



**TECHNISCHE  
UNIVERSITÄT  
DRESDEN**



Leibniz-Institut  
für Festkörper- und  
Werkstoffforschung  
Dresden

---

# Topologically non-trivial states in one- and quasi-one-dimensional frustrated spin systems

Dissertation  
zur Erlangung des akademischen Grades  
Doctor rerum naturalium  
(Dr. rer. nat.)

vorgelegt der  
Fakultät Physik  
der Technischen Universität Dresden

von  
**Clìo Eftimìa Agrapìdis**  
geboren am 3. Oktober 1991 in Ravenna (Italien)



Eingereicht am 27.08.2019

Verteidigt am 07.11.2019

1. Gutachter: Prof. Jeroen van den Brink
2. Gutachter: Prof. Andreas Honecker



*Kannst du lesen, so sollst du verstehen; kannst du schreiben, so musst du etwas wissen...*

---

Goethe, Maximen und Reflexionen



# Contents

---

|          |   |           |
|----------|---|-----------|
| <b>1</b> | <b>Introduction</b>   | <b>1</b>  |
| 1.1      | Quantum phase transitions . . . . .   | 2         |
| 1.2      | Concepts in magnetic frustration . . . . .                                  | 3         |
| 1.3      | One-dimensional systems . . . . .   | 4         |
| 1.4      | Methods . . . . .   | 5         |
| <b>2</b> | <b>Quasi one-dimensional frustrated materials</b>                           | <b>9</b>  |
| 2.1      | Magnons, spinons and spin waves . . . . .                                   | 9         |
| 2.2      | The spin-Peierls transition . . . . .                                       | 10        |
| 2.3      | Cuprate chains with ferromagnetic first-neighbour interaction . . . . .     | 11        |
| <b>3</b> | <b>The ferromagnetic frustrated <math>J_1</math>-<math>J_2</math> chain</b> | <b>15</b> |
| 3.1      | Introduction . . . . .  | 15        |
| 3.2      | Frustrated ferromagnetic $J_1$ - $J_2$ chain . . . . .                      | 16        |
| 3.2.1    | AKLT model . . . . .  | 17        |
| 3.2.2    | Methods . . . . .   | 20        |
| 3.2.3    | Spin gap . . . . .  | 20        |
| 3.2.4    | Valence Bond Solid . . . . .  | 23        |
| 3.2.5    | Entanglement entropy and spectrum . . . . .                                 | 25        |
| 3.2.6    | Dimerisation order . . . . .  | 27        |
| 3.2.7    | Matrix product state . . . . .  | 30        |
| 3.3      | Dimerised $J_1 - J'_1 - J_2$ chain . . . . .                                | 31        |
| 3.3.1    | Model and method . . . . .  | 31        |
| 3.3.2    | Ferromagnetic critical point . . . . .                                      | 32        |
| 3.3.3    | Haldane gapped state . . . . .  | 33        |
| 3.4      | Discussion . . . . .  | 36        |
| <b>4</b> | <b>Kitaev materials</b>   | <b>39</b> |
| 4.1      | The Kitaev model . . . . .  | 39        |
| 4.2      | Kitaev interaction in real materials . . . . .                              | 46        |
| <b>5</b> | <b>The Kitaev-Heisenberg chain</b>  | <b>49</b> |
| 5.1      | Motivation . . . . .  | 49        |
| 5.2      | Model and Numerical Methods . . . . .                                       | 50        |
| 5.2.1    | 1D Kitaev-Heisenberg Hamiltonian . . . . .                                  | 50        |
| 5.2.2    | Numerical methods . . . . .   | 51        |
| 5.3      | Ground-state properties . . . . .   | 52        |
| 5.3.1    | Quantum phase transitions . . . . .   | 52        |
| 5.3.2    | Ferromagnetic- $xy$ phase ( $\pi < \phi < \frac{3\pi}{2}$ ) . . . . .       | 52        |
| 5.3.3    | Ferromagnetic- $z$ phase ( $0.65\pi \lesssim \phi < \pi$ ) . . . . .        | 54        |
| 5.3.4    | Spiral- $xy$ phase ( $\frac{\pi}{2} < \phi \lesssim 0.65\pi$ ) . . . . .    | 55        |

|          |  |            |
|----------|--|------------|
| 5.3.5    | Néel- $z$ ordered phase ( $1.65\pi \lesssim \phi < 2\pi$ ) . . . . .                 | 56         |
| 5.3.6    | Staggered- $xy$ ordered phase ( $\frac{3\pi}{2} < \phi \lesssim 1.65\pi$ ) . . . . . | 59         |
| 5.3.7    | Tomonaga-Luttinger-liquid phase ( $0 \leq \phi < \frac{\pi}{2}$ ) . . . . .          | 60         |
| 5.3.8    | Kitaev points . . . . .  | 61         |
| 5.4      | Phase diagram . . . . .  | 64         |
| 5.5      | Low-lying excitations . . . . .  | 66         |
| 5.5.1    | Tomonaga-Luttinger-liquid phase ( $0 \leq \phi < \pi/2$ ) . . . . .                  | 66         |
| 5.5.2    | Spiral- $xy$ phase ( $\frac{\pi}{2} < \phi \lesssim 0.65\pi$ ) . . . . .             | 69         |
| 5.5.3    | Ferromagnetic- $z$ phase ( $0.65\pi \lesssim \phi < \pi$ ) . . . . .                 | 69         |
| 5.5.4    | Ferromagnetic- $xy$ phase ( $\pi < \phi < \frac{3\pi}{2}$ ) . . . . .                | 70         |
| 5.5.5    | Staggered- $xy$ ordered phase ( $\frac{3\pi}{2} < \phi \lesssim 1.65\pi$ ) . . . . . | 70         |
| 5.5.6    | Néel- $z$ ordered phase ( $1.65\pi \lesssim \phi < 2\pi$ ) . . . . .                 | 70         |
| 5.6      | Discussion . . . . .   | 71         |
| <b>6</b> | <b>Kitaev-Heisenberg ladder</b> . . . . .  | <b>73</b>  |
| 6.1      | Introduction . . . . .   | 73         |
| 6.2      | Model and Method . . . . .   | 74         |
| 6.2.1    | Model . . . . .  | 74         |
| 6.2.2    | Method . . . . .   | 75         |
| 6.3      | Ordered phases . . . . .   | 76         |
| 6.3.1    | Stripy phase ( $1.57\pi < \phi < 1.7\pi$ ) . . . . .                                 | 76         |
| 6.3.2    | Zigzag phase ( $0.53\pi \leq \phi < 0.8\pi$ ) . . . . .                              | 78         |
| 6.3.3    | Rung-singlet phase ( $-0.3\pi \leq \phi \leq 0.48\pi$ ) . . . . .                    | 79         |
| 6.3.4    | Ferromagnetic phases . . . . .   | 81         |
| 6.4      | Spin-liquid states . . . . .   | 82         |
| 6.4.1    | Plaquette operator . . . . .   | 83         |
| 6.4.2    | Excitation gap . . . . .   | 83         |
| 6.4.3    | String order parameter . . . . .   | 84         |
| 6.5      | Phase diagram . . . . .  | 85         |
| 6.6      | Low-lying excitations . . . . .  | 86         |
| 6.6.1    | Rung-singlet phase . . . . .   | 86         |
| 6.6.2    | Stripy phase . . . . .   | 87         |
| 6.6.3    | Zigzag phase . . . . .   | 87         |
| 6.6.4    | FM states . . . . .  | 89         |
| 6.6.5    | Kitaev spin liquid . . . . .   | 89         |
| 6.7      | Discussion . . . . .   | 90         |
| <b>7</b> | <b>Conclusion</b> . . . . .  | <b>91</b>  |
|          | <b>Bibliography</b> . . . . .  | <b>94</b>  |
|          | <b>Acknowledgments</b> . . . . .   | <b>107</b> |
|          | <b>Eidesstattliche Erklärung</b> . . . . .   | <b>109</b> |



# 1

## Introduction

---

Magnetism is a phenomenon we encounter in our daily lives from a very young age. As kids, one of the first toys we interact with is a “magic board” consisting of a pen with a magnetic tip and a screen hiding some dark magnetic powder floating in a white liquid: rolling the pen on the board our drawing appears and we can wipe it clean just by swiping a bar that will release the powder to the hidden back. As adults, we often use magnets to hold notes on our fridge, or keep track of our reading progress using magnetic bookmarks. We can safely state that a large part of the population has directly interacted with some magnetic material.

On the other hand, the microscopic theory of magnetism still poses several questions. We know that the fundamental blocks for a microscopic magnetic theory are spin and orbital moments. While orbital moments have an analogue in classical mechanics, spins are an intrinsic quantum property of particles and have no classical counterpart.

One of the first attempts to model ferromagnetism is the Ising model proposed by E. Ising in his PhD dissertation under the supervision of W. Lenz [1]. In this model, the spins are viewed as a vector that can only point up or down (Ising spins). Ising introduced an interaction between nearest neighbour (NN) spins:

$$\mathcal{H}_{\text{Ising}} = -J \sum_{\langle i,j \rangle} S_i S_j, \quad (1.1)$$

with  $J > 0$ . His study was performed on a one dimensional chain, and did not show any possible phase transition to a ferromagnetically ordered state at finite temperature. While Ising believed his model to be flawed, we now know that it is not the Hamiltonian that supports the ordered state at finite temperature, but rather the dimensionality is to be blamed for that. In fact, it has been shown that the Ising interaction leads to phase transitions at finite temperature in two [2, 3] and three dimensions [4, 5, 6].

Going back to our daily experience, the magnetic materials we are most used to are ferromagnetic (FM) materials. In fact, ferromagnetism was already known to ancient Greeks and it was the first one to be tackled through a microscopic theory, as evident from the choice of FM interaction in the Ising model. This can be understood by noting that the finite magnetic moment of a ferromagnet is macroscopically detectable (think of the magnets on your fridge). Opposite to this phenomenon, we have antiferromagnetic (AFM) materials. Those will not show any finite net magnetic moment, despite not being a trivial paramagnet, where moments point disorderly in all directions, averaging to a vanishing total magnetic moment. Theoretical studies on AFM materials started in the 1930s with Louis Néel and the existence of such an ordered state was experimentally shown in 1949 thanks to neutron diffraction measurements of MnO taken by Clifford Shull and Stuart Smart [7].

While antiferromagnetism was the challenge in the beginning of the 20th century, magnetism in the 21st century is dealing with a new, more exotic, form of magnetism. Namely, what we have come to call as frustrated magnetism. The simplest example to show how this new flavour of magnetism works is to consider three Ising spins on

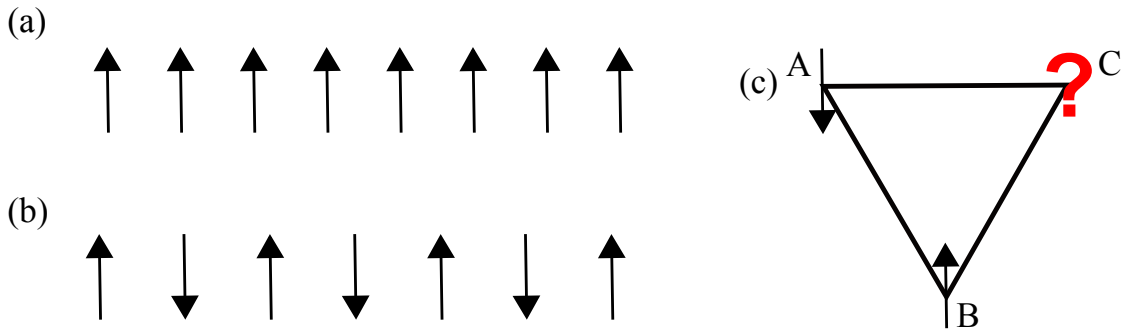


Figure 1.1: Examples of (a) FM ordering and (b) AFM ordering on a chain. (c) Ising spins with AFM interactions on a triangle are the simplest example of geometric frustration (see text).

an equilateral triangle with AFM interactions, i.e., the energy is minimised when the spins are antiparallel. We can fix the A spin in Fig. 1.1(c) to point up, then the B spin would point down, but what about the C spin? It is not possible for this system to minimise all interactions at once. In such cases, we talk of geometrical frustration, since the frustration arises from the geometrical properties of the lattice.

Another path to frustration is known as exchange frustration. In this case, different spin components interact in an Ising fashion on different bonds. The most famous example of such a kind of frustration is the Kitaev model, which will be introduced in more detail in Chapter 4.

In this dissertation, we will present examples of both geometrical and exchange frustration on one-dimensional (1D) and quasi-one-dimensional (quasi-1D) systems. Before we do so, we will briefly introduce quantum phase transitions, some concepts in frustrated magnetism and 1D systems, and talk about the numerical method, namely the density matrix renormalisation group (DMRG) method, used in this work.

## 1.1 Quantum phase transitions

The concept of phase transitions is common to most people. Everyone knows that water will turn into ice when put in a freezer and that it is important that the water is boiling before we throw in our pasta for cooking. These changes in state that are commonly experienced have one thing in common: a change in temperature. In this work, however, we consider systems at zero temperature. How do we change the state of our system then? In this case, a phase transition can be induced by varying a non-thermal parameter, such as pressure, magnetic field or chemical composition, i.e., doping. Transitions of this kind are called quantum phase transitions (QPT), as the leading mechanism breaking the order is represented by quantum fluctuations.

Considering systems at zero temperature allows us to avoid the constraint on 1D systems imposed by the Mermin-Wagner theorem [8]. This theorem states that there cannot be any spontaneous breaking of continuous symmetries at finite temperature for  $d \leq 2$ . As said above, we here consider systems at zero temperature. Thus, quantum phase transitions are allowed in 1D systems.

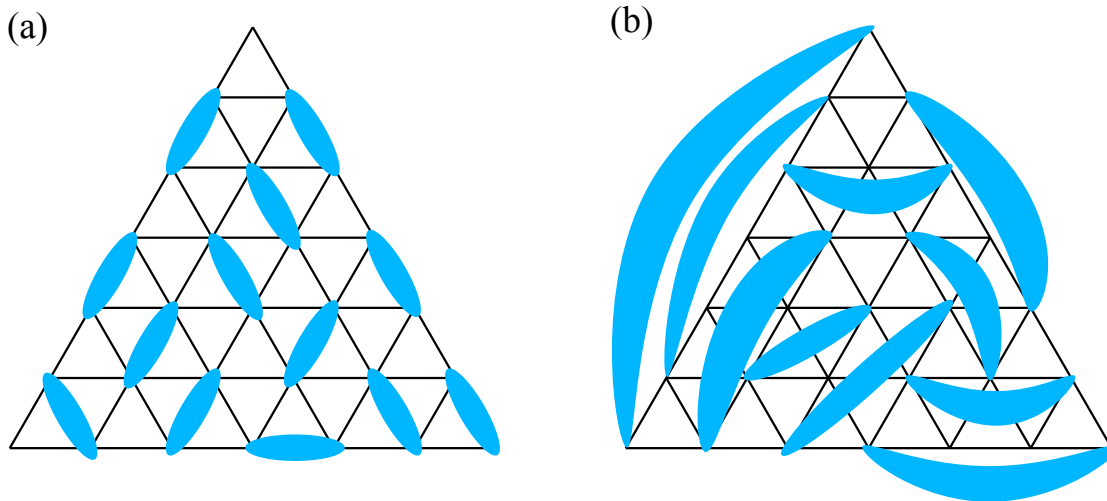


Figure 1.2: A possible configuration for (a) a short range RVB spin liquid and (b) a long range RVB spin liquid on a triangular lattice.

In this work, we study different 1- and quasi-1D phase diagrams as the couplings in the Hamiltonian change. Physically, this change would be induced by one of the non-thermal parameters listed above. Moreover, as some of these models can apply to different materials with different values of the interactions, a study of the whole phase diagram for different ratios of the couplings gives access to universal predictions for all materials described by a certain Hamiltonian and a better understanding of the physics typical of the model considered.

## 1.2 Concepts in magnetic frustration

As briefly stated above, the hydrogen atom of geometric frustration is composed of three spins with AFM interactions on a triangle. If we now consider Heisenberg spins, i.e., spins with three components  $S^x$ ,  $S^y$  and  $S^z$  that follow the angular momentum commutation relations, and consider a whole triangular lattice, we end up with a different frustrated system. This model was used by Anderson in 1973 when he first introduced the concept of a resonating valence bond (RVB) state [9]. If we consider a lattice where spins form valence bonds, i.e., singlets, between first neighbours, then we are in the presence of a valence bond solid (VBS). This state has total spin 0 and is non-magnetic. In a perfect VBS state, NN spins are maximally entangled, but they are not entangled with the other spins in the system. Moreover, the formation of singlets on certain bonds can break the translational symmetry in the lattice. If we now allow for quantum fluctuations to act on the valence bonds, so that the ground state is composed of all possible superpositions of different partitions of spins into valence bonds, we are in the presence of a quantum spin liquid (QSL). We can further distinguish between short-range and long-range RVB pairing, as shown in Fig. 1.2.

Though the original proposal of Anderson was modelled on the spin- $\frac{1}{2}$  AFM Heisenberg triangular lattice, the ground state of this model is yet to be defined. It is, however, possible to say that this model shows long range order with finite magnetisation  $\sim 60\%$

of the classical one [10, 11, 12, 13, 14, 15]. These results rely on numerical methods such as quantum Monte Carlo and exact diagonalization. They also show that powerful and reliable numerical methods are of great importance in the context of magnetic frustration.

The RVB state proposed by Anderson is the first example of what we call a QSL. This state of matter is defined by the absence of magnetic ordering down to zero temperature. The absence of ordering is due to strong quantum fluctuations, typical of frustrated systems. Moreover, QSL do not spontaneously break any symmetry and show long-range entanglement, fractionalised excitations and artificial gauge fields [16]. All of these properties are predicted by theory, which also classifies different QSL based on their symmetry properties (topological order) [17]. Nonetheless, this state of matter is very elusive and hard to conclusively detect experimentally, due to the lack of a “smoking gun” signature. In fact, this state is characterised by the vanishing value of all major observables: no magnetisation, no dissipation, exponential/power-law decay in the correlations for gapped/gapless QSL. Possible probes for measuring QSL properties are: specific heat measurements, which can be compared to the theoretically expected low-energy density of states, thermal transport measurements, which can detect the nature of the excitations, i.e., fractionalisation, and neutron scattering measurements, which give information about the nature of the excitations through their energy dispersion and also information about the correlations in the system.

Another possible consequence of magnetic frustration, almost opposite to the formation of spin liquid states, is the phenomenon known as order by disorder. This characteristic situation was first introduced by Villain in 1980 [18]. He analysed a magnetic model with a classically degenerate ground state and was the first to recognise the importance of focusing on the free energy. The high degeneracy in the ground state we are referring to is not the usual symmetry related degeneracy: these states are not symmetry related. They are, in fact, characterised by different symmetries. By including fluctuations, quantum or thermal, it is possible to break this degeneracy and select a certain ordered state. Hence, an ordered state is chosen through the disordered fluctuations, explaining the naming *order by disorder*.

### 1.3 One-dimensional systems

The properties of 1D systems are very different from those of higher dimensional systems. First of all, it is easy to notice that only collective excitations are possible. In fact, electrons cannot “avoid” each other in 1D, and only a collective motion is possible, much like people waiting in line at the bank.

The basic concept behind 1D physics is given by the Tomonaga-Luttinger model, also called the Tomonaga-Luttinger liquid (TLL). This model clearly shows how the concept of a Fermi liquid breaks down in 1D, as scattering processes close to the Fermi level become of the utmost importance. Tomonaga was the first to realise that the low-energy excitations of a 1D non-interacting fermionic system are bosonic-like excitations with linear dispersion relation [19]. Luttinger extended this model to an exactly solvable one that shows the following properties: there are no fermionic low-lying excitations, there is no Fermi surface as in the usual definition, correlation functions decay asymptotically at large distances and long times with non-universal exponents [20]. All of these properties

descend from the linear dispersion.

In 1D, there is no Fermi surface, but only two Fermi points  $\pm k_F$ . All states far below these points are filled and all those far above are empty. Therefore, single-particle and electron-hole pair excitations are situated near those points in a  $k_B T$  range and determine the physical properties of the system. Let us focus on electron-hole excitations. If both the particle and the hole are in the vicinity of the same Fermi point, the required momentum  $q$  for the process is much smaller than  $k_F$ . On the other hand, if they are around opposite points, the required momentum is of the order of  $\pm 2k_F$ . Thus, low-energy particle-hole excitations exist only at  $q = 0, \pm 2k_F$ . Without going into mathematical details, using the linear dispersion it follows that the excitation energy is always  $\pm \hbar v_F q$  independently of the position of the hole, giving rise to a highly degenerate spectrum. Moreover, the system can be mapped from fermion to boson operators and the Fermi sea is their vacuum.

Maybe the most important property of the excitations of this model is the so called spin-charge separation. This is an example of fractionalisation, i.e., the mechanism for which the excitations of a system only carry a part of the physical quantities of the original particle. In fact, an electron has a charge  $e$  and a spin  $S$ , but through fractionalisation these are split in two quasi-particles: spinons, carrying the spin degree of freedom, and holon, carrying the charge degree of freedom. These two quasi-particles propagate separately in the system. Fractionalisation appears in other systems, such as the fractional quantum Hall effect and spin liquids, and it is a signature of the topological nature of the system in question.

It is important to notice that the isotropic AFM Heisenberg chain is in a TLL state and the non-Fermi liquid behaviour is a generic property of 1D systems.

## 1.4 Methods

When considering spin-1/2 systems as we do in this study, the size of the Hilbert space grows exponentially with the size of the system as  $2^L$ , with  $L$  being the system's size. Therefore, exact diagonalization methods such as the Lanczos algorithm cannot easily tackle systems larger than  $L = 30-40$ . While in some cases this might be enough, especially given that these methods are numerically exact, there are systems in which finite size scaling is of the foremost importance. Moreover, there are cases where the long range order (LRO) stabilises only after reaching a certain critical size.

To tackle large systems in 1D and quasi-1D, one of the best numerical tools is the density matrix renormalisation group (DMRG). Introduced by S. R. White in 1992 [21] as an evolution of the numerical renormalisation group of Wilson, DMRG has widely spread and it is nowadays recognised as highly trustworthy. In this section, we explain the ideas behind our version of the algorithm.

The main idea behind any renormalisation group procedure is to keep only the relevant degrees of freedom. This is achieved through successively eliminating the microscopic degrees of freedom, ending up with a coarse-grained version of the initial system that still keeps all of the information we are looking for. In DMRG, the renormalisation procedure is performed on the eigenstates of the density matrix of the system [21, 22].

There are three lines of reasoning focusing on the optimisation of different quantities

for why this truncation procedure leads to a good approximation of the exact ground states: optimisation of expectation values [23], optimisation of the wave function [21, 24] and optimisation of entanglement [25, 26, 27, 28]. We will here present the argument about optimising the expectation values.

Consider a system  $S$  of length  $\ell$  and add a site  $\sigma$ . The physical state of the system can be represented through the reduced density matrix

$$\hat{\rho} = \text{Tr}_\sigma |\psi\rangle \langle\psi| \quad (1.2)$$

where  $|\psi\rangle$  is the pure ground state of the supersystem  $S\sigma$  and we have traced out the site  $\sigma$ . Diagonalising the matrix  $\rho$ , we find it has  $N$  eigenvalues  $w_\alpha$ , with  $N$  being the Hilbert space dimension of the system  $S$  and  $w_\alpha \geq 0$ . Let us order the eigenstates in decreasing value, so that  $w_1 \geq w_2 \geq w_3 \geq \dots \geq w_N$ . The prescription used in DMRG is to keep only the first  $m$  largest eigenvalues and the related eigenstates. Let us consider a bounded operator  $\hat{A}$  acting on  $S$ . The expectation value can be expressed in terms of the reduced density matrix as

$$\langle\hat{A}\rangle = \text{Tr}_S \hat{\rho} \hat{A} = \sum_{\alpha=1}^N w_\alpha \langle w_\alpha | \hat{A} | w_\alpha \rangle. \quad (1.3)$$

Keeping only the  $m$  largest eigenvalues translates to the expectation value of  $\hat{A}$  as

$$\langle\hat{A}\rangle_{\text{approx}} = \sum_{\alpha=1}^m w_\alpha \langle w_\alpha | \hat{A} | w_\alpha \rangle. \quad (1.4)$$

The error done with this approximation is bounded from above

$$\langle\hat{A}\rangle_{\text{approx}} - \langle\hat{A}\rangle \leq \left( \sum_{\alpha>m}^N w_\alpha \right) c_A = \epsilon_\rho c_A, \quad (1.5)$$

where  $c_A$  is the exact expectation value for  $\hat{A}$ . For local quantities, errors are of the order of the truncated weight

$$\epsilon_\rho = 1 - \left( \sum_{\alpha>m}^N w_\alpha \right). \quad (1.6)$$

In this study, we use finite DMRG (fDMRG). This, however, needs infinite DMRG (iDMRG) as a warm-up step. Therefore, we will now briefly present both versions of the algorithm.

In our iDMRG warm-up step, we start by considering a block  $S$  with a Hilbert space of dimension  $m$  and a basis  $\{|m\rangle_\ell\}$ ,  $\ell$  being the length of the system. We now add a site  $\sigma$  to the block  $S$  and we assume its Hilbert space to have dimension  $d$ , so that the final total dimension for the Hilbert space of the superblock  $S\sigma$  is  $md$  and the basis is composed of product states  $\{|m_\ell\sigma\rangle\} = \{|m_\ell\rangle|\sigma\rangle\}$ . Though the Hamiltonian  $\mathcal{H}_{\ell+1}$  for  $S\sigma$  can be represented in this basis explicitly, this is normally not done in order to preserve storage space. Using a large sparse-matrix diagonalisation algorithm, we now find the ground state  $|\Psi\rangle$  of the Hamiltonian  $\mathcal{H}_{S\sigma}$ . From  $|\Psi\rangle$ , we construct the density matrix  $\rho = |\Psi\rangle \langle\Psi|$ . This is a  $md \times md$  matrix. By tracing out the site's degrees of freedom, we

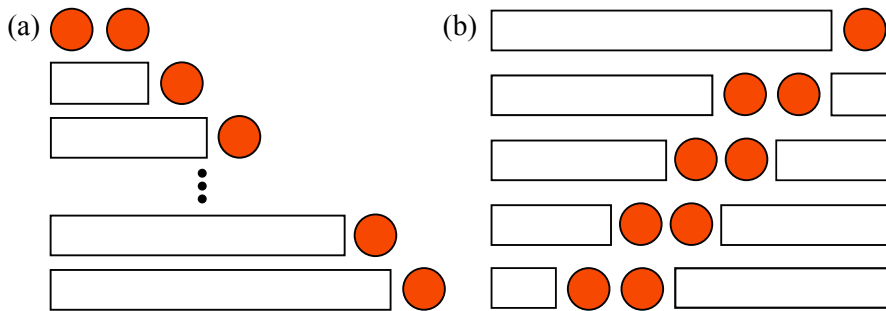


Figure 1.3: A visual representation of the DMRG method: (a) represents the iDMRG algorithm. Starting from two sites, one site is added at every step of the algorithm until a final length  $L$  is reached. (b) The fDMRG algorithm starts from the last step of the iDMRG one. The figure shows how the block  $E$  grows against the block  $S$ .

find the reduced density matrix  $\rho_S = \text{Tr}_\sigma \rho$ . Having the reduced density matrix, we now perform the “real” renormalisation procedure: we diagonalise this matrix and keep only the  $m$  eigenstates with the largest eigenvalues. The last step is to perform a reduced basis transformation  $\mathcal{H}_{\ell+1}^{\text{tr}} = T^\dagger \mathcal{H}_{\ell+1} T$ , with  $T$  being a rectangular matrix of size  $md \times m$  with elements  $\langle \psi_\sigma | m_{\ell+1} \rangle$ . Here,  $|m_{\ell+1}\rangle$  refers to the basis for a block with length  $\ell + 1$ . We rename  $\mathcal{H}_{\ell+1}^{\text{tr}} \rightarrow \mathcal{H}_{\ell+1}$  and we perform the procedure described above until we reach a certain fixed length  $L$ . This construction allows us to observe a translational symmetry broken state.

The fDMRG algorithm starts from the last step of the iDMRG one. We consider a system ( $S$ ) and an environment ( $E$ ) block. While the iDMRG involves only growing the block and renormalising it, fDMRG fixes the whole length of the superblock  $S + E$  and grows only one block at a time, while shrinking the other one. Moreover, the projection procedure described above is carried out only on the growing block. So, we will start with two blocks and let the environment grow, while the system shrinks. While doing so, the renormalisation procedure is applied only to the environment block. Once the system cannot shrink anymore, the procedure is reversed: the system block grows against the environment one until the minimal length for the environment is reached. This process is called a sweep. To check convergence, different sweeps are performed and, in many cases, the use of different  $m$ -values is advised as well as  $m$ -value extrapolation of interesting quantities.





# 2 Quasi one-dimensional frustrated materials

As introduced in the previous chapter, 1D physics shows peculiar phenomena arising from strong quantum fluctuations [29]. As in this work we are dealing with frustrated spin systems, we will now present some of the important concepts emerging due to the interplay of low-dimensionality and geometric frustration and we will relate them to studied materials that can be well described by quasi-1D models.

## 2.1 Magnons, spinons and spin waves

When considering a ferromagnet, the way we picture it is with having all of its spins parallel to each other. This would be the ground state configuration. The easiest perturbation we can apply to this ground state is the flip of a single spin. If we consider the system to have only NN FM interactions, it is easy to see how the energy would rise and the neighbouring spins would “notice” the antiparallel defect. Because of that, they will also tend to misalign from the magnetisation direction, but instead of completely reversing their direction, they will only slightly change it. Their neighbours will also follow this behaviour and this whole process will create a collective misalignment known as a spin-wave. More quantitatively, a single spin-flip would cost an energy  $|J|$ , with  $J$  being the FM Heisenberg coupling. If we allow for superpositions of this kind of excitation all over the system, the energy cost tends to zero in the small  $\mathbf{q}$  limit, with  $\mathbf{q}$  being transferred momentum. This limit corresponds to considering very large wavelengths for the spin-waves. Hence, we can conclude that spin-waves are the magnetic excitations of a FM material. Because quantum mechanics allows us to associate a particle with a wave, we can define a quasi-particle called magnon and associate it with the spin-wave. Magnons are bosonic quasi-particles and carry a spin  $S = 1$ . In most cases, when the wave properties such as propagation direction and dispersion are not important, people use magnons to treat FM excitations.

Let us now consider the AFM case. In particular, let us take into consideration a Néel chain. A single spin-flip can result into two domain walls as depicted in Fig. 2.1(a). These two domains do not cost any additional energy, so that a single domain has an energy of  $\sim |J|/2$ . Now, a single spin flip  $S^z = 1$  results in two different independent quasiparticles [see Figs. 2.1(b) and 2.1(c)]. As the total  $S^z$  is not changed, each quasiparticle carries spin  $S = 1/2$ . We call such excitations spinons. Because in 1D the spinons propagate independently and without additional energy cost, we say they are deconfined. For higher dimensions, separating a magnon into two spinons generally requires energy. We then talk about confined spinons. The energy cost comes from noting that, in a 2D or 3D AFM ordered state, the two spinons are connected by a string of flipped spins with frustrated, i.e., not satisfied, bonds. Thus, the energy is proportional to the length of the string. In a 1D Heisenberg AFM, the dispersion relation for spinons can be found through the Bethe ansatz [30]:

$$\hbar\omega_q^{\text{spinon}} = \frac{\pi}{2}J \sin q, \quad (2.1)$$

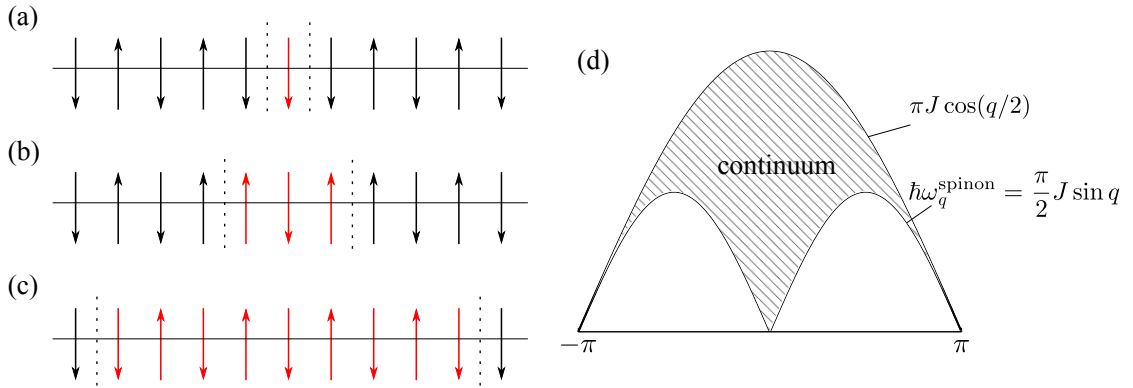


Figure 2.1: (a) A spin flip in a Néel chain creates two domain walls [29]. Panels (b) and (c) show the propagation of the spinon quasiparticles. (d) The spinon dispersion relation and continuum.

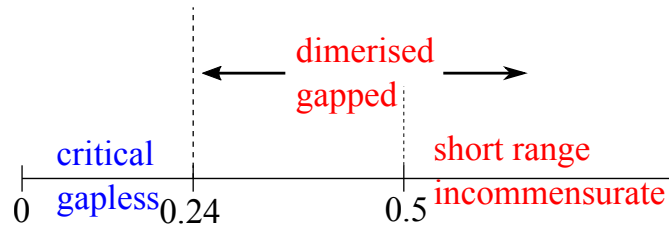


Figure 2.2: The phase diagram for the AFM  $J_1$ - $J_2$  chain as a function of the parameter  $\alpha$

where  $J > 0$  is the AFM coupling. As a single excitation generates a pair of spinons, the momentum  $q$  can be distributed in different ways between the two quasiparticles. This leads to the existence of a spinon continuum of excitations for a single momentum  $q$  (Fig. 2.1 (d)).

## 2.2 The spin-Peierls transition

The spin-Peierls transition takes its name from the similar Peierls transition that can take place in conducting quasi-1D materials. This transition implies a dimerisation in the underlying lattice structure, i.e., spontaneous translational symmetry breaking. In fact, dimerisation on the chain merely means that two bonds that are equivalent in the Hamiltonian become inequivalent on the lattice. One can see this as a displacement along the chain, where pairs of electrons alternate being closer or further apart. The dimerisation causes a gap in the electronic spectrum which, in return, lowers the energy of the filled bands below the gap. A similar picture can be used for spin chains, only that, in this case, the dimerisation is driven by spin-spin interactions instead of being an instability related to conduction electrons. Moreover, a spin-Peierls transition also involves the formation of a spin gap.

This phenomenon was first observed in organic materials [31]. The first inorganic crystal showing this transition was  $\text{CuGeO}_3$ . In 1993, Hase *et al.* showed that the reduction in the magnetic susceptibility  $\chi(T)$  was isotropic along the different magnetic axis, in contrast with the pure AFM transition [32]. The sharp drop in  $\chi$  happens at

$T_{SP} = 14$  K. Through the existence of a broad maximum in the correlations at  $T_{\max} = 56$  K, the intrachain coupling is fixed to be  $J = 88$  K. When  $T < T_{SP}$ , the chain exhibits two alternating NN coupling  $J_1$  and  $J'_1$  due to dimerisation with  $J_1^{(\prime)} = J(1 \pm \delta(T))$ . The dimerisation parameter is found to be  $\delta = 0.17$  through its proportionality to the spin gap ( $\Delta \sim \delta^{2/3}$ ), which is measured to be  $\Delta = 24$  K. The small interchain couplings have been determined through inelastic neutron scattering to be  $J_b = 0.1 J$  and  $J_c = -0.1 J$  [33]. All spin-Peierls compounds show a similar magnetic phase diagram composed of a uniform phase, a dimerised phase and an intermediate phase [34]. This intermediate state is thought to be a commensurate, dicommensurate or incommensurate state.

By neglecting the effect of the electron-phonon coupling, this compound might be modelled by the so called AFM  $J_1$ - $J_2$  chain [35], with  $J_1$  ( $J_2$ ) being the nearest (next nearest) neighbour interaction. The Hamiltonian is given by

$$\mathcal{H} = J_1 \sum_i \mathbf{S}_i \cdot \mathbf{S}_{i+1} + J_2 \sum_i \mathbf{S}_i \cdot \mathbf{S}_{i+2}, \quad (2.2)$$

where  $J_1, J_2 > 0$ . It is easy to see this model is, indeed, geometrically frustrated. By defining a frustration parameter  $\alpha = J_2/J_1$ , the quantum phase transition from a gapless to a gapped state is found at  $\alpha_C = 0.24$  [36, 37, 38]. We show the full phase diagram of the AFM  $J_1$ - $J_2$  chain in Fig. 2.2.

## 2.3 Cuprate chains with ferromagnetic first-neighbour interaction

While the  $\text{CuGeO}_3$  compound exhibits NN AFM interactions, most spin chains composed of edge sharing  $\text{CuO}_6$  octahedra have a FM  $J_1$  interaction ( $J_1 < 0$ ). As the next nearest neighbour (NNN) coupling is AFM, these chains are frustrated. We will thoroughly analyse the ground state phase diagram of what we call the FM  $J_1$ - $J_2$  chain (in contrast to the pure AFM  $J_1$ - $J_2$  one) in Chapter 3. Here, we present some of the compounds that are believed to be described by the FM  $J_1$ - $J_2$  chain as a minimal model. We point out that this system is expected to be in an incommensurate spin helix state for  $J_2/|J_1| > 1/4$  [41].

Several compounds are expected to show this kind of interactions, such as  $\text{LiCu}_2\text{O}_2$  [44],  $\text{Li}_2\text{CuZrO}_4$  [39],  $\text{LiCuSbO}_4$  [43] and  $\text{LiCuVO}_4$  [45]. The last one, in particular, shows ferroelectricity at low temperature and spin nematicity at high magnetic fields. The crystal structure is shown in Fig. 2.3(c). The  $\text{Cu}^{2+}$  ions form magnetic chains with  $S = 1/2$  along the orthorhombic  $b$  axis [45]. The values of the couplings are found to be  $J_1 = -19$  K and  $J_2 = 44$  K. It is, however, necessary to include an interchain coupling  $J' = -4.6$  K in order to explain the long-range helix order setting at  $T_N = 2.4$  K [46]. The incommensurate vector is found to be  $\mathbf{Q} = (0; 0.532; 0)$  and the spin spiral ground state is in the  $ab$  plane. We show the magnetoelectric phase diagram from Ref. [42] in Fig. 2.4(a).

While  $\text{LiCuVO}_4$  shows long-range order at low temperature, the similar compound  $\text{LiCuSbO}_4$  does not exhibit it down to  $T_N = 0.1$  K. Through  $^7\text{Li}$  nuclear magnetic resonance (NMR) measurements it was possible to probe the temperature dependence of the spin lattice relaxation rate  $T_1^{-1}$  at various fields [43]. The magnetic phase diagram found in this study is shown in Fig. 2.4(b). The first feature reported in Ref. [43] is

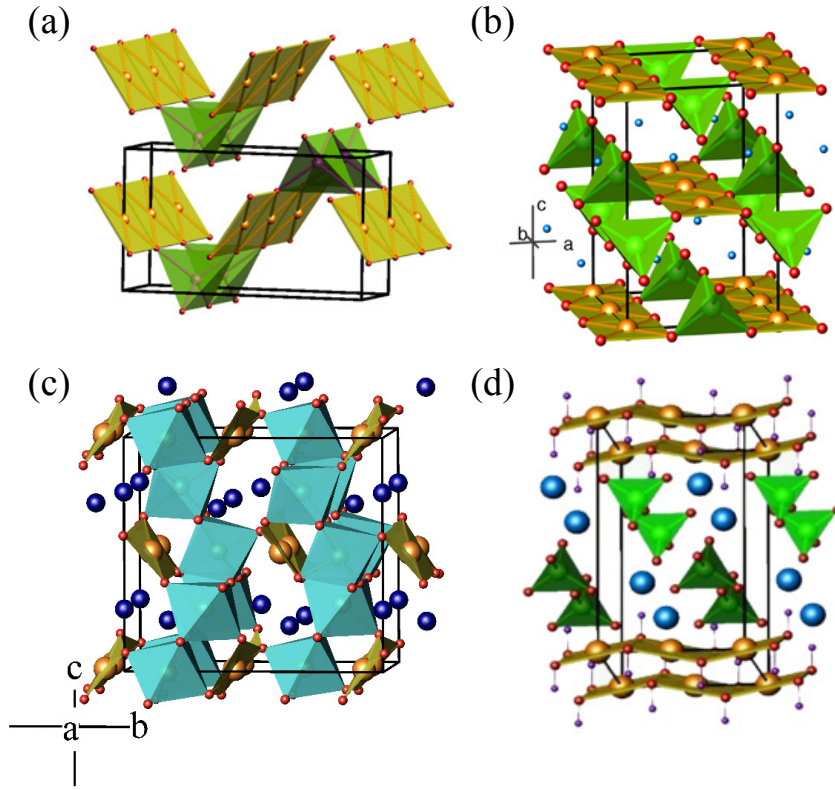


Figure 2.3: Crystal structure of (a)  $\text{CuGeO}_3$ , (b)  $\text{LiCuVO}_4$ , (c)  $\text{LiCuSbO}_4$  and (d)  $\text{PbCuSO}_4(\text{OH})_2$ . Figs. (a) and (b) are taken from Ref. [39]. Fig. (d) is modified from Ref. [40].

that the ordering temperature increases with field, against the normal behaviour of the Néel temperature, which is expected to be suppressed under magnetic field. Moreover, a critical field  $\mu_0 H_c = 13$  T was determined. At this field,  $T_1^{-1}$  vs  $T$  is drastically suppressed. This has been interpreted as a point at which magnetic fluctuations change. Furthermore, a spin gap was observed and several possible mechanisms were taken into consideration before claiming that the correct magnetic ground state is a nematic spin liquid.

Another spin chain compound that presents a rich magnetic phase diagram is the linearite compound  $\text{PbCuSO}_4(\text{OH})_2$ . Linear spin wave theory predicts the couplings to be  $J_1 = -114$  K and  $J_2 = 37$  K [47]. For this material, it is necessary to consider an interchain coupling  $J' = 4$  K. DMRG calculations find an anisotropic  $\mathbf{J}_1 = (J_1^x, J_1^y, J_1^z) = (-91.1, -86.6, -88.4)$  K and  $J_2 = 28.3$  K, so that  $\alpha \sim 0.32$  [40] in order to describe the experimental results. Within these calculations, the interchain coupling is found to be  $J' = 2.7$  K. The phase diagram has been determined through neutron diffraction and  $^1\text{H-NMR}$ . It is composed by five different states for field parallel to the  $b$  axis [48, 49, 50]. The low-temperature and low-field phase is a helical incommensurate magnetic state with  $\mathbf{Q} = (0; 0.186; 0.5)$  [51] (phase I in Fig. 2.4(c)). At lower temperatures, an hysteretic phase II separates phase I from the polarised phase IV with commensurate vector  $\mathbf{Q} = (0; 0; 0.5)$  [48]. For  $T > 600$  mK, phase I and IV are separated by a coexistence phase III [48].

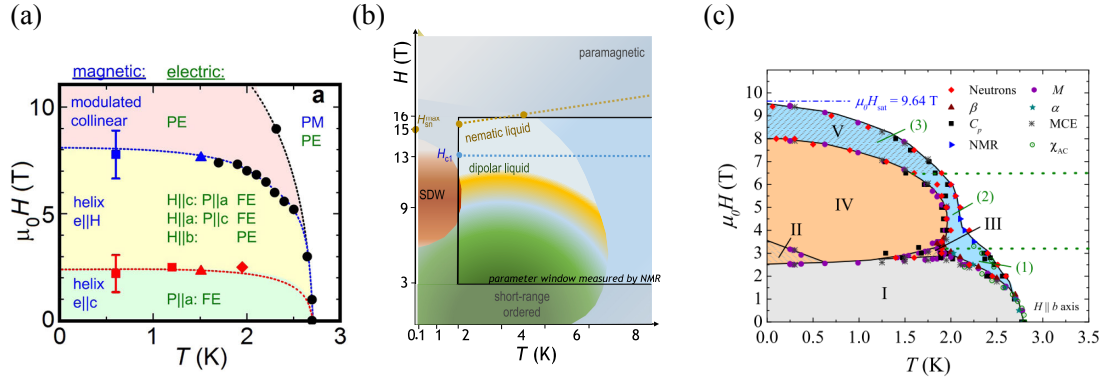


Figure 2.4: (a) Magnetoelectric phase diagram of  $\text{LiCuVO}_4$  as reported in Ref. [42]. (b) Magnetic phase diagram of  $\text{LiCuSbO}_4$  as reported in Ref. [43]. (c) Magnetic phase diagram of  $\text{PbCuSO}_4(\text{OH})_2$  adapted from Ref. [40].

Phase V surrounds phase I, III and IV. This phase is a spin density wave state with propagation vector  $\mathbf{Q} = (0; k_y; 0.5)$  shifting with magnetic field [48]. Recent experimental results point in the direction of another phase VI close to the saturation region [40]. This phase would present nematic correlations and a possible two magnon gap. The effect of the Dzyaloshinsky-Moriya interaction on this compound is yet to be theoretically analysed. We show the phase diagram from Ref. [40] in Fig. 2.4(c).



# 3 The ferromagnetic frustrated $J_1$ - $J_2$ chain

## 3.1 Introduction

The one-dimensional quantum world of spin-chain systems connects some of the most advanced concepts from many-body physics, such as integrability and symmetry-protected topological order [52], with the measurable physical properties of real materials. An example is the presence of the Haldane phase [53] in spin-1 chains, which is a topological ground state protected by global  $Z_2 \times Z_2$  symmetry [54, 55]. On the other hand frustrated magnets, in which a macroscopic number of quasi-degenerate states compete with each other, are an ideal playground for the emergence of exotic phenomena [56]. For instance, the interplay of frustration and fluctuations leads to unexpected condensed matter orders at low temperatures by spontaneously breaking of either a continuous or discrete symmetry, i.e., order by disorder [57]. A prototype for the interplay of low-dimensionality and geometric frustration is the so called  $J_1$ - $J_2$  chain, with NN  $J_1$  and NNN  $J_2$  coupling, the Hamiltonian of which is given by

$$H = J_1 \sum_i \mathbf{S}_i \cdot \mathbf{S}_{i+1} + J_2 \sum_i \mathbf{S}_i \cdot \mathbf{S}_{i+2}, \quad (3.1)$$

where  $\mathbf{S}_i$  are spin- $\frac{1}{2}$  operator at sites  $i$ . This model exhibits frustration for AFM  $J_2$  ( $J_2 > 0$ ) and both signs of  $J_1$ . While the ground state of the AFM  $J_1$ - $J_2$  chain is well understood [36, 37, 38], assisted by the exact solution of the Majumdar-Ghosh model for  $\alpha = 0.5$  [58]; the ground and excited state properties of the FM  $J_1$ - $J_2$  chain are still not completely identified. It is known that a phase transition occurs at  $\alpha = \frac{1}{4}$  [59, 60] from a FM to an incommensurate spiral state [61, 62] with dimerisation order [63], but the quantitative estimation of the spin gap (if it exists) and its numerical confirmation have been a long standing challenge - so far there is only a field-theoretical prediction of an exponentially small spin gap for  $\alpha \gtrsim 3.3$  [64, 65].

The FM  $J_1$ - $J_2$  chain is used as a standard magnetic model for quasi-one-dimensional edge-shared cuprates such as  $\text{Li}_2\text{CuO}_2$  [66],  $\text{LiCuSbO}_4$  [43],  $\text{LiCuVO}_4$  [67],  $\text{Li}_2\text{ZrCuO}_2$  [39],  $\text{Rb}_2\text{Cu}_2\text{Mo}_3\text{O}_{12}$  [68] and  $\text{PbCuSO}_4(\text{OH})_2$  [69]. Especially, multimagnon bound state [70] and multipolar ordering [71] under magnetic field have been established both theoretically and experimentally in this context.

In this chapter, we numerically prove the existence of a gapped state in the FM  $J_1$ - $J_2$  chain and describe the ground state configuration supporting the spin gap, finding a topologically non-trivial ground state in Sec. 3.2. We then introduce a dimerisation in the first-neighbour interaction, extending our model to a  $J_1$ - $J'_1$ - $J_2$  chain. The reason for introducing a dimerised interaction in the Hamiltonian lies in the properties of real materials, where NN bonds are not equal. In particular, two of the cuprate chains listed above are expected to exhibit explicit dimerisation:  $\text{LiCuSbO}_4$  [43] and  $\text{Rb}_2\text{Cu}_2\text{Mo}_3\text{O}_{12}$ .

---

Parts of this chapter have been published as SciPost Phys. **6**, 19 (2019) and Phys. Rev. B **95**, 220404(R) (2017)

The anisotropic frustrated spin-chain cuprate  $\text{LiCuSbO}_4$  was recently reported to exhibit a magnetic field-induced “hidden” spin-nematic state [43]. By the nuclear magnetic resonance technique, a field-induced spin gap was observed above a field  $\sim 13\text{T}$  in the measurements of the  $^7\text{Li}$  spin relaxation rate  $T_1^{-1}$ , supported by static magnetisation and electron spin resonance data. This material has a unique crystal structure: In the  $\text{CuO}_2$  chain, four nonequivalent  $\text{O}^{2-}$  ions within a  $\text{CuO}_4$ -plaquette give rise to two kinds of nonequivalent left and right Cu-Cu bonds along the chain direction. This gives rise to alternating nearest-neighbour transfer integrals ( $t_1 \neq t'_1$ ). As a result, a sizeable splitting of the two NN FM exchange integrals was estimated:  $J_1 \approx -160\text{K}$  and  $J'_1 \approx -90\text{K}$ , whereas the NNN AFM coupling is  $J_2 \approx 37.6\text{K}$  [see Fig. 3.11(a)]. Another example of a FM dimerised chain compound is  $\text{Rb}_2\text{Cu}_2\text{Mo}_3\text{O}_{12}$  which has  $\text{CuO}_2$  ribbon chains. Here its ribbon chains are twisted, so that the Cu-Cu distances and the Cu-O-Cu angles are slightly alternating. Accordingly, a small dimerisation of the nearest-neighbour exchange integrals is expected. Assuming no dimerisation, the values of the FM nearest- and AFM next-nearest-neighbour exchanges have been estimated as  $-138\text{K}$  and  $51\text{K}$ , respectively, by the fitting of susceptibility and magnetization [72]. Besides, a non-magnetic ground state with energy gap  $E_g \sim 1.6\text{K}$  has been experimentally detected [73]. The Hamiltonian for the dimerised model is

$$H = J_1 \sum_{i=\text{odd}} \mathbf{S}_i \cdot \mathbf{S}_{i+1} + J'_1 \sum_{i=\text{even}} \mathbf{S}_i \cdot \mathbf{S}_{i+1} + J_2 \sum_i \mathbf{S}_i \cdot \mathbf{S}_{i+2}, \quad (3.2)$$

We study the phase diagram as a function of the dimerisation and frustration parameters in Sec. 3.3. We define the phase transition line from the FM gapless to the gapped state using spin wave theory. The gapped region supports a crossover between two different AKLT-like VBS states.

## 3.2 Frustrated ferromagnetic $J_1$ - $J_2$ chain

In this section, we focus on the FM  $J_1$ , AFM  $J_2$  chain. We refer to this system as FM  $J_1$ - $J_2$ . The Hamiltonian is given by eq. (3.1), with  $J_1 < 0$  and  $J_2 > 0$ . This chain system can be also represented as a zigzag ladder [Fig. 3.1(a)] or a diagonal ladder [Fig. 3.1(b)-(d)]. The frustration is parametrised as  $\alpha = J_2/|J_1|$ .

Our aim is to determine the ground state and spin gap of the FM  $J_1$ - $J_2$  chain. To this end, we calculate various quantities including spin gap, string order parameter, several dimerisation order parameters, dimer-dimer correlation function, spin-spin correlation function, and entanglement entropy using DMRG. First, we verify the existence of a finite spin gap at  $\alpha > \frac{1}{4}$  and find its maximum around  $\alpha = 0.6$ . Next, we show that the ground state is a VBS state with spin-singlet formations between third-neighbour sites (which we refer to as the “ $\mathcal{D}_3$ -VBS state”), which leads to the finite spin gap. The leading mechanism for the emergence of this ordered state is magnetic frustration, which is characterised by the presence of strong quantum fluctuations: while the classical ground state is highly degenerate, quantum fluctuations in the system lift this degeneracy with formation of FM dimers and valence bonds, thus we are observing the formation of *order by disorder*. Remarkably, this VBS state is associated with an Affleck-Kennedy-Lieb-Tasaki (AKLT) [74]-like topological hidden order (see Sec. 3.2.1). While there exist



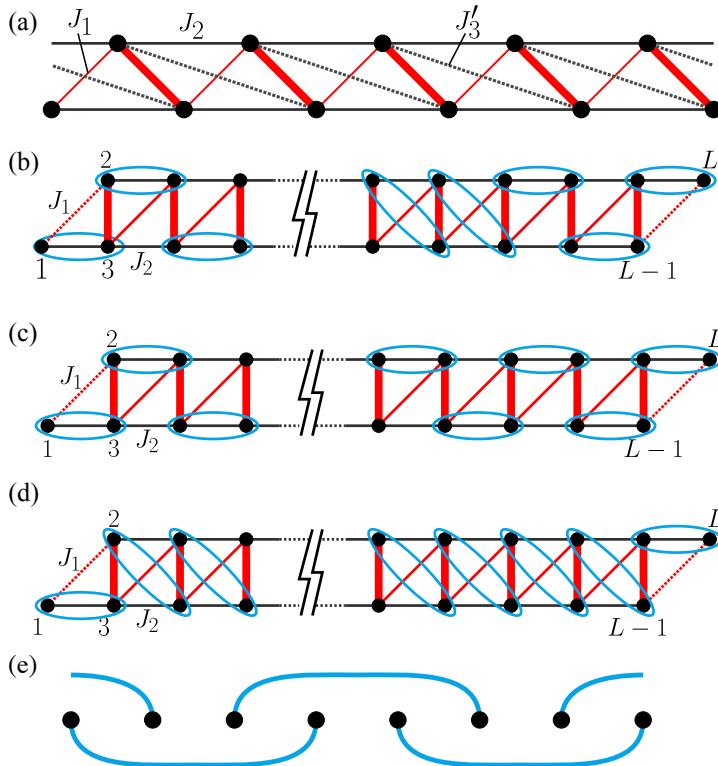


Figure 3.1: (a) Lattice structure of the  $J_1$ - $J_2$  chain (at  $J'_3 = 0$ ) as a zigzag ladder. The  $J_1$  chain is shown in red. Bold lines represent spin-triplet dimers, which are spontaneously formed in the VBS state. Dotted lines show the third-neighbour  $J'_3$  bonds (see text). (b), (c), (d) Three candidates for the VBS ground state of the FM  $J_1$ - $J_2$  chain. Red bold line represent effective  $S = 1$  site as spin-triplet pairs of two spin- $\frac{1}{2}$  sites, blue ellipses represent spin-singlet pairs, i.e., valence bonds. The dashed  $J_1$  bonds at the chain edges are set to be zero in most of our calculations. (d) Schematic picture of the third-neighbour VBS ground state (“ $\mathcal{D}_3$ -VBS state”) of the FM  $J_1$ - $J_2$  chain.

examples of order by disorder in quantum chains (e.g. Majumdar-Ghosh model [58]), we are not aware of previous example of *topological order by disorder*. We support the topological nature of the  $\mathcal{D}_3$ -VBS state by computing the entanglement spectrum (ES) of the system. We confirm the robustness of the  $\mathcal{D}_3$ -VBS state by considering an adiabatic connection of the ground state to the enforced third-neighbour dimerised state.

### 3.2.1 AKLT model

In 1987, Affleck, Kennedy, Lieb and Tasaki presented a result about a new magnetic state they called a VBS [74]. This state, when present in one-dimensional AFM, features a Haldane gap, hence being the first exact solution following Haldane’s suggestion in 1983 [53]. A VBS state is constructed as follows: first, note that a good basis for any spin-singlet states of spin- $\frac{1}{2}$  AFM consists of all possible products of pair contractions of spins into singlets (referred to as *valence bonds*). We can then rewrite any spin  $s$  by symmetrising  $2s$  spin- $\frac{1}{2}$  variables. Now, we can express our spin-singlet state in terms of

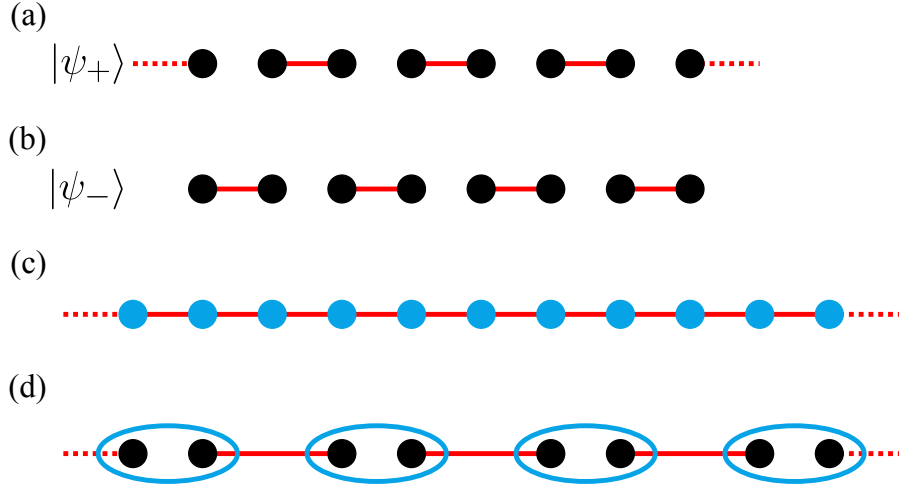


Figure 3.2: (a) and (b) show the two possible ground states for the MG model. Black dots represent  $S = \frac{1}{2}$  sites. (c) shows the  $S = 1$  AFM chain. Blue dots represent  $S = 1$  sites. (d) shows the AKLT-state. Blue ellipses represent  $S = 1$  sites, black dots are the virtual  $S = \frac{1}{2}$ , red lines represent the valence bonds in all figures.

$2s$  valence bonds emanating from each site and terminating on different sites.

It is important to notice that this state does not break translational symmetry, marking a difference with a dimerised state. One important example of a dimerised spin chain is the Majumdar-Ghosh (MG) model. The MG model is an extension of the AFM Heisenberg spin- $\frac{1}{2}$  chain in which a NNN AFM interaction is added. This NNN interaction is set to be half of the nearest neighbours one and the Hamiltonian reads:

$$\mathcal{H}_{\text{MG}} = J \sum_i^N \mathbf{S}_i \cdot \mathbf{S}_{i+1} + \frac{J}{2} \sum_i^N \mathbf{S}_i \cdot \mathbf{S}_{i+2} = J \sum_i^N \left[ (\mathbf{S}_i + \mathbf{S}_{i+1} + \mathbf{S}_{i+2})^2 - \frac{6}{9} \right]. \quad (3.3)$$

This system is exactly solvable and features two possible ground states composed of neighbouring pairs forming singlets as shown in Figs. 3.2(a-b). The two states  $|\psi_+\rangle$  and  $|\psi_-\rangle$  break translational symmetry going from a period of 1 to a period of 2. The ground state is then given by the superposition of these two solutions:  $|\psi\rangle_{\text{MG}} = \frac{1}{\sqrt{2}}(|\psi_+\rangle + |\psi_-\rangle)$ . On the other hand, we can consider the  $s = 1$  AFM chain in a VBS state shown in Fig. 3.2(c). Using the same representation as in Figs. 3.2(a-b), we can re-draw it explicating the virtual spin- $\frac{1}{2}$  as in Fig. 3.2(d). It is then clear that a VBS does not break translational symmetry. Moreover, a VBS exhibits a gap and short-range correlations.

Consider again the spin-1 chain as in Fig. 3.2(d). A similar projection method to the one used for the MG model can be applied. The VB forming at each neighbouring pair implies that the total spin of each pair cannot be 2. We can then use the projection operator onto spin 2 for each pair to define the Hamiltonian as:

$$\mathcal{H}_{\text{AKLT}} = \sum_i \mathcal{P}_2(\mathbf{S}_i + \mathbf{S}_{i+1}) \quad (3.4)$$

$$= \sum_i \left[ \frac{1}{2} \mathbf{S}_i \cdot \mathbf{S}_{i+1} + \frac{1}{6} (\mathbf{S}_i \cdot \mathbf{S}_{i+1})^2 + \frac{1}{3} \right]. \quad (3.5)$$

Clearly,  $\langle \mathcal{H} \rangle \geq 0$ . Affleck, Kennedy, Lieb and Tasaki have shown that a ground state  $|\psi\rangle_{\text{AKLT}}$  exists such that  $\mathcal{H}|\Omega\rangle = 0$ . Using modern notation, we now call this ground state a matrix product state (MPS). In fact, this state can be written in terms of matrices as:

$$|\psi\rangle_{\text{AKLT}} = \sum_{\mathbf{s}} \text{Tr}(A^{s_1} A^{s_2} \dots A^{s_L}) |\mathbf{s}\rangle, \quad (3.6)$$

where  $|\mathbf{s}\rangle = |s_1, s_2, \dots, s_L\rangle$  represents the state of the chain with  $|s_i\rangle = |+\rangle, |0\rangle, |-\rangle$  and  $A^{s_i}$  are  $2 \times 2$  matrices defined as:

$$A^+ = \sqrt{\frac{2}{3}}\sigma^+ \quad A^0 = -\frac{1}{\sqrt{3}}\sigma^0 \quad A^- = -\sqrt{\frac{2}{3}}\sigma^- \quad (3.7)$$

with  $\sigma^\pm = \frac{1}{2}(\sigma^x \pm i\sigma^y)$  and  $\sigma^{x,y,z}$  are the standard Pauli matrices.

Having defined the ground state of the spin-1 AKLT VBS, we can now look into its properties. First of all, it has hidden AFM order, i.e., when removing all the  $S^z = 0$  sites, the remaining non-zero sites will alternate between  $+1$  and  $-1$  in the standard  $S^z$  basis. Moreover, if we consider an open chain, zero-energy spin- $\frac{1}{2}$  excitations can appear at the edges [54], making the ground state 4-fold degenerate and giving us the first hint that this state is topologically non trivial, as the spin- $\frac{1}{2}$  edge states are an example of *fractionalisation*. The first property can be detected using the string order parameter introduced by Den Nijs and Rommelse in 1989 [75]:

$$\mathcal{O}_{\text{string}}^\gamma = - \lim_{|k-j| \rightarrow \infty} \langle (S_k^\gamma) \exp(i\pi \sum_{l=k+1}^{j-1} S_l^\gamma) (S_j^\gamma) \rangle, \quad (3.8)$$

with  $\gamma = x, y$  or  $z$ . The second property is seen in system with open boundary conditions as it is then possible to detect 4 nearly-degenerate states in the lowest part of the spectrum, separated by a Haldane gap from the rest.

These two properties are common to the whole Haldane phase, including the Heisenberg point. Let us rewrite the AKLT Hamiltonian as

$$\mathcal{H}_{\text{Haldane}} = \sum_i^L [\mathbf{S}_i \cdot \mathbf{S}_{i+1} + \lambda(\mathbf{S}_i \cdot \mathbf{S}_{i+1})^2]. \quad (3.9)$$

This system is in the Haldane phase for  $-1 < \lambda < 1$  and it describes the same system as Eq. (3.5) for  $\lambda = 1/3$ , while the model originally studied by Haldane corresponds to  $\lambda = 0$ . With this Hamiltonian, we can prove the two properties in a more rigorous way. Let us consider the non-local unitary transformation introduced by Oshikawa [55]:

$$\mathcal{U} = \prod_{j < k} e^{i\pi S_j^z S_k^x}. \quad (3.10)$$

If we apply it to Eq. (3.9) with  $\lambda = 0$ , i.e, to the Haldane chain, we get

$$\tilde{\mathcal{H}} = \mathcal{U}^{-1} \left( \sum_i^L \mathbf{S}_i \cdot \mathbf{S}_{i+1} \right) \mathcal{U} \quad (3.11)$$

$$= \sum_i^L \left( S_i^x e^{i\pi S_{i+1}^x} S_{i+1}^x + S_i^y e^{i\pi(S_i^z + S_{i+1}^x)} S_{i+1}^y + S_i^z e^{i\pi S_i^z} S_{i+1}^z \right) \quad (3.12)$$

The transformed Hamiltonian  $\tilde{\mathcal{H}}$  shows a global discrete symmetry given by  $\pi$ -rotations along  $x, y, z$  axes, i.e., a  $\mathbf{Z}_2 \times \mathbf{Z}_2$  global symmetry.

Applying the same transformation to Eq. (3.8) with  $\gamma = z$  we obtain

$$\mathcal{U}^{-1} \mathcal{O}_{\text{string}}^z \mathcal{U} = \lim_{|k-j| \rightarrow \infty} S_j^z S_k^z \quad (3.13)$$

which measures FM order in the transformed system described by Eq. (3.12).

Following this line of reasoning, we conclude the Haldane phase described by Eq. (3.9) is stabilised by a  $\mathbf{D}_2 = \mathbf{Z}_2 \times \mathbf{Z}_2$  symmetry. Moreover, we can talk about *hidden order*, as this  $\mathbf{Z}_2 \times \mathbf{Z}_2$  comes from the underlying spin-1/2 virtual degrees of freedom, as it is obvious in the open chain. We would like to point out that this is not the only symmetry that can stabilise the Haldane phase, as demonstrated in Ref. [52]. This is, however, the only one that allows for a non vanishing string order parameter.

### 3.2.2 Methods

In the studying the FM  $J_1$ - $J_2$  chain, we apply open boundary conditions (OBC) unless stated otherwise. Besides, both edged  $J_1$ 's (denoted as  $J_1^{\text{edge}}$ ) are taken to be zero in the open chain. This has an important physical implication which will be clarified in the following. This enables us to calculate ground-state and low-lying excited-state energies, as well as static quantities, quite accurately for very large systems. It puts us in the position to carry out an accurate finite-size-scaling analysis to obtain energies and quantities in the thermodynamic limit. In our DMRG calculations, we keep up to  $m = 6000$  density-matrix eigenvalues in the renormalization procedure. Moreover, several chains with length up to  $L = 800$  are studied to perform finite size scaling. This way, we are able to obtain accurate results with error in the energy  $\Delta E/L < 10^{-11}$ . In some cases we study larger systems up to  $L = 3000$  to estimate the decay length of the spin-spin correlation function and entanglement entropy.

### 3.2.3 Spin gap

Although the existence of a tiny spin gap was predicted by the field-theoretical analyses [64, 65], it has not been numerically detected so far. In our DMRG calculations, the spin gap  $\Delta$  is defined as the energy difference between the singlet ground state and the triplet first excited state:

$$\Delta(L) = E_0(L, S^z = 1) - E_0(L, S^z = 0); \quad \Delta = \lim_{L \rightarrow \infty} \Delta(L), \quad (3.14)$$

where  $E_0(L, S^z)$  is the ground state energy of a system of size  $L$  and total spin  $z$ -component  $S^z$ . As mentioned above, we set  $J_1^{\text{edge}} = 0$ ; otherwise, one cannot measure

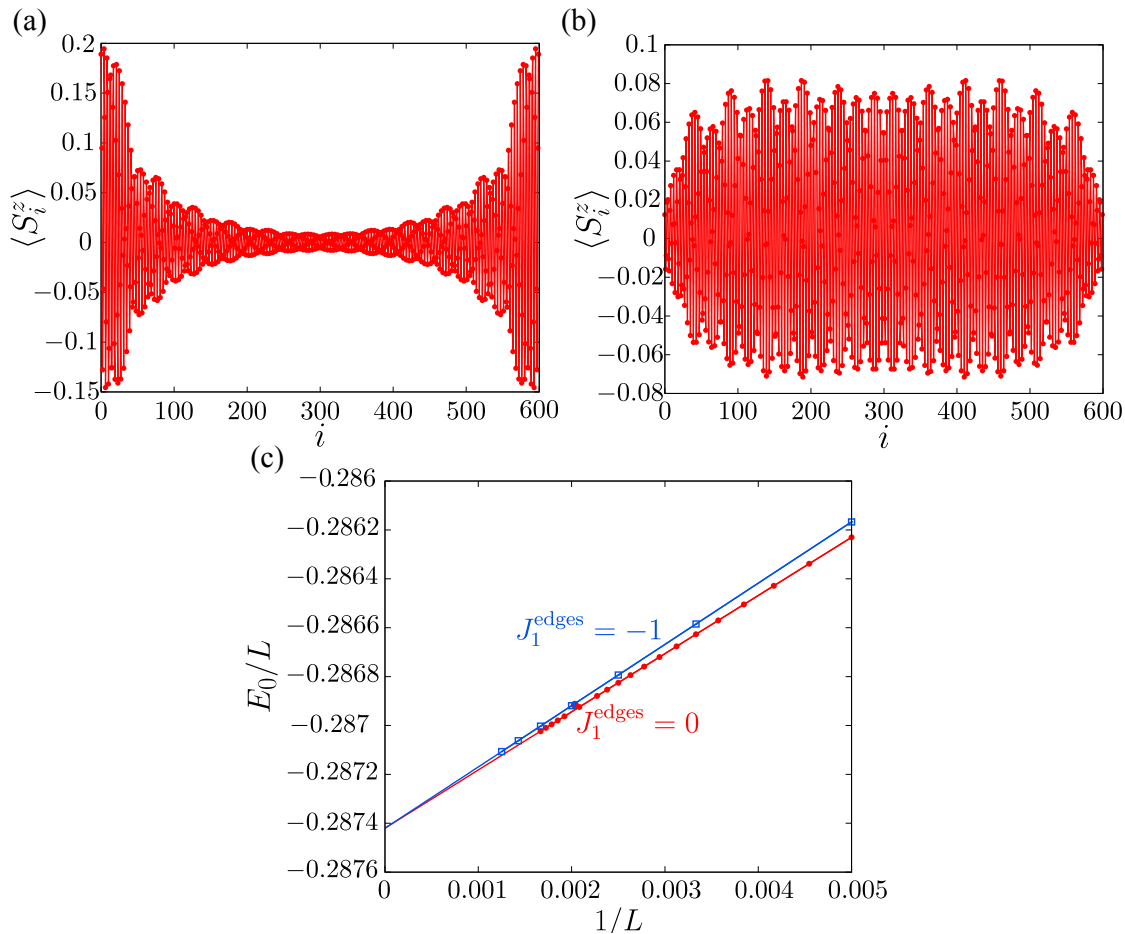


Figure 3.3: Expectation value of the  $z$ -component of local spin  $\langle S_i^z \rangle$  in the first-excited triplet state (total  $S^z = 1$ ) as a function of site position  $i$  at  $\alpha = 0.6$  with  $L = 600$  for (a)  $J_1^{\text{edge}} = -1$  and (b)  $J_1^{\text{edge}} = 0$ . (c) Finite-size scaling of the lowest-state energy with total  $S^z = 0$  for  $J_1^{\text{edge}} = -1$  and  $J_1^{\text{edge}} = 0$  at  $\alpha = 0.6$ . A linear fitting is performed in both cases.

correctly the excitation energy for the bulk system. As shown below, our system is spontaneously dimerised along the FM  $J_1$  chain. By regarding the ferromagnetically dimerised NN bond as a  $S = 1$  site, the system can be considered as a  $S = 1$  Heisenberg chain. In fact, this setting  $J_1^{\text{edge}} = 0$  corresponds to an explicit replacement of  $S = 1$  spin at each end by  $S = \frac{1}{2}$  spin in the  $S = 1$  Heisenberg open chain. It is known that this procedure is necessary to numerically calculate the Haldane gap as a singlet-triplet excitation defined by Eq.(3.14) because a  $S = \frac{1}{2}$  degree of freedom appears as an unpaired (nearly) free spin at both edges, i.e., so-called edge spin state, in the  $S = 1$  Heisenberg open chain. The appearance of edge spin states is a definite signature of the Haldane state. To illustrate the presence of edge spin states in our model, we plot the expectation value of the local spin  $z$ -component, i.e.  $\langle S_i^z \rangle$ , in the  $S^z = 1$  first-excited triplet state as a function of site position  $i$  at  $\alpha = 0.6$  for  $L = 600$ . As shown in Fig. 3.3(a), when we naively keep  $J_1^{\text{edge}} = -1$ , the spin flipped from the singlet ground state (spinon) is mostly localised around the chain edges. It resembles the fact that a residual  $S = 1/2$  edge

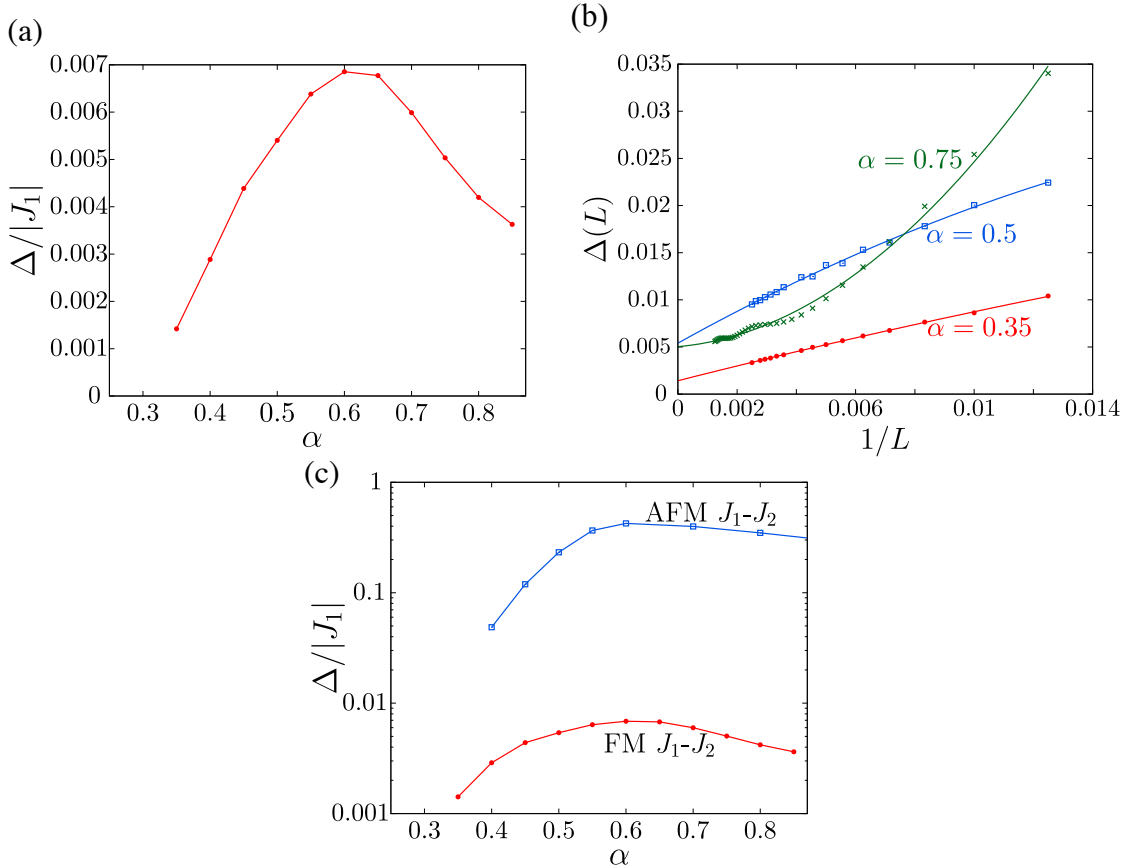


Figure 3.4: (a) Spin gap  $\Delta/|J_1|$  of the  $J_1$ - $J_2$  chain as a function of the degree of frustration  $\alpha$ . (b) Examples of finite size scaling of the spin gap for  $\alpha = 0.35$  (red line),  $\alpha = 0.5$  (blue line) and  $\alpha = 0.75$  (green line). (c) Comparison between the gaps of the FM  $J_1 - J_2$  and the AFM  $J_1$ - $J_2$  chain on a semilog scale.

spin (out of a valence bond) in the 1D  $S = 1$  Heisenberg model can be flipped without energy cost. In this case, the excitation energy, i.e. the spin gap, is zero or significantly underestimated. It thus prevents us from estimating the bulk spin gap correctly. Whereas in the case of  $J_1^{\text{edge}} = 0$ , the flipped spin is distributed inside the system as seen in Fig. 3.3(b). Therefore, this setting of  $J_1^{\text{edge}} = 0$  enables us to obtain the spin gap after an extrapolation of the singlet-triplet excitation energy to the thermodynamic limit.

Fig. 3.4(a) shows the spin gap in the thermodynamic limit as a function of  $\alpha$ . For information, we present three examples of finite-size scaling analysis for the spin gap in Fig. 3.4(b). We performed second-order polynomial fitting for all values of  $\alpha$ . For  $\alpha \geq 0.6$ , larger system sizes up to  $L = 800$  were taken into account due to the oscillations of the data point reflecting the incommensurate structure. For  $\alpha > 0.85$  the oscillations become a crucial problem and we could not perform a reasonable fitting. The spin gap of the FM  $J_1$ - $J_2$  chain is compared to that for the AFM  $J_1$ - $J_2$  chain in Fig. 3.4(c). For the FM  $J_1$ - $J_2$  chain a finite spin gap is clearly observed in a certain  $\alpha$  region, although it is about two orders of magnitude smaller than that for the AFM  $J_1$ - $J_2$  chain. The spin gap seems to grow continuously from  $\alpha = \frac{1}{4}$  reaching its maximum  $\Delta \simeq 0.007|J_1|$  around  $\alpha = 0.6$ , which is within *the most highly-frustrated region*. This already suggests that the

origin of the spin gap is a frustration-induced long-range order, and the result of *order by disorder*.

We here check to be sure that the artificial setting  $J_1^{\text{edge}} = 0$  does not change the ground state. To study it, we compare the lowest energies at  $\alpha = 0.6$  for the two different values of  $J_1^{\text{edge}}$  in Fig. 3.3(c) as a function of  $1/L$ . We see that at finite  $L$  the energy for  $J_1^{\text{edge}} = 0$  is rather lower than that for  $J_1^{\text{edge}} = -1$ . Nevertheless, they coincide perfectly in the thermodynamic limit ( $1/L = 0$ ); a linear fitting yields  $E_0/L = -0.2874202246$  for  $J_1^{\text{edge}} = -1$  and  $E_0/L = -0.2874200731$  for  $J_1^{\text{edges}} = 0$ . This means that the bulk ground state does not depend on the choice of  $J_1^{\text{edge}}$ .

Additionally, it would be interesting to mention the relation between edge spin states and spinon excitations. Since the spin gap is very small in our system, the spinons are expected to be nearly deconfined. With setting  $J_1^{\text{edge}} = -1$ , the system exhibits spin edge states; thus, a spinon is created at the system edges as an edge spin- $\frac{1}{2}$  excitation in the total  $S^z = 1$  state [see Fig. 3.3(a)]. Typically, the Friedel oscillation decays quickly (with decay length of the order of 1) from the edges in a Haldane gapped system. If the edge spin- $\frac{1}{2}$  is completely free like in the AKLT state, the decay length is 0. However, in our system, it decays very slowly and the amplitude seems to be still sizeable even around the system center for  $L = 600$ . The slow decay of the Friedel oscillation clearly indicates nearly complete deconfinement of spinons. This is also consistent with an exponential decay of the spin-spin correlation with very large decay length,  $\xi \sim 50$  ( $\alpha \sim 0.6$ ) at the minimum.

### 3.2.4 Valence Bond Solid

Having established the existence of a finite spin gap for  $\alpha > \frac{1}{4}$ , we investigate a possible mechanism leading to it. It is known that a spontaneous FM dimerisation is driven along  $J_1$  bonds [64, 65] and an emergent effective spin-1 degree of freedom is created with the dimerised two spin- $\frac{1}{2}$ 's [63]. If the system (3.1) can be mapped onto a  $S = 1$  Heisenberg chain, the finite spin gap might be interpreted as a Haldane gap with a VBS state [74]. However, it is nontrivial whether an arbitrary set of valence bonds, i.e., resonating valence bonds forming in different directions, between the neighbouring effective  $S = 1$  sites leads to a finite spin gap [see Fig. 3.1(b)]. To investigate the stability of the VBS state, we examine the string order parameter. For a spin  $S = 1$  chain, the string order parameter is defined by eq. (3.8) and we consider  $\gamma = z$ . In our system, the resultant spin of two  $S = 1/2$  spins forming a spin-triplet pair is regarded as an effective  $S = 1$  spin. Hence, Eq. (3.8) can be rewritten in term of  $S = 1/2$  spins as

$$\mathcal{O}_{\text{string}}^z = - \lim_{|k-j| \rightarrow \infty} \langle (S_k^z + S_{k+1}^z) \exp(i\pi \sum_{l=k+2}^{j-1} S_l^z) (S_j^z + S_{j+1}^z) \rangle, \quad (3.15)$$

where  $S_i^z$  is the  $z$ -component of a spin-1/2 operator at site  $i$ . Considering that the  $z$ -component of a spin-1/2 spin can only take the values  $S^z = \pm 1/2$ , we have

$$\exp(i\pi S_l^z) = i \sin(\pm\pi/2) = \pm i,$$

since  $\cos(\pm\pi/2) = 0$ . Taking pairs of spins  $S_i^z S_{i+1}^z$  (within an effective spin-1 site), we get a relation

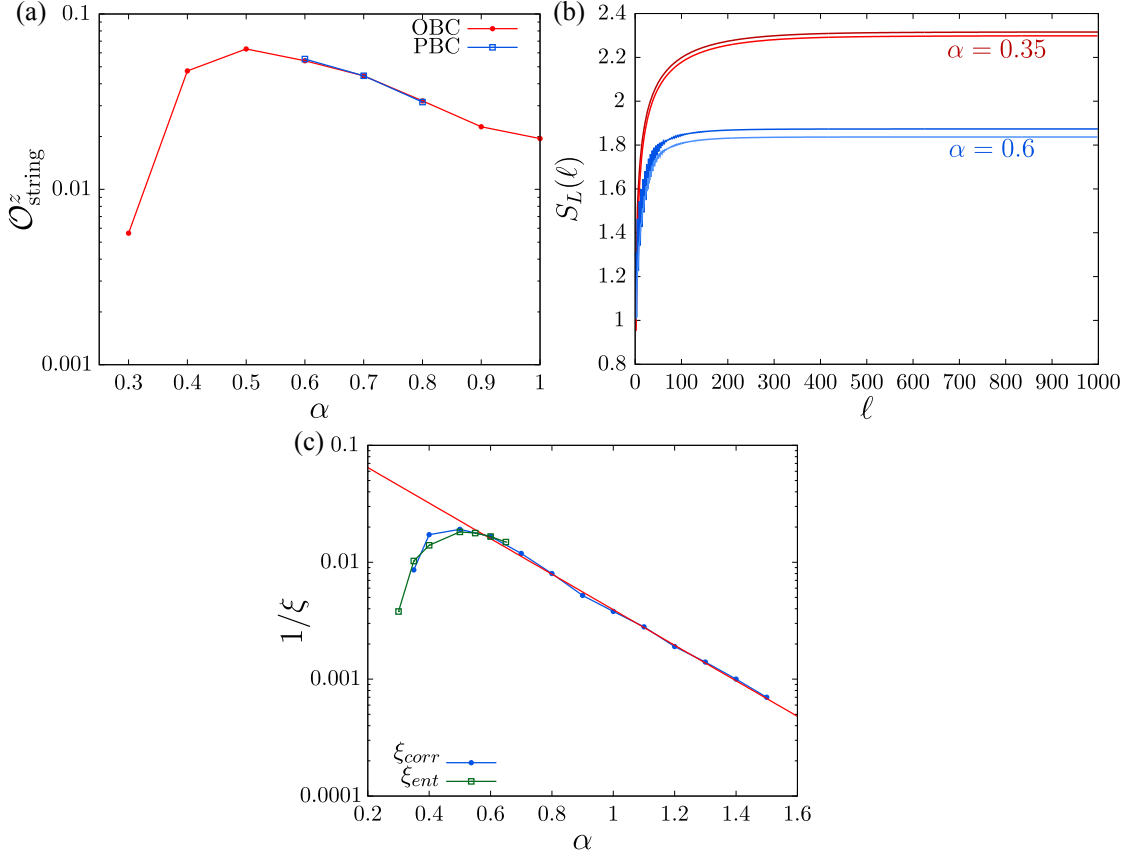


Figure 3.5: (a)String-order parameter as a function of  $\alpha$ . Red (blue) line refers to open (periodic) boundary conditions. (b) Entanglement entropy as a function of the subsystem length  $l$ . (c) Inverse of the decay length estimated from the spin-spin correlation ( $\xi_{\text{corr}}$ ) and the entanglement entropy ( $\xi_{\text{ent}}$ ) as a function of  $\alpha$ . Red line is a fit with the exponential function  $1/\xi_{\text{corr}} = 0.13 \exp(-0.35\alpha)$ .

$$\exp[i\pi(S_l^z + S_{l+1}^z)] = -4S_l^z S_{l+1}^z,$$

where the coefficient 4 accounts for renormalising the  $1/4$  factor from multiplying two spin- $1/2$ 's. Finally, we obtain a simplified string order parameter:

$$\mathcal{O}_{\text{string}}^z = - \lim_{|k-j| \rightarrow \infty} (-4)^{\frac{j-k-2}{2}} \langle (S_k^z + S_{k+1}^z) \prod_{l=k+2}^{j-1} S_l^z (S_j^z + S_{j+1}^z) \rangle, \quad (3.16)$$

which is expressed only by products of  $S^z$  and can be computed within our DMRG code.

The two-fold degeneracy due to the FM dimerisation of the ground state is lifted under OBC and the value of  $\mathcal{O}_{\text{string}}^z$  is different for even and odd  $j$  ( $k$ ). We thus take their average obtained with  $(k, j) = (\frac{L}{4}, \frac{3L}{4})$  and  $(k, j) = (\frac{L}{4} + 1, \frac{3L}{4} - 1)$ . We confirm the validity of this method by checking the agreement of the OBC results with those obtained under periodic boundary conditions keeping  $|k - j| = \frac{L}{2}$ . In Fig. 3.5(a) the string order parameter in the thermodynamic limit is plotted as a function of  $\alpha$ . The finite value of  $\mathcal{O}_{\text{string}}^z$  suggests the formation of a VBS state with a hidden topological long-range



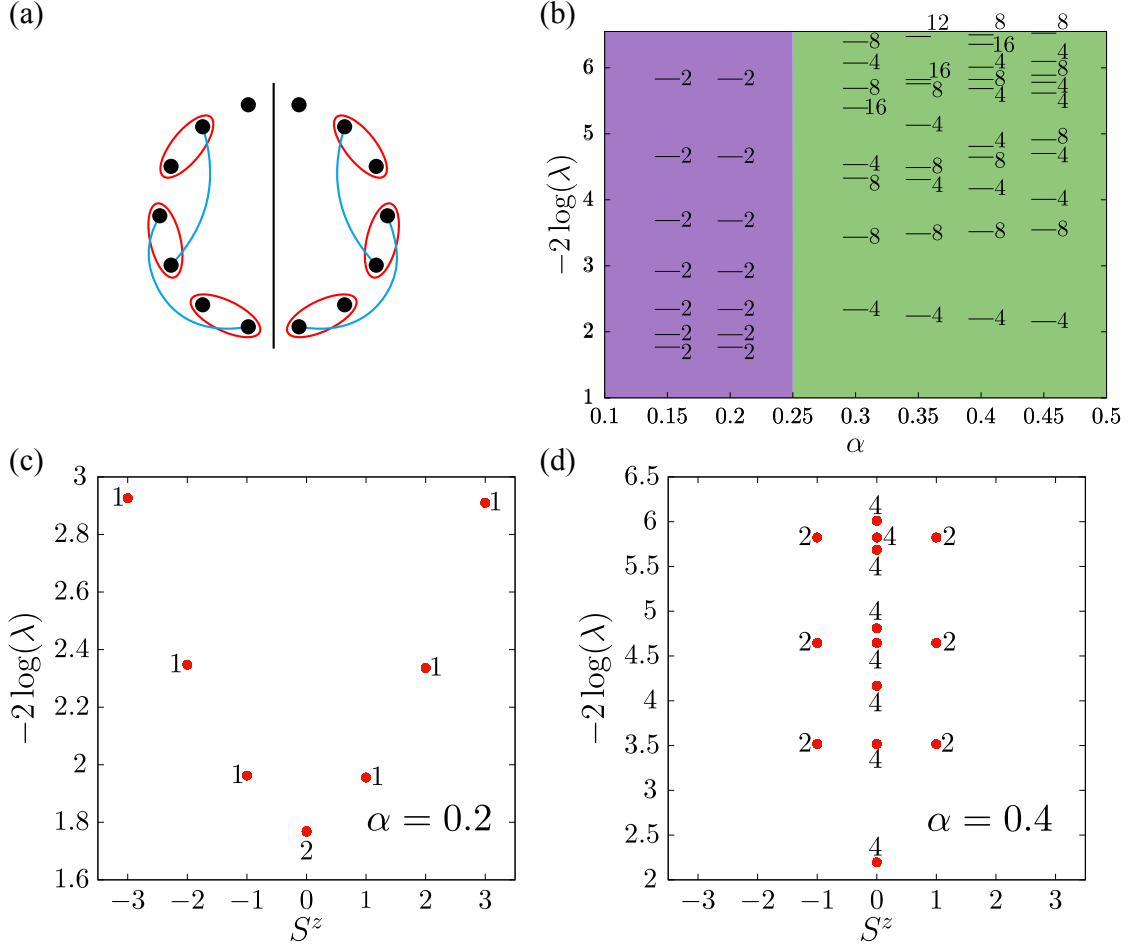


Figure 3.6: (a) Depiction of the cutting of the system with PBC. Red ellipses represent effective  $S = 1$ , blue lines represent singlet formation between third-neighbours. (b) ES as a function of  $\alpha$ , lilac area shows the FM region, green one is the  $\mathcal{D}_3$ -VBS state.  $\lambda$  are the eigenstates of  $\rho_\ell$ . (c)(d) ES as a function of  $S^z$  for (c)  $\alpha = 0.2$  (FM) and (d)  $\alpha = 0.4$  ( $\mathcal{D}_3$ -VBS).

order. The string order vanishes when approaching  $\alpha = \frac{1}{4}$ , indicating a second-order phase transition at the FM critical point. With increasing  $\alpha$ , it goes through a maximum at  $\alpha \simeq 0.55$ , which is roughly consistent with the maximum position of the spin gap, and tends slowly towards zero in the limit  $\alpha \rightarrow \infty$ . The maximum value  $\mathcal{O}_{\text{string}}^z \sim 0.06$  is much smaller than  $\mathcal{O}_{\text{string}}^z = \frac{4}{9} \simeq 0.4444$  for the *perfect* VBS state for the AKLT model [74] and  $\mathcal{O}_{\text{string}}^z \simeq 0.3743$  for the  $S = 1$  Heisenberg chain [76]. This means that our VBS state is very fragile which is the reason why it is so difficult to detect the spin gap numerically.

### 3.2.5 Entanglement entropy and spectrum

The criticality of a 1D system can be definitely identified by its entanglement structure. The full density matrix of the system is  $\rho = |\Psi\rangle\langle\Psi|$ , with  $|\Psi\rangle$  being the many body ground state of the system. We consider a cut dividing our system in two subsystems  $A$

and  $B$ . The reduced density matrix for the subsystem  $A$  is defined as:

$$\rho_A = \text{Tr}_B |\Psi\rangle \langle \Psi|. \quad (3.17)$$

We then define the von Neumann entanglement entropy of the subsystem  $A$  as:

$$S_A = -\text{Tr} \rho_A \log \rho_A. \quad (3.18)$$

Note that  $S_A = S_B$ .

Though the entanglement entropy already gives us some information about the entanglement properties of the system and can be used to derive further quantities, e.g., central charge, it is still only one number. Li and Haldane have shown how this number can be generalised to a more “structured” quantity that can be used to prove the topological nature of a state: the entanglement spectrum (ES) [77]. This spectrum derives naturally from the Schmidt decomposition:

$$|\Psi\rangle = \sum_i e^{-\frac{1}{2}\xi_i} |\Psi_A^i\rangle \otimes |\Psi_B^i\rangle, \quad (3.19)$$

where  $|\Psi_A^i\rangle$  ( $|\Psi_B^i\rangle$ ) are an orthonormal basis on the subsystem  $A$  ( $B$ ). In our calculations, the ES  $\{\xi_i\}$  is simply obtained as  $\xi_i = -\log \lambda_i$ , where  $\{\lambda_i\}$  are the eigenvalues of the reduced density matrices after the bipartite splitting.

We use the von Neumann entanglement entropy of the subsystem with length  $l$ ,  $S_L(l) = -\text{Tr}_l \rho_l \log \rho_l$ , where  $\rho_l = \text{Tr}_{L-l} \rho$  is the reduced density matrix of the subsystem and  $\rho$  is the full density matrix of the whole system. A gapped state is characterised by a saturation of  $S_L(l)$  as a function of  $l$  [78]. In Fig. 3.5(b) the entanglement entropy is plotted as a function of  $l$  with fixed whole system length  $L = 2000$ . We can clearly see the saturation behaviour indicating a gapped ground state. The saturation value is slightly split depending on whether the system is divided inside or outside the effective  $S = 1$  site. In a VBS state,  $S_L(l)$  approaches the saturation value  $S_L^{\text{sat}}$  exponentially, i.e.,  $S_L(l) \sim S_L^{\text{sat}} - a \exp(-l/\xi_{\text{ent}})$ ; while, the spin-spin correlation decays with distance exponentially, i.e.,  $|\langle S_0^z S_r^z \rangle| \sim b \exp(-r/\xi_{\text{corr}})$  [79]. For the AKLT VBS state  $\xi_{\text{ent}}$  and  $\xi_{\text{corr}}$  must coincide, which is indeed what we observe numerically in the  $\mathcal{D}_3$ -VBS state. [see Fig. 3.5(c)] For technical reasons, we could determine the spin gap only for  $\alpha \leq 0.85$ . However, since  $\xi_{\text{corr}} \cdot (\Delta/J_2) = \text{const.}$  is expected in the large  $\alpha$  regime, a tiny but finite gap is expected up to  $\alpha = \infty$ .

To further support the existence of topological order in our system, we computed the ES for several values of  $\alpha$  through the FM critical point. We studied systems of size  $L = 82$  with applying periodic boundary conditions (PBC). We assumed that the system consists of  $L = 4n + 2$  sites and it is divided in half as in Fig. 3.6(a). Since each subsystem includes an odd number of sites, the edge spin state can be directly observed. The results are plotted as a function of  $\alpha$  in Fig. 3.6(b). The FM state ( $\alpha < \frac{1}{4}$ ) has only double degenerate states. The double degenerate state indicates a trivial state because of the area law acting on a periodic system cut at two points (the typical 1-3- degeneracy is not possible due to the impossibility of forming a triplet state, having an odd number of spins). The Haldane phase is thus characterised by a four-fold degeneracy of the entire ES [80]. In fact, our  $\mathcal{D}_3$ -VBS shows  $4n$ -degeneracy in the entire ES. Therefore, we

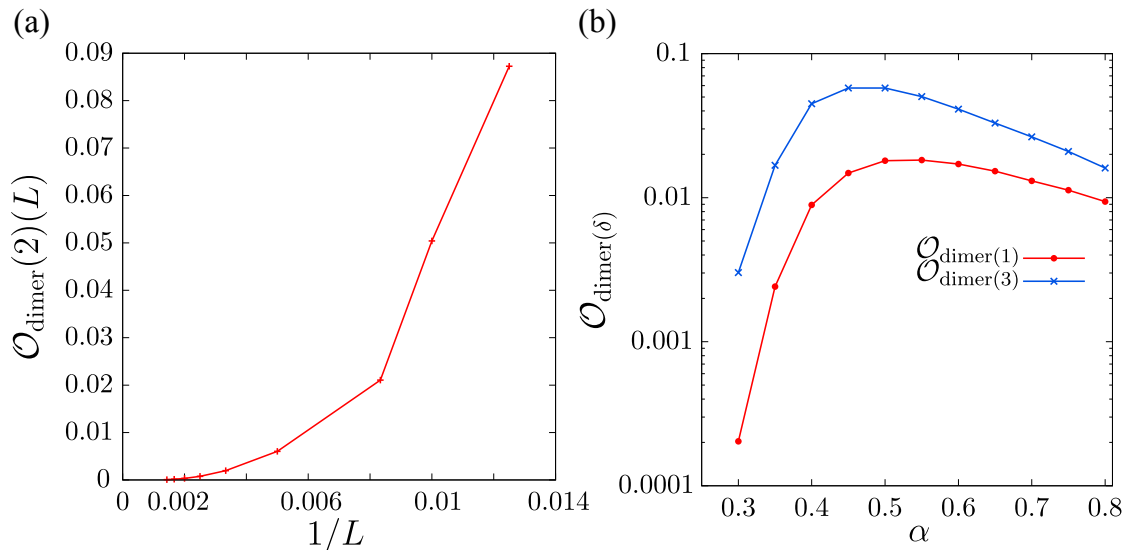


Figure 3.7: (a) Finite-size scaling of the dimer order parameter for NNN bonds ( $\delta = 2$ ) at  $\alpha = 0.6$ . The order parameter is vanishing in the thermodynamical limit. (b) Dimer order parameters for NN ( $\delta = 1$ , red line) and third-neighbour ( $\delta = 3$ , blue line) bonds as a function of  $\alpha$ .

confirmed that our  $\mathcal{D}_3$ -VBS state is an expression of the symmetry protected Haldane state. In Fig. 3.6(c)(d), we show the ES as a function of total spin  $z$ -component of the subsystem  $S^z$  for the FM ( $\alpha = 0.2$ ) and  $\mathcal{D}_3$ -VBS ( $\alpha = 0.4$ ) states: While in the FM state the double degeneracy is lifted for  $S^z \neq 0$  and the spectrum moves away from 0 symmetrically with increasing the Schmidt value, in the  $\mathcal{D}_3$ -VBS state the Schmidt values are  $2n$ -degenerate and the spectrum is dense around  $S^z = 0$  due to the possibility that the free spins in the two subsystems are aligned ( $S^z = 0$ ) or anti-aligned ( $S^z = 1$ ).

### 3.2.6 Dimerisation order

The above analysis makes clear that a gap opens due to the formation of a topologically ordered VBS state but it is not yet obvious how the VBS structure is formed. We can determine a more specific VBS structure by considering the possibility of longer-range dimerisation orders. The dimerisation order parameter between sites distant  $\delta$  is defined as

$$\mathcal{O}_{\text{dimer}}(\delta) = \lim_{L \rightarrow \infty} |\langle \mathbf{S}_{i-\delta} \cdot \mathbf{S}_i \rangle - \langle \mathbf{S}_i \cdot \mathbf{S}_{i+\delta} \rangle|, \quad (3.20)$$

where we take  $i = L/2$  for  $\delta = 1$  and  $i = L/2 - 1$  for  $\delta = 2, 3$  (the extrapolated value in the thermodynamic limit does not depend on these choices). If  $\mathcal{O}_{\text{dimer}}(\delta)$  is finite for  $\delta$ , it signifies a long-range dimerisation order associated with translational symmetry breaking to period of  $4 - 2(\delta \bmod 2)$ . For the case of  $\delta = 2$ ,  $\mathcal{O}_{\text{dimer}}(2)$  goes to zero in

This formula becomes obvious for the  $\delta = 1$  case: A dimerised bond and an undimerised bond appear alternately along the  $J_1$  chain, meaning the symmetry breaking period is 2. For odd values of  $\delta > 1$ , considering the ladder representation as in Fig. 3.1(d), the mirror symmetry between the two  $J_2$  chains is broken and the translational symmetry along the  $J_2$  chains is preserved. It leads to symmetry breaking with period 2 along the  $J_1$  chain. For even values of  $\delta$ , as depicted in Fig. 3.1(c), the translational

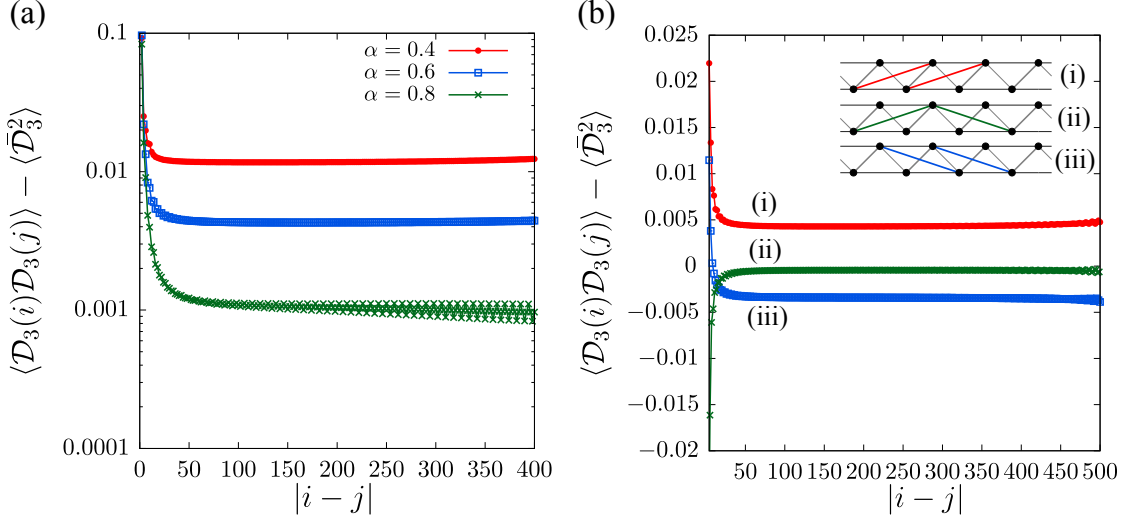


Figure 3.8: (a) Dimer-dimer correlation  $\langle \mathcal{D}_3(i)\mathcal{D}_3(j) \rangle$  as a function of distance  $|i-j|$  for several values of  $\alpha$ . To see the net correlation the product of expectation values  $\langle \bar{\mathcal{D}}_3 \rangle^2$  is subtracted. (b) Dimer-dimer correlation functions for the three different kinds of third-neighbour bonds pairs at  $\alpha = 0.6$ .

the thermodynamic limit, as seen in Fig. 3.7(a). This clearly indicates the absence of long-range dimerisation order along the two  $J_2$  chains like in Fig. 3.1(c). Thus, this VBS state can be excluded as a candidate for the ground state for the FM  $J_1$ - $J_2$  chain. Hence, the possibility of a VBS state with dimerisation along two  $J_2$  chains is excluded. Whereas for  $\delta = 1$  and 3,  $\mathcal{O}_{\text{dimer}}(\delta)$  is finite. In Fig. 3.7(b) the values of  $\mathcal{O}_{\text{dimer}}(1)$  and  $\mathcal{O}_{\text{dimer}}(3)$  in the thermodynamic limit are plotted as a function of  $\alpha$ . Remarkably,  $\mathcal{O}_{\text{dimer}}(3)$  is significantly larger than  $\mathcal{O}_{\text{dimer}}(1)$  despite the longer distance. Moreover, though FM dimerisation between fifth-neighbours and AFM dimerisation between seventh-neighbour may be finite, we expect them to be much smaller than the values reported in Fig. 3.7(b). We also find that  $\langle \mathbf{S}_i \cdot \mathbf{S}_{i+3} \rangle$  is always negative at  $\alpha > \frac{1}{4}$  suggesting that a VBS ground state with third-neighbour valence bonds, i.e.,  $\mathcal{D}_3$ -VBS state, is stabilised as shown in Fig. 3.1(d).

In order to further prove the  $\mathcal{D}_3$ -VBS picture, we calculate the dimer-dimer correlation function defined as

$$\langle \mathcal{D}_3(i)\mathcal{D}_3(j) \rangle - \langle \bar{\mathcal{D}}_3 \rangle^2, \quad (3.21)$$

where  $\mathcal{D}_3(i) = \mathbf{S}_i \cdot \mathbf{S}_{i+3}$  is spin-spin correlation between the third-neighbour sites  $(i, i+3)$  and  $\langle \bar{\mathcal{D}}_3 \rangle$  is the averaged value of  $\mathcal{D}_3(i)$  over  $i = 1, \dots, L$  in the thermodynamic limit. In Fig. 3.8(a) we show the dimer-dimer correlation as a function of the distance  $|i-j|$  for different values of  $\alpha$ . For all  $\alpha$  values a fast saturation with the distance is clearly seen. This directly evidences the presence of the long-range  $\mathcal{D}_3$ -VBS order. In fact, in Fig. 3.8(a) only the correlations for dimer pairs forming valence bond as in Fig. 3.8(b)(i) are shown. It would be informative to see the correlation between the other third-neighbour bond pairs. As expected, the correlation between third-neighbour pairs without valence bond

---

symmetry is broken on the  $J_2$  chain with a twofold structure, and the mirror symmetry between the two  $J_2$  chains is also broken. This leads to a symmetry breaking period of 4 along the  $J_1$  chain.

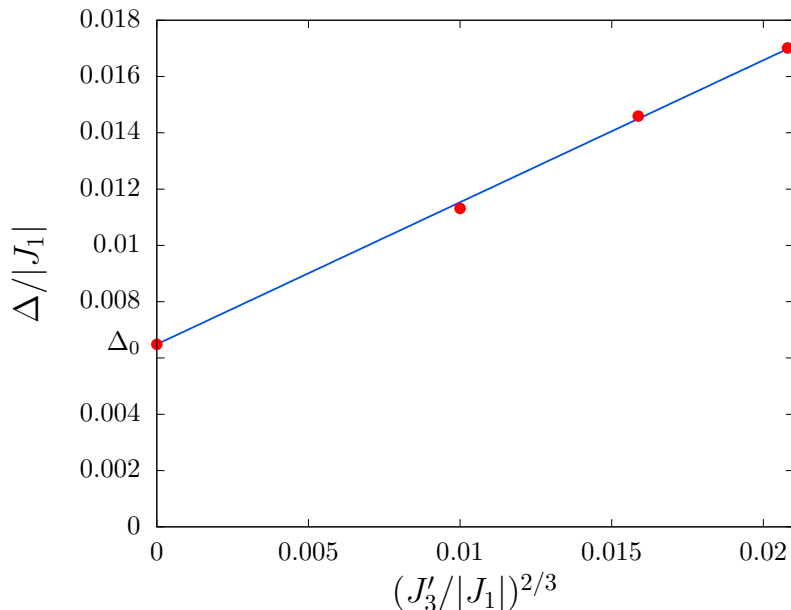


Figure 3.9: Spin gap  $\Delta$  as a function of the third neighbour AFM interaction  $J'_3$  for  $\alpha = 0.6$ . The red line points are data points, the blue line is a linear fitting. We indicate  $\Delta(J'_3 = 0)$  as  $\Delta_0$ . The fitting function yields  $\Delta - \Delta_0 \simeq 0.5046J_3'^{2/3}$ .

saturates to a negative value [Fig. 3.8(b)(iii)] and that between third-neighbour pairs with and without valence bond vanishes [Fig. 3.8(b)(ii)].

Thus, the finite spin gap is related to the emergent spin-singlet formation on every third-neighbour bond. To test this concept, we introduce an explicit AFM exchange interaction  $J'_3 \mathbf{S}_i \cdot \mathbf{S}_{i+3}$  on the third-neighbour bonds [see Fig. 3.1(a)]. Note that  $i$  is chosen to be either even or odd depending on the symmetry breaking pattern; in our open chain  $i$  is taken to be even. The dependence of  $\Delta$  on  $J'_3$  with fixing  $\alpha = 0.6$  is shown in Fig. 3.9. We find that the spin gap is smoothly enhanced by the AFM  $J'_3$ . This means that our ground state is adiabatically connected to an explicit formation of the third-neighbour VBS state by  $J'_3$ . With increasing  $J'_3$  the gap increases like  $\Delta - \Delta(J'_3 = 0) \propto J_3'^{2/3}$ , though small but finite intrinsic dimerisation should exist at  $J'_3 = 0$ . This is qualitatively the same behaviour as in the spin-Peierls transition of the  $S = \frac{1}{2}$  dimerised Heisenberg chain [81]. We thus conclude that the ground state of the system (3.1) is the  $\mathcal{D}_3$ -VBS state depicted in Fig. 3.1(d). If we regard the system (3.1) as a diagonal ladder with effective  $S = 1$  rungs as in Fig. 3.1(d), the  $\mathcal{D}_3$ -VBS state may be interpreted as a symmetry protected state [52] with a *plaquette* unit including two effective  $S = 1$  rungs, i.e., four  $S = \frac{1}{2}$  sites. The plaquette is sketched in the inset of Fig. 3.10(a). The third-neighbour valence bond is locally stabilised in a  $|\sum_{i=1}^4 \mathbf{S}_i| = 1$ , i.e.,  $S^{\text{tot}} = 1$ , sector. The spin gap can be qualitatively estimated from the excitation energy to a state with  $|\sum_{i=1}^4 \mathbf{S}_i| = 2$ , i.e.  $S^{\text{tot}} = 2$ , sector which is projected out from the ground state as in the AKLT model. We plot the excitation energy as a function of  $\alpha$ . We can see that the tendency of  $\Delta$  is qualitatively reproduced by the single plaquette: With increasing  $\alpha$ , the gap starts to increase at  $\alpha = \frac{1}{4}$ , goes through the maximum at  $\alpha = 0.5$ , and then decreases slowly at larger  $\alpha$ . Moreover, in the  $S^{\text{tot}} = 1$  sector the antiferromagnetic spin-spin correlation

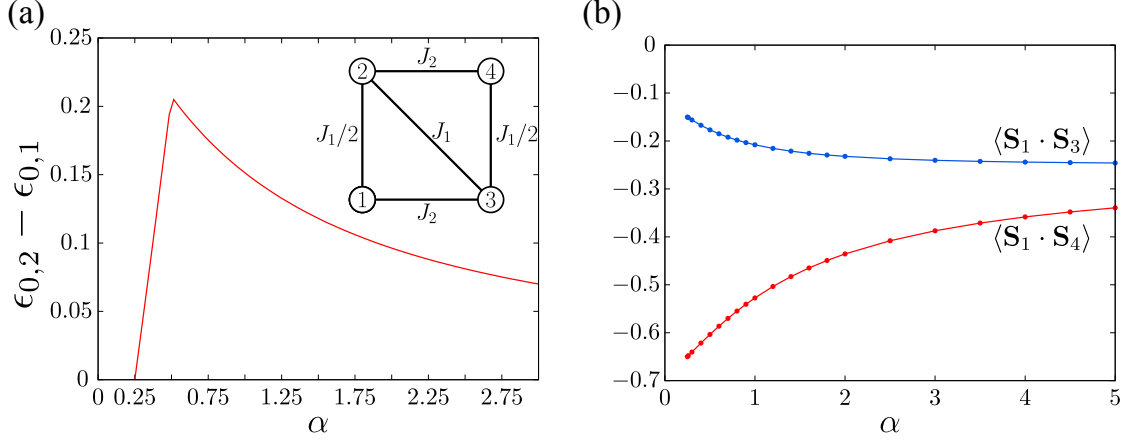


Figure 3.10: (a) Excitation energy from the  $S^{\text{tot}} = 1$  ( $\epsilon_{0,1}$ ) to  $S^{\text{tot}} = 2$  ( $\epsilon_{0,2}$ ) sectors in a single plaquette extracted from the diagonal ladder [Fig. 3.1(d)]. A spin-singlet is formed between sites 1 and 4 in the  $S^{\text{tot}} = 1$  sector. (b) Spin-spin correlations in a single plaquette as a function of  $\alpha$ .

between sites 1 and 4 is much stronger than that between sites 1 and 3 for  $\alpha > 1/4$ . This clearly indicates a spin-singlet formation between sites 1 and 4, which corresponds to the third-neighbour valence bond in our  $\mathcal{D}_3$ -VBS state. Each of the remaining two  $S = 1/2$  spins on sites 2 and 3 forms another spin-singlet with a  $S = 1/2$  spin in the neighbouring plaquette.

### 3.2.7 Matrix product state

Our VBS wave function can be expressed as the matrix product state

$$|\text{VBS}\rangle = \frac{1}{\sqrt{2}} \left[ \text{Tr} \prod_{i \text{ odd}} g_i + \text{Tr} \prod_{i \text{ even}} g_i \right] \quad (3.22)$$

with

$$g_i = \begin{pmatrix} 0 & 1 \\ -1 & 0 \end{pmatrix} \begin{pmatrix} |\uparrow\rangle_{i+1} |\uparrow\rangle_i & |\uparrow\rangle_{i+1} |\downarrow\rangle_i \\ |\downarrow\rangle_{i+1} |\uparrow\rangle_i & |\downarrow\rangle_{i+1} |\downarrow\rangle_i \end{pmatrix} \quad (3.23)$$

where  $|a\rangle_{i+1}|b\rangle_i$  ( $a, b = \uparrow, \downarrow$ ) denotes the spin state of effective  $S = 1$  site created by the original two  $S = \frac{1}{2}$  sites ( $i, i+1$ ). To show this corresponds to our third-neighbours VBS, let us perform a part of the product between two effective  $S = 1$  sites:

$$\begin{aligned} & \begin{pmatrix} |\uparrow\rangle_{i+1} |\uparrow\rangle_i & |\uparrow\rangle_{i+1} |\downarrow\rangle_i \\ |\downarrow\rangle_{i+1} |\uparrow\rangle_i & |\downarrow\rangle_{i+1} |\downarrow\rangle_i \end{pmatrix} \begin{pmatrix} 0 & 1 \\ -1 & 0 \end{pmatrix} \begin{pmatrix} |\uparrow\rangle_{i+3} |\uparrow\rangle_{i+2} & |\uparrow\rangle_{i+3} |\downarrow\rangle_{i+2} \\ |\downarrow\rangle_{i+3} |\uparrow\rangle_{i+2} & |\downarrow\rangle_{i+3} |\downarrow\rangle_{i+2} \end{pmatrix} \\ &= \begin{pmatrix} |\uparrow\rangle_{i+1} |\uparrow\rangle_{i+2} & |\uparrow\rangle_{i+1} |\downarrow\rangle_{i+2} \\ |\downarrow\rangle_{i+1} |\uparrow\rangle_{i+2} & |\downarrow\rangle_{i+1} |\downarrow\rangle_{i+2} \end{pmatrix} \otimes (|\uparrow\rangle_i |\downarrow\rangle_{i+3} - |\downarrow\rangle_i |\uparrow\rangle_{i+3}). \end{aligned} \quad (3.24)$$

A spin-singlet is formed between  $S = 1/2$  spins at sites  $i$  and  $i+3$ , namely, between third-neighbour sites. Since the resultant  $2 \times 2$  matrix has the same form as before, this matrix product state can be extended up to an arbitrary length.

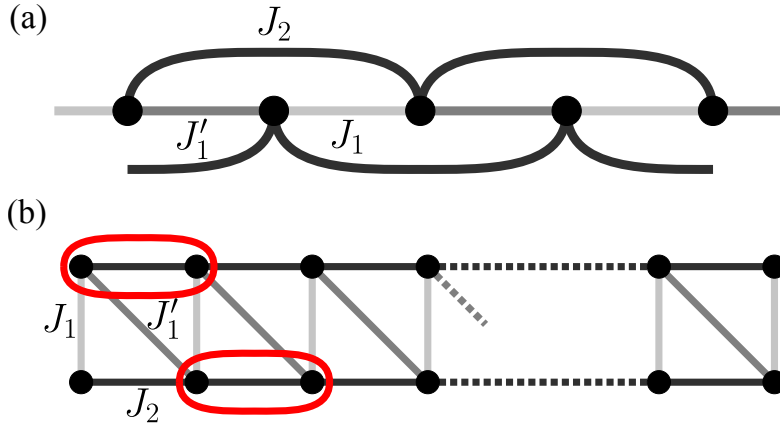


Figure 3.11: (a) Lattice structure of the  $J_1 - J'_1 - J_2$  model. (b) Topologically equivalent situation which allows to schematic picture of the valence-bond-solid gapped state. Red ellipses indicate spin-singlet pairs that form in the AKLT (Haldane) state.

This is similar to the ground state of the AKLT model in Eq. (3.6), but the symmetric operation between two spin- $\frac{1}{2}$ 's within the effective  $S = 1$  site, i.e.,  $\frac{1}{\sqrt{2}}(|\uparrow\rangle|\downarrow\rangle + |\downarrow\rangle|\uparrow\rangle)$ , is not explicitly included. Alternatively, two terms in Eq. (3.22) correspond to two-fold degenerate states. The Lieb-Schultz-Mattis theorem is thus satisfied. A schematic picture of either one is shown in Fig. 3.1(d), in which every site forms a singlet pair with the third neighbour site. In fact, setting  $J_1^{\text{edge}} = 0$  corresponds to an *explicit* replacement of  $S = 1$  spin at the each end by  $S = \frac{1}{2}$  spin in our effective  $S = 1$  chain [82]. It removes the degeneracy due to the edge spin state and enables us to calculate the spin gap with the DMRG method. The essential physics of our  $\mathcal{D}_3$ -VBS state can be explained by extracting a single *plaquette* including two effective  $S = 1$  sites, i.e., four  $S = \frac{1}{2}$  sites, in the same way that a combined spin-2 state is projected out in the AKLT model (see Sec. 3.2.1).

### 3.3 Dimerised $J_1 - J'_1 - J_2$ chain

As noted in Sec. 3.1, due to lattice dimerisation in the compounds  $\text{LiCuSbO}_4$  and  $\text{Rb}_2\text{Cu}_2\text{Mo}_3\text{O}_{12}$ , it is interesting to consider a model with dimerised NN interaction.

#### 3.3.1 Model and method

The spin Hamiltonian is given by eq. (3.2). The lattice is shown in Fig. 3.11(a). We use the notations of next-nearest-neighbour coupling ratio  $\alpha = J_2/|J_1|$  (frustration parameter) and nearest neighbour coupling ratio  $\beta = J'_1/J_1$  (dimerisation parameter) hereafter.

When the system is undimerised ( $\beta = 1$ ), we are dealing with the so-called  $J_1 - J_2$  model described in Sec. 3.2. Increasing  $\alpha$ , a gapped phase with incommensurate spin-spin correlations follows a FM phase. The transition occurs at  $\alpha = 1/4$ , both in the quantum as well as in the classical model [59, 60]. The incommensurate (“spiral”) correlations are short ranged in the quantum model [61, 83]. A vanishingly small gap was predicted by the field-theory analysis [65] and we have numerically proved its existence in Sec. 3.2.3.

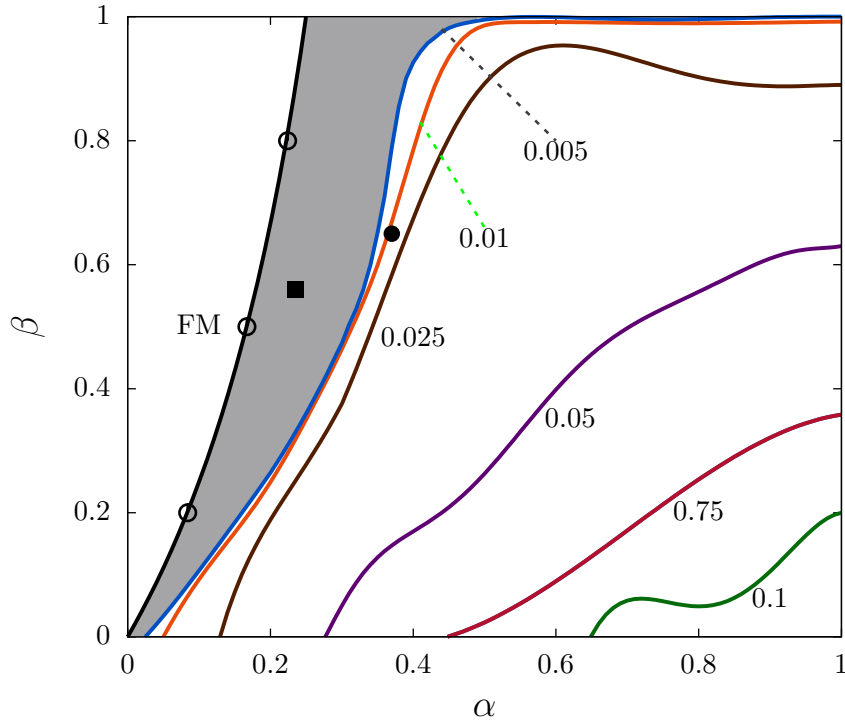


Figure 3.12: Phase diagram of the  $J_1$ - $J'_1$ - $J_2$  model in the  $\alpha$ - $\beta$  plane. Contour map for the spin gap  $\Delta/|J_1|$  is shown. The black line represents the boundary of the fully-polarised ferromagnetic and gapped incommensurate spiral states, obtained by spin-wave theory. The open circles mark the results from DMRG. The shaded area indicates the region with a vanishingly small gap ( $\Delta|J_1| < 10^{-3}$ ). Filled circle and square indicate the locations of  $\text{Rb}_2\text{Cu}_2\text{Mo}_3\text{O}_{12}$  and  $\text{LiCuSbO}_4$ , respectively.

In the limit of  $\beta = 0$ , the system (3.2) is equivalent to a spin ladder with AFM legs and FM rung couplings. Since this system can be effectively reduced to an  $S = 1$  AFM Heisenberg chain with regarding two  $S = 1/2$  spins on each rung as a  $S = 1$  spin [84, 85], the ground state is gapped as predicted by the Haldane conjecture [53]. Therefore, the ground state can be well described by a VBS picture, proposed in the AKLT model [74]. The schematic picture is shown in Figure 3.11(b).

We calculate the total spin with periodic boundary conditions, and spin gap, spin-spin correlation functions with open boundary conditions. In the DMRG calculation, we keep up to  $m = 6000$  density-matrix eigenstates in the renormalisation procedure and extrapolate the calculated quantities to the limit  $m \rightarrow \infty$  if necessary. Furthermore, several chains with lengths up to  $L = 800$  are studied to handle the finite-size effects. In this way, we can obtain quite accurate ground states within the error of  $\Delta E/L = 10^{-9} - 10^{-10}|J_1|$ .

### 3.3.2 Ferromagnetic critical point

In the limit of  $\beta = 0$  and  $\alpha = 0$ , the FM critical point no longer exists because the system is solely composed of isolated spin-triplet dimers. However, if  $\beta$  is finite, a FM order is expected for small  $\alpha$ . Let us then consider the  $\beta$ -dependence of the critical point. Since



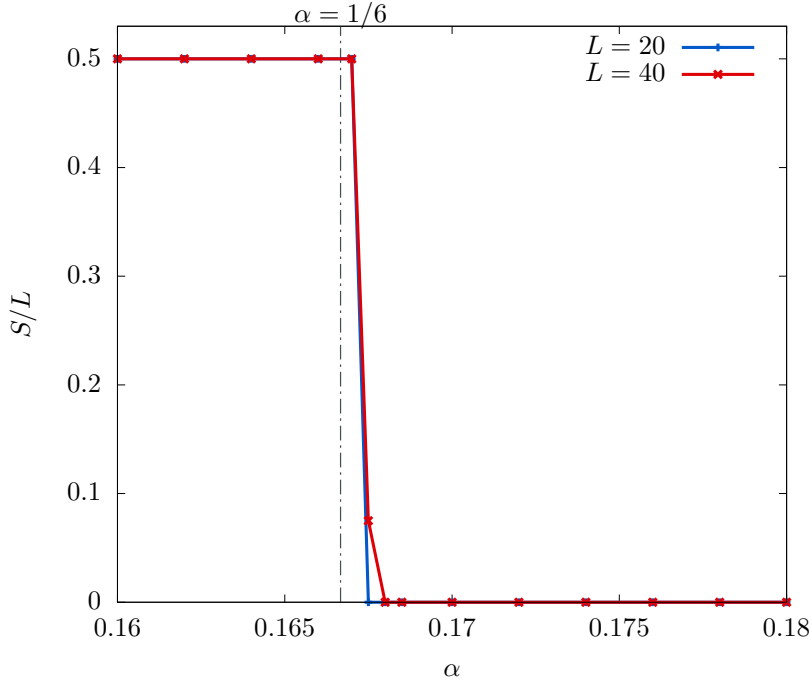


Figure 3.13: Normalised total spin as a function of  $\alpha$  at  $\beta = 0.5$ , calculated by DMRG with periodic boundary conditions.

the quantum fluctuations vanish at the FM critical point, the classical SWT may work perfectly for estimating the FM critical point. By the SWT the excitation energy for a FM ground state is given as

$$2\omega_q = -\sqrt{1 + \beta^2 + 2\beta \cos(2q)} + 2\alpha \cos(2q). \quad (3.25)$$

The system is in the FM ground state if  $\omega_q > 0$  for all  $q$ ; otherwise, it is in the spiral singlet state. Thus, the FM critical point is derived as

$$\alpha_{c,1} = \frac{\beta}{2(1 + \beta)}. \quad (3.26)$$

As shown in Fig. 3.12, the FM region is simply shrunk with decreasing  $\beta$ , and disappears in the limit of  $\beta = 0$  as a consequence of isolated FM dimers. It can be numerically confirmed by calculating the ground-state expectation value of the total-spin quantum number  $S$  of the whole system,  $\mathbf{S}^2$ , defined as  $\langle \mathbf{S}^2 \rangle = S(S + 1) = \sum_{ij} \langle \mathbf{S}_i \cdot \mathbf{S}_j \rangle$ . In Fig. 3.13, the normalized total spin at  $\beta = 0.5$  is plotted as a function of  $\alpha$ . We can find a direct jump from  $S = 0$  to  $S = L/2$  at  $\alpha \sim 0.17$ , indicating the absence of an intermediate (partially polarised) FM state. This critical value is in good agreement with that obtained by the SWT ( $\alpha_{c,1} = 1/6$ ). Similarly, for all  $\beta$  values, we confirm a direct transition between FM ( $S = L/2$ ) and singlet spiral ( $S = 0$ ) states as well as perfect agreement between SWT and DMRG critical points as compared in Fig. 3.12.

### 3.3.3 Haldane gapped state

The spin gapped state has been verified in the limit of  $\beta = 0$  [84, 85] and  $\beta = 1$  (Sec. 3.2.3). This can be interpreted as a realisation of the AKLT VBS state. However, it is a nontrivial

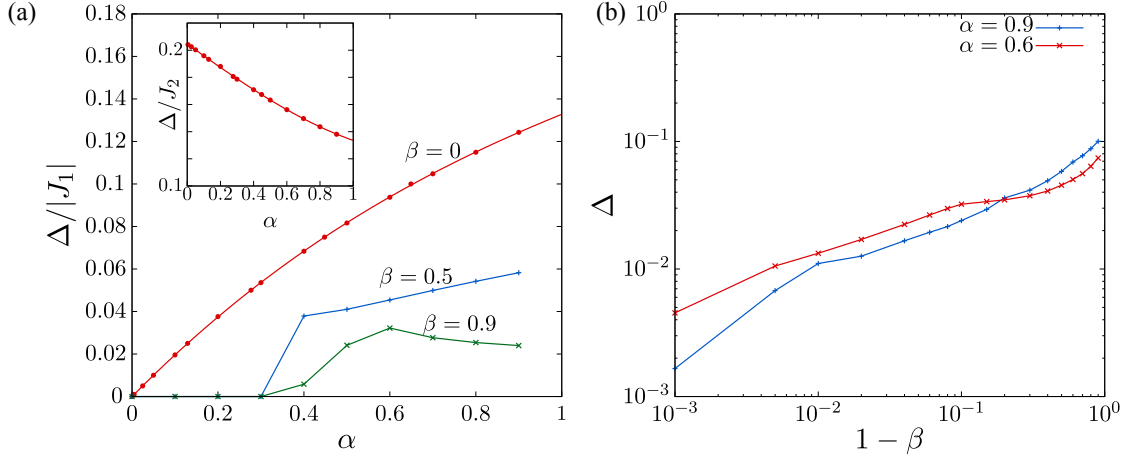


Figure 3.14: (a) Extrapolated spin gap  $\Delta/|J_1|$  as a function of  $\alpha$  for  $\beta = 0, 0.5,$  and  $0.9$ . Inset: similar plot of  $\Delta/J_2$  at  $\beta = 0$ . (b) Log-log plot of  $\Delta/|J_1|$  as a function of  $1 - \beta$  for  $\alpha = 0.6$  and  $0.9$ .

question what happens to the spin gap for finite  $0 < \beta < 1$ . The spin gap  $\Delta$  is evaluated as the energy difference between the lowest triplet state and the singlet ground state as in Eq. (3.14).

First, we focus on the case of  $\beta = 0$ , namely, a ladder consisting of two AFM leg chains and FM rungs. In Fig. 3.14(a) the extrapolated values of  $\Delta/|J_1|$  is plotted as a function of  $\alpha$ . The gap opens at  $\alpha = 0$  and increases monotonously with increasing  $\alpha$ , and saturates at a certain value scaled by  $|J_1|$ . This means that  $\Delta$  is finite for all  $\alpha$  at  $\beta = 0$ , which is consistent with the prediction by the bosonisation method [85] and the conformal field theory [86]. In the limit of  $\alpha = 0$  the system is exactly reduced to a  $S = 1$  AFM Heisenberg chain

$$H_{\text{eff}} = J_{\text{eff}} \sum_i \tilde{\mathbf{S}}_i \cdot \tilde{\mathbf{S}}_{i+1} - J_1 L/4, \quad (3.27)$$

where  $\tilde{\mathbf{S}}_i$  is a spin-1 operator as resultant spin  $\tilde{\mathbf{S}}_i = \mathbf{S}_{2i} + \mathbf{S}_{2i+1}$  and  $J_{\text{eff}} = J_2/2$ . In the inset of Fig. 3.14(a)  $\Delta$  is replotted in unit of  $\alpha$ . We obtain  $\Delta/J_2 = 0.2045$  in the limit  $\alpha = 0$ . The Haldane gap of the system (3.27) has been calculated as  $\Delta/J_{\text{eff}} = 0.410479$  [87]. Thus, we can confirm  $J_{\text{eff}} = J_2/2$  numerically for the mapping from Eq.(3.2) to Eq.(3.27) at the limit  $|J_1|/J_2 (= 1/\alpha) \rightarrow 0$  and  $\beta = 0$ .

Next, we look at the effect of  $\beta$  on the spin gap. Figure 3.14(b) shows a log-log plot of  $\Delta/|J_1|$  as a function of  $1 - \beta$  for  $\alpha = 0.6$  and  $0.9$ . The behaviours are nontrivial, but  $\Delta$  decays roughly as a power law with decreasing  $1 - \beta$ . As a result, the gap is vanishingly small near the uniform  $J_1$ - $J_2$  limit ( $\beta \sim 1$ ). As discussed in Sec. 3.2, this is due to the fact that we are not applying the correct boundary conditions on the  $J_1$  coupling at the edges while performing this study. Besides, it is interesting that  $\Delta$  for  $\alpha = 0.6$  is larger than that for  $\alpha = 0.9$  at larger  $\beta$  and opposite at smaller  $\beta$ . We know that the gapped state at  $\beta = 1$  is an AKLT-type VBS with valence bonds forming between third-neighbours (see Sec. 3.2.4). The crossing depicted in Fig. 3.14(b) suggests that for smaller  $\beta$  the gapped state is in the AKLT-like VBS state depicted in Fig. 3.11(b), with valence bonds forming on NNN ( $J_2$ -VBS), while near  $\beta = 1$  the state is described

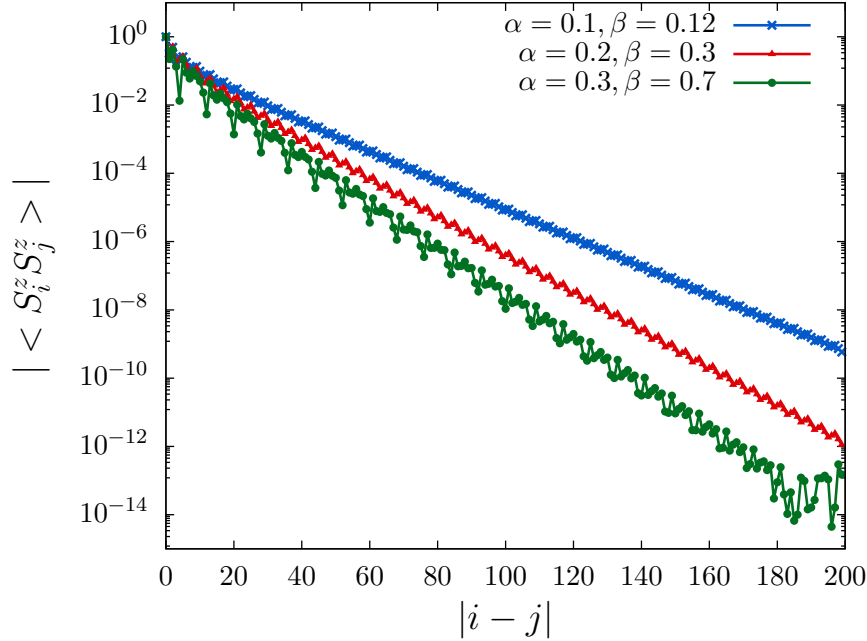


Figure 3.15: Equal-time spin-spin correlation function  $|\langle S_i^z S_j^z \rangle|$  as a function of distance  $|i-j|$  at  $\alpha = 0.1, \beta = 0.12$ ,  $\alpha = 0.2, \beta = 0.3$ , and  $\alpha = 0.3, \beta = 0.7$  for the  $L = 400$  cluster.

by a  $\mathcal{D}_3$ -VBS as explained in Sec. 3.2.6. A contour plot of the magnitude of  $\Delta$  is given in Fig. 3.12. We can see a rapid decay of  $\Delta$  with approaching the FM phase. However,  $\Delta$  is too small to figure out whether it remains finite, e.g.  $\Delta \lesssim 10^{-3}$ , in the vicinity of the FM critical boundary. Therefore, to verify the presence or absence of the gap, we checked the asymptotic behaviour of spin-spin correlation function  $|\langle S_i^z S_j^z \rangle|$ . In Fig. 3.15 the semi-log plot of  $|\langle S_i^z S_j^z \rangle|$  as a function of distance  $|i-j|$  is shown for some parameters near the the FM critical boundary. The distances  $|i-j|$  are taken about the midpoint of the systems to exclude the Friedel oscillations from the system edges, i.e.  $(i+j)/2$  locates around the midpoint of the systems. All of them exhibit exponential decay of  $|\langle S_i^z S_j^z \rangle|$  with distance, which clearly indicates the presence of a finite spin-gap. The curves are well-fitted with the expression  $|\langle S_i^z S_j^z \rangle| \propto \cos[Q(i-j)]|i-j|^{-\frac{1}{2}} e^{-\frac{|i-j|}{\xi}}$  for long distances [88, 89]; the correlation lengths  $\xi$  are estimated as  $\xi = 11.6$  ( $\alpha = 0.1, \beta = 0.12$ ),  $\xi = 8.6$  ( $\alpha = 0.2, \beta = 0.3$ ), and  $\xi = 7.3$  ( $\alpha = 0.3, \beta = 0.7$ ). In the AFM  $J_1 - J_2$  model [88], a region with  $\xi \approx 10$  still has a spin gap of order of  $10^{-1} J_1$ . This may imply the spin velocity of our system is more than two digits smaller than that of the AFM  $J_1 - J_2$  model since  $\Delta = v_s / \xi$  where  $v_s$  is the spin velocity.

Therefore, to consider the connection to the gapped state with tiny gap  $\Delta \lesssim 10^{-40} J_2$  at  $\alpha > 3.3$  predicted by field theory [65], we estimated the correlation length as shown in figure 3.16, where the absolute values of spin-spin correlation functions  $|\langle S_i^z S_j^z \rangle|$  for  $\alpha = 0.35, 0.5$ , and  $0.9$  are plotted as a function of distance  $|i-j|$ . We can clearly see the exponential decays for all  $\alpha$  values. By performing the fitting of  $|\langle S_i^z S_j^z \rangle|$  with a function  $\langle S_0^z S_r^z \rangle = A \exp(-r/\xi)$ , where  $\xi$  is the correlation length, we obtained  $\xi = 116$  for  $\alpha = 0.35$ ,  $\xi = 52$  for  $\alpha = 0.5$ , and  $\xi = 192$  for  $\alpha = 0.9$ . We found that the inverse correlation length is well fitted by  $1/\xi = 0.085 \exp(-\pi\alpha)$  for large  $\alpha$ . Since  $\Delta = v_s / \xi$ , it

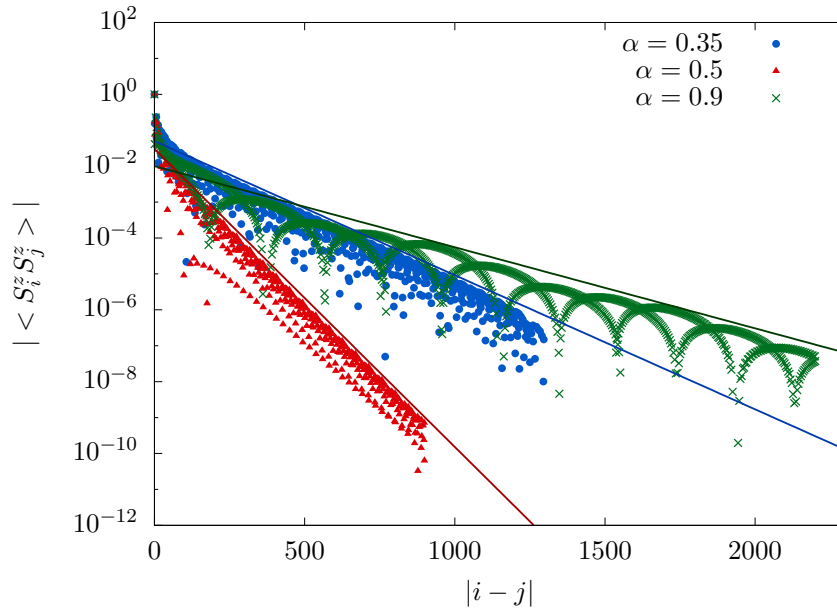


Figure 3.16: Spin-spin correlation functions  $|\langle S_i^z S_j^z \rangle|$  as a function of distance  $|i - j|$  for several  $\alpha$  values in the uniform  $J_1$ - $J_2$  model ( $\beta = 1$ ). The solid lines exhibit fittings with a function  $\langle S_0^z S_r^z \rangle = A \exp(-r/\xi)$  where  $\xi$  is the correlation length.

may be feasible to speculate that the gap has a maximum around  $\alpha = 0.5 - 0.6$ , decreases with increasing  $\alpha$ , and smoothly connects to the tiny gap region.

### 3.4 Discussion

We considered a frustrated  $J_1$ - $J_2$  spin chain without/with dimerisation of nearest-neighbour FM coupling and determined its phase diagram in both cases.

For the undimerised model, we find a second order phase transition at  $\alpha = \frac{1}{4}$  from a FM state to a third-neighbour VBS state with the AKLT-like topological hidden order based on the results of string order parameter, dimerisation order parameters, dimer-dimer correlation function, and entanglement entropy. This provides a simple realisation of coexistence of spontaneous symmetry breaking and topological order, or rather, topological order caused by spontaneous symmetry breaking. It may be helpful to consider this transition in two steps: (i) *The system exhibits a spontaneous nearest-neighbour FM dimerisation, i.e., breaking of translational symmetry, as a consequence of the quantum fluctuations typical of magnetic frustration – order by disorder.* (ii) *By regarding the ferromagnetically dimerised spin- $\frac{1}{2}$  pair as a spin-1 site, the system is effectively mapped onto a  $S = 1$  Heisenberg chain and topological order as in the Haldane state is possible. The coexistence of symmetry breaking and topological order is thus allowed. Then, we proposed the third-neighbour valence bond formation as the origin of the finite spin gap since the FM dimerisation alone does not lead to a finite gap. The third-neighbour valence bond formation is consistent with the Haldane state with valence bond formation between nearest-neighbour  $S = 1$  sites, as the two third-neighbour spins in the  $J_1$ - $J_2$  chain can be seen as nearest-neighbour spin-1 sites on the effective  $S = 1$  chain.*

The emergence of third-neighbour VBS formation was also confirmed by the observation of adiabatic connection of the ground state to an enforced third-neighbour dimerised state. Originated from the VBS state, the spin gap opens at  $\alpha = \frac{1}{4}$  and reaches its maximum  $\Delta \simeq 0.007|J_1|$ , which is about two orders of magnitude smaller than that for the AFM  $J_1$ - $J_2$  chain, at  $\alpha \simeq 0.6$ . Since the correlation length of spin-spin correlation seems to diverge at  $\alpha = \infty$ , a tiny but finite spin gap may be present up to  $\alpha = \infty$ .

For the dimerised chain, the FM critical point is analytically determined to be  $\alpha_c = (\beta/2)/(1 + \beta)$  by applying the linear spin-wave theory, which was confirmed by the numerical calculation of the total spin. The transition between the fully polarised FM and the singlet spiral states is of the first order for  $\beta < 1$  and no partially polarised FM state exists. The spin-gap in the vicinity of the FM boundary was confirmed to be finite by the exponential decay of the spin-spin correlation functions but it is vanishingly small. Near  $\beta = 0$  the spin-gap increases with increasing  $\alpha$ ; whereas, near  $\beta = 1$  it has a maximum value around the strongest frustration region  $\alpha = 0.6$ , as shown in Sec. 3.2.3. Therefore, the gap opening in the entire incommensurate singlet phase may be interpreted as a crossover between two different AKLT-type VBS states: Near  $\beta = 0$  the valence bonds form along NNN on the  $J_2$  bonds ( $J_2$ -VBS), while near  $\beta = 1$  they form between third-neighbours along the symmetry breaking direction ( $\mathcal{D}_3$ -VBS). Moreover, the spin gap computed for  $\beta > 0.9$  is probably underestimated as we did not use special OBC with zero coupling at the edges as done for the undimerised  $J_1$ - $J_2$  model.

A typical value for  $J_1$  in cuprates is  $J_1 = -200\text{K}$ , which leads to a gap closing at external magnetic field  $\simeq 1\text{ T}$  for the undimerised chain. In real materials, the exchange couplings have been estimated to be  $J_1 = -6.95\text{ meV}$ ,  $J_2 = 5.20\text{ meV}$  ( $\alpha = 0.75$ ) for  $\text{LiCuVO}_4$  [90];  $J_1 = -6.84\text{ meV}$ ,  $J_2 = 2.46\text{ meV}$  ( $\alpha = 0.36$ ) for  $\text{PbCuSO}_4(\text{OH})_2$  [91]. If experimental measurements are performed at very low temperature, a spin excitation gap with magnitude  $\Delta = 0.035\text{ meV}$  and  $\Delta = 0.013\text{ meV}$  could be observed, respectively.

Concerning materials with explicit NN dimerisation, density-functional calculations predict  $\alpha = 0.235$  and  $\beta = 0.56$  for  $\text{LiCuSbO}_4$  with  $J_1 \approx -160\text{ K}$ ,  $J'_1 \approx -90\text{ K}$ , and  $J_2 \approx 37.6\text{ K}$  [43]. The system is in the gapped spiral state, but very close to the FM phase where the spin-gap is vanishingly small. Thus, the spin gap may be too small to be detected experimentally. For the compound  $\text{Rb}_2\text{Cu}_2\text{Mo}_3\text{O}_{12}$ , previously estimated parameters are  $J_1 = -138\text{ K}$  and  $J_2 = 51\text{ K}$  ( $\alpha = 0.37$ ). Then, a substantial dimerisation ( $\beta = 0.65$ ) of  $J_1$  and  $J'_1$  is necessary to reproduce the experimentally observed gap  $E_g \sim 1.6\text{ K}$ , namely,  $J_1 = -138\text{ K}$  and  $J'_1 = 90\text{ K}$ . Furthermore, if it is more appropriate to consider the value  $-138\text{ K}$  as an averaged FM coupling  $(J_1 + J'_1)/2$ , then an even larger dimerisation would be needed. In practice, the actual  $J_1$  should be somewhat smaller or  $J_2$  should be larger. A detailed analysis of the experimental data that explicitly takes into account the dimerisation can clarify this point.



# 4 Kitaev materials

While in chapter 2 we have investigated a prototype of geometric frustration in 1D, we now turn to the other face of magnetic frustration, namely exchange frustration. As stated in the Introduction (Chapter 1), exchange frustration arises when the different types of interactions on different bonds cannot be satisfied simultaneously. Nowadays, the most famous example of this is the Kitaev model on a honeycomb lattice. This peculiar compass model allows for an analytical solutions and supports exotic Majorana quasiparticles. A summary of the properties of this model is given in Sec. 4.1.

Though this model has such intriguing properties, it is crucial to determine the class of materials that can host such Kitaev physics. This is reviewed in Sec. 4.2, together with the introduction of the Kitaev-Heisenberg (KH) model.

## 4.1 The Kitaev model

In 2006, Alexei Kitaev published the solution for a compass model on a honeycomb lattice [92]. This system exhibits exchange frustration and has an exact solution. This solution turns out to be a  $\mathbb{Z}_2$  spin liquid and the phase diagram exhibits a gapless and a gapped phase. By applying a magnetic field, a gap is induced in the gapless phase and the system exhibits non-Abelian excitations.

The system is described by the following Hamiltonian on the honeycomb lattice:

$$\mathcal{H}_{\text{Kitaev}} = -K^x \sum_{x\text{-bonds}} S_i^x S_j^x - K^y \sum_{y\text{-bonds}} S_i^y S_j^y - K^z \sum_{z\text{-bonds}} S_i^z S_j^z. \quad (4.1)$$

The different sums run on different kind of bonds, labeled  $x$ ,  $y$ , and  $z$  bonds depending on the spin component considered for the Ising-like interaction. On the honeycomb lattice, there are three bonds emanating from every lattice site, so that each site has every kind of bond interaction. Moreover, two adjacent bonds do not carry the same flavour of bond interaction. The lattice is represented in Fig. 4.1(a). Note that the lattice is bipartite and the unit cell is composed of two lattice sites.

Kitaev's solution uses the Majorana representation for spins, where one spin component in a multi-spin system can be represented through two Majorana operators, where there are four different flavours of Majoranas. He also introduces the plaquette operator

$$\mathcal{O}_{\text{plaquette}} = 2^6 S_1^x S_2^y S_3^z S_4^x S_5^y S_6^z, \quad (4.2)$$

where the spin component at site  $i$  is defined by the incoming bond not included in the considered plaquette [see Fig. 4.1(a)] and we have included a normalisation factor  $2^6$  such that the operator squares to 1. This operator commutes with the Hamiltonian (4.1). This is relatively easy to see by considering one bond, for example the 1-2 bond in Fig. 4.1(a). On this bond, the relevant interaction is  $K^z S_1^z S_2^z$ , so that we need to consider the commutator  $[S_1^z S_2^z, \mathcal{O}_{\text{plaquette}}]$ . This effectively reduces to  $[S_1^z S_2^z, S_1^x S_2^y]$ , as spin operators

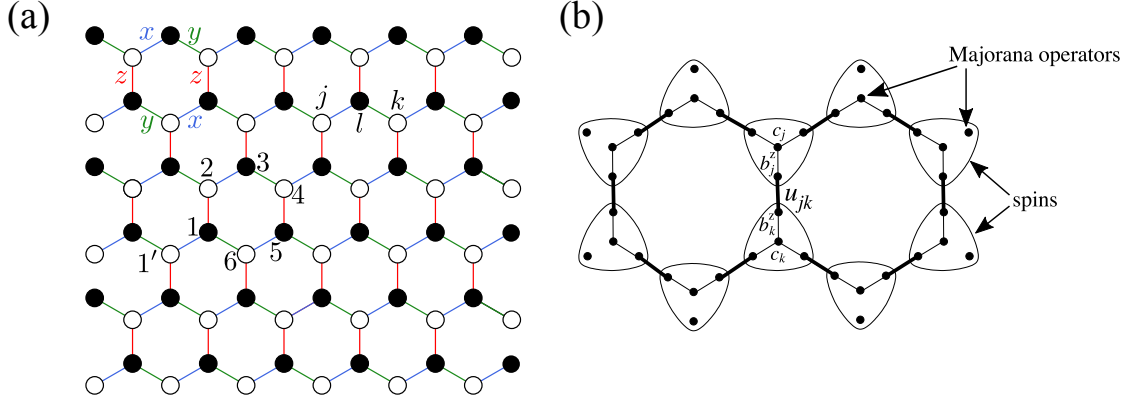


Figure 4.1: (a) The Kitaev model on the honeycomb lattice. Black and white sites show the bipartition on the lattice.  $x$ ,  $y$  and  $z$  label the bonds.  $l$ ,  $j$  and  $k$  label the sites considered for the field induced mass term in Eq. (4.40). The numbering shows one plaquette as in Eq. (4.2). (b) The Majorana representation as in Eq. (4.10), adapted from Ref. [92]

at different sites commute. Then, we have

$$[S_1^z S_2^z, S_1^x S_2^y] = S_1^z S_2^z S_1^x S_2^y - S_1^x S_2^y S_1^z S_2^z = \frac{i}{2} S_1^y \left(-\frac{i}{2} S_2^x\right) - \left(-\frac{i}{2} S_1^y\right) \frac{i}{2} S_2^x = 0, \quad (4.3)$$

where we have used the Pauli matrices' property  $\sigma_i \sigma_j = \delta_{ij} + i \epsilon_{ijk} \sigma_k$  and  $S^\gamma = \frac{1}{2} \sigma^\gamma$ . We now also consider an incoming bond, for example 1-1' in Fig. 4.1(a). In this case, the interaction reads  $K_x S_1^x S_{1'}^x$ . This directly commutes with all spin operators in the plaquette except for  $S_1^x$ :

$$[S_1^x S_{1'}^x, S_1^x] = [S_1^x, S_{1'}^x] S_1^x + S_{1'}^x [S_1^x, S_{1'}^x] = 0. \quad (4.4)$$

This can be done in a similar way for all bonds. Furthermore, plaquette operators on different plaquettes commute with each other. This can be proven in a similar way as done for the commutation with the Hamiltonian.

As plaquette operators commute with the Hamiltonian, they are conserved quantities of the system. This means we have at least  $2^N$  conserved quantities, with  $N$  being the number of unit cells in the system, as this is the number of plaquettes in a honeycomb lattice. Moreover,  $\langle \mathcal{O}_{\text{plaquette}} \rangle = 1$ , so that the eigenvalues are  $O_{\text{plaquette}} = \pm 1$ . We call the eigenvalue on plaquette  $j$  the flux of the plaquette, also referred to as static flux, gauge flux or  $\mathbb{Z}_2$  flux. We can then divide the Hilbert space into  $2^N$  sectors with a certain plaquette configuration, e.g. the sector where all  $O_{\text{plaquette}} = 1$ . Each sector has  $2^N$  degrees of freedom left.

As previously stated, Kitaev's approach builds on the representation of spin operators in terms of Majorana ones. We here recall the properties of this kind of operators. First, the defining property of Majorana particles is that they are their own antiparticle, so that  $a_i = a_i^\dagger$ , making them Hermitian. They satisfy the following relations:

$$a_i^2 = 1 \quad [a_i, a_j]_+ = \delta_{ij}, \quad (4.5)$$



where  $[\cdot, \cdot]_+$  is the anticommutator, so that Majorana operators obey the fermionic commutation relation. As any operator can be represented in terms of Hermitian operators, the fermionic creation and annihilation operators  $c_i, c_i^\dagger$  can be rewritten as

$$c_i = a_{2j-1} + ia_{2j}. \quad (4.6)$$

It is possible to write the spin- $\frac{1}{2}$  operators in terms of four different (real) flavours of Majorana modes  $c, b_x, b_y, b_z$  in the following way:

$$2S^x = icb_x \quad (4.7)$$

$$2S^y = icb_y \quad (4.8)$$

$$2S^z = icb_z, \quad (4.9)$$

with a constraint  $cb_x b_y b_z = 1$  for the physical system. This representation preserves the spin commutation relations  $[S_i^\alpha, S_j^\beta]_+ = \frac{1}{2}\delta_{\alpha\beta}$  and  $[S_i^\alpha, S_j^\beta] = i\epsilon_{\alpha\beta\gamma}S_j^\gamma$ .

Within this new representation, the original Hamiltonian (4.1) can be mapped to

$$\mathcal{H}_{\hat{u}} = i \sum_{\langle i,j \rangle} K_{ij}^\alpha \hat{u}_{ij} c_i c_j, \quad (4.10)$$

with  $\hat{u}_{ij} = ib_i^{\alpha_{ij}} b_j^{\alpha_{jk}}$ , where  $\alpha_{ij}$  labels the direction of the bond, and  $\hat{u}_{ij} = -\hat{u}_{ji}$ . The operators  $\hat{u}_{ij}$  commute with the Hamiltonian and have eigenvalues  $u_{ij} = \pm 1$ . This Hamiltonian is illustrated in Fig. 4.1(b).

It is possible to show that all possible choices of  $\{u_{ij}\}$  for a given plaquette configuration (flux sector) are equivalent. The plaquette operator in this notation is written as  $\mathcal{O}_{\text{plaquette}} = u_{21}u_{23}u_{43}u_{45}u_{65}u_{61}$ . For instance, if all plaquettes have eigenvalue  $\langle \mathcal{O}_i \rangle = 1$ , then we can take all  $u_{ij} = 1$ , but this is not the only possible admissible configuration. For example, flipping all bonds emanating from the same site does not change the flux sector. All configuration of  $u_{ij}$  corresponding to the same plaquette configuration are gauge equivalent and only correspond to choosing a different sign for the  $c$  Majoranas (gauge transformation). The gauge redundancy comes from the transformation into Majorana operators, which has increased the size of the Hilbert space, leading to the emergence of a  $\mathbb{Z}_2$  field. Physically, this means our spins have fractionalised into delocalised Majorana modes and static gauge fluxes. The fluxes are long range ordered, but Majorana-Majorana correlations decay algebraically: we conclude there is no magnetic order and we are in the presence of a spin liquid.

We now present a different approach to the problem and use it to define the phase diagram of the Kitaev model on a honeycomb lattice. Namely, we will be using a Jordan-Wigner transformation to fermionize the spins, following Chen and Nussinov [93]. The way this one-dimensional transformation works on the two-dimensional honeycomb lattice is made more vivid by considering a brickwall lattice as in Fig. 4.2(a). The latter is topologically equivalent to the honeycomb one. The Jordan-Wigner transformation was originally introduced for 1D systems. Nonetheless, by finding a suitable path, it is possible to extend it to two-dimensional lattices. For the brickwall lattice, the path chosen for the transformation is shown in Fig. 4.2(b). We use the notation w/b (white/black)

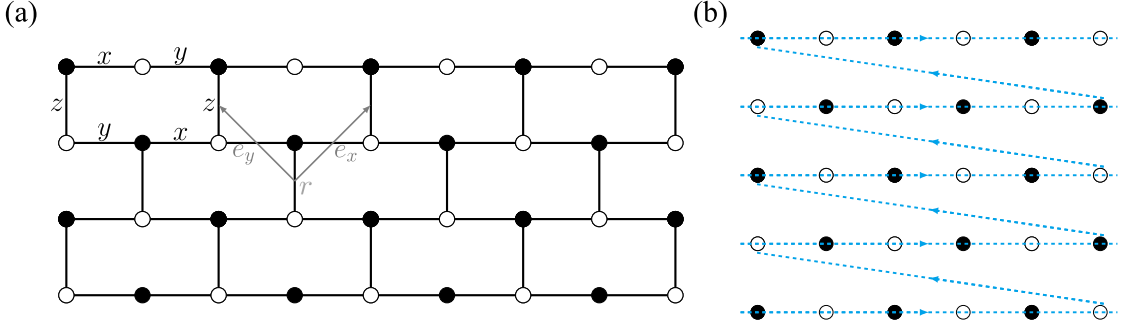


Figure 4.2: (a) Brickwall lattice with  $x$ ,  $y$  and  $z$  bonds on one plaquette and lattice vectors  $e_x$  and  $e_y$  and label  $r$  on one  $z$  bond. (b) Schematic of the Jordan-Wigner transformation on the brickwall lattice.

to denote the two sublattices as illustrated in Fig. 4.2(a) and we introduce Cartesian coordinates  $(\alpha, \beta)$  for every site  $i$ . Then, we define the transformation:

$$\sigma_{\alpha\beta}^+ = 2 \left[ \prod_{\beta' < \beta} \prod_{\alpha'} \sigma_{\alpha'\beta'}^z \right] \left[ \prod_{\alpha' < \alpha} \sigma_{\alpha'\beta}^z \right] c_{\alpha\beta}^\dagger \quad (4.11)$$

$$\sigma^z = 2c_{\alpha\beta}^\dagger c_{\alpha\beta} - 1, \quad (4.12)$$

where  $c_{\alpha\beta}^\dagger$  is the fermion creation operator associated with the spin raising operator and the factor of 2 comes from noticing that  $\sigma_{\alpha\beta}^+ = (\sigma_{\alpha\beta}^x + i\sigma_{\alpha\beta}^y)$  is twice the spin raising operator.

The Kitaev Hamiltonian (4.1) is now rewritten as

$$\begin{aligned} \mathcal{H}_{\text{Kitaev}} = & K_x \sum_{x\text{-bonds}} (c^\dagger - c)_w (c^\dagger + c)_b - K_y \sum_{y\text{-bonds}} (c^\dagger + c)_w (c^\dagger - c)_w \\ & - K_z \sum_{z\text{-bonds}} (2c^\dagger c - 1)_w (2c^\dagger c - 1)_b. \end{aligned} \quad (4.13)$$

For each bond, we drop the Cartesian-coordinate notation and refer to black and white sites as shown in Fig. 4.2(a).

It is generally possible to express a fermion operator in term of Majorana operators. Hence, we rewrite fermionic operators on white and black sites as:

$$c_w^\dagger = \frac{B_w - iA_w}{2} \quad (4.14)$$

$$c_b^\dagger = \frac{A_b - iB_b}{2}. \quad (4.15)$$

In the Majorana representation, the Hamiltonian (4.1) becomes

$$\mathcal{H}_{\text{Kitaev}} = -i \left[ K_x \sum_{x\text{-bonds}} A_w A_b - K_y \sum_{y\text{-bonds}} A_b A_w \right] - K_z \sum_{z\text{-bonds}} (BA)_b (BA)_w. \quad (4.16)$$

It is easy to see that the operator  $B_b B_w$  along the  $z$ -bonds is a conserved quantity. We define an operator

$$\alpha_r = iB_b B_w, \quad (4.17)$$

where  $r$  labels the middle of the bond between a black and a white site (Fig. 4.2(a) shows  $r$  on a  $z$  bond) and  $B_b$  and  $B_w$  are defined by Eqs. (4.14) and (4.15). Finally, the Hamiltonian takes the form:

$$\mathcal{H}_{\text{Kitaev}} = -i \left[ K_x \sum_{x\text{-bonds}} A_w A_b - K_y \sum_{y\text{-bonds}} A_b A_w \right] - iK_z \sum_{z\text{-bonds}} \alpha_r A_b A_w. \quad (4.18)$$

Notice that  $\alpha_r$  are  $\mathbb{Z}_2$  static local gauge fields and, since there are no direct connections between  $z$ -bonds, all  $\alpha_r$  operators are good quantum numbers, meaning they commute with each other as well as with the Hamiltonian.

The Hamiltonian (4.18) is a free Majorana model with static  $\mathbb{Z}_2$  gauge fields. A similar expression was derived in the original work of Kitaev [92]. In that case, however, four Majoranas were introduced for each spin, requiring to make use of a projection to get rid of the redundant degrees of freedom.

As said, the plaquette operator (4.2) is a conserved quantity. This quantity is related to the  $\alpha_r$  operators. In fact:

$$\sigma_{1w}^y \sigma_{2b}^z \sigma_{3w}^x = iB_{1w} B_{3b} \quad (4.19)$$

$$\sigma_{6b}^x \sigma_{5w}^z \sigma_{4b}^y = iB_{4b} B_{6w}. \quad (4.20)$$

Therefore

$$\mathcal{O}_{\text{plaquette}} = \alpha_{34} \alpha_{16}. \quad (4.21)$$

Note that inverting all  $\alpha_r$  on one horizontal row does not affect the system. This is explicitly shown in Ref. [93]. Here, the authors also show how the degree of freedom given by the possibility of choosing the direction of one  $\alpha$  on each row is related to the string-like quantity in the original spin model  $P_j = \prod_i \sigma_i j^z$ . Furthermore, the authors point out that taking the gauge where one  $\alpha$  is fixed to +1 on each row makes the set  $\{\mathcal{O}_{\text{plaquette}}^h\}$  equivalent to the set  $\{\alpha_r\}$ .

In order to determine the energy spectrum of the model, we recombine the Majoranas into fermion operators on  $z$  bonds as

$$d = \frac{A_w + iA_b}{2} \quad d^\dagger = \frac{A_w - iA_b}{2}. \quad (4.22)$$

We define the unit vector  $\hat{e}_y$  as the vector connecting two  $z$  bonds and crossing a  $y$  bond. In the same manner, we can define a unit vector  $\hat{e}_x$ . These vectors define the square lattice where the fermion operators (4.22) act. On this lattice and with the operators defined in (4.22), the Hamiltonian takes the form

$$\mathcal{H}_{\text{Kitaev}} = K_x \sum_r (d_r^\dagger + d_r)(d_{r+\hat{e}_x}^\dagger - d_{r+\hat{e}_x}) + K_y \sum_r (d_r^\dagger + d_r)(d_{r+\hat{e}_y}^\dagger + d_{r+\hat{e}_y}) + K_z \sum_r \alpha_r (2d_r^\dagger d_r - 1) \quad (4.23)$$

and  $\alpha_r$  now plays the role of a site-dependent chemical potential. By definition

$$[\alpha_r, d_r^\dagger] = [\alpha_r, d_r] = 0. \quad (4.24)$$

A theorem by Lieb assures us that, for large enough systems, the ground state is in the vortex free sector  $O_{\text{plaquette}} = 1$  for all plaquettes. In terms of the fermionic model (4.23), this means all  $\alpha_r = 1$ . As previously stated, reversing a plaquette from 1 to  $-1$  corresponds to reversing all  $\alpha_r$  on a given horizontal string.

To get the ground state, we perform a Fourier transformation

$$d_r^\dagger = \frac{1}{\sqrt{N}} \sum_q e^{iqr} d_q^\dagger. \quad (4.25)$$

This leads to

$$\mathcal{H}_{\text{FT}} = \sum_q \left[ \epsilon_q d_q^\dagger d_q + i \frac{\Delta_q}{2} (d_q^\dagger d_{-q}^\dagger + h.c.) \right], \quad (4.26)$$

with

$$\begin{aligned} \epsilon_q &= 2K_z - 2K_x \cos q_x - 2K_y \cos q_y \\ \Delta_q &= 2K_x \sin q_x + 2K_y \sin q_y. \end{aligned} \quad (4.27)$$

The Hamiltonian (4.23) is that of a  $p$ -wave superconductor, as the second term shows spinless superconducting pairing. By performing a Bogoliubov transformation, we can write the Hamiltonian as

$$\mathcal{H}_{\text{FT}} = \begin{pmatrix} d_q^\dagger & d_{-q} \end{pmatrix} \mathcal{H}_{\text{BdG}} \begin{pmatrix} d_q \\ d_{-q}^\dagger \end{pmatrix} \quad \mathcal{H}_{\text{BdG}} = \epsilon_q \sigma_z + \Delta_q \sigma_y, \quad (4.28)$$

with  $\sigma_\gamma$  being the Pauli matrices. This is easily diagonalised and gives us the spectrum:

$$E_q = \sqrt{\epsilon_q^2 + \Delta_q^2}. \quad (4.29)$$

By analysing Eq. (4.27) and Eq. (4.29), we can determine when the energy spectrum is gapped. To do so, we study the solution to the condition  $E_q = 0$ . This is equal to requiring  $\epsilon_q^2 + \Delta_q^2 = 0$ . Imposing that the sum of two squares of real quantities vanishes translates into a system of two equations  $\epsilon_q = 0$  and  $\Delta_q = 0$ :

$$\begin{cases} 2K_z - 2K_x \cos q_x - 2K_y \cos q_y = 0 \\ 2K_x \sin q_x + 2K_y \sin q_y = 0. \end{cases} \quad (4.30)$$

The first equation in (4.30) gives the condition

$$\cos q_x = \frac{K_z - K_y \cos q_y}{K_x}, \quad K_x \neq 0. \quad (4.31)$$

Remembering the first trigonometric fundamental relation  $\sin^2 \alpha + \cos^2 \alpha = 1$  and substituting in the second equation of the system (4.30), we get:

$$\pm \sqrt{K_x^2 - (K_z - K_y \cos q_y)^2} = -K_y \sin q_y. \quad (4.32)$$

Thanks to the  $\pm$  sign on the left hand side of Eq. (4.32), we do not need to impose any condition on  $K_y \sin q_y$  and we can square both sides in Eq. (4.32). Rearranging the terms, we get:

$$\cos q_y = \frac{K_y^2 + K_z^2 - K_x^2}{2K_z K_y}. \quad (4.33)$$

Substituting back into (4.31), we finally arrive at the values for  $q_x$  and  $q_y$ :

$$q_x = \pm \arccos \left[ \frac{K_x^2 + K_z^2 - K_y^2}{2K_x K_z} \right] \quad q_y = \pm \arccos \left[ \frac{K_y^2 + K_z^2 - K_x^2}{2K_y K_z} \right]. \quad (4.34)$$

The domain of the arccos function is  $[-1, 1]$ , so that, for this solution to be admissible, the following conditions have to be satisfied simultaneously

$$-2|K_x||K_z| < K_x^2 + K_z^2 - K_y^2 < 2|K_x||K_z| \quad (4.35)$$

$$-2|K_y||K_z| < K_y^2 + K_z^2 - K_x^2 < 2|K_y||K_z| \quad (4.36)$$

Solving these inequalities provides the conditions for gapless excitations

$$|K_x| < |K_y| + |K_z| \quad (4.37)$$

$$|K_y| < |K_z| + |K_x| \quad (4.38)$$

$$|K_z| < |K_x| + |K_y| \quad (4.39)$$

These are the same as the one obtained in the original work by Kitaev [92]. The phase diagram as a function of the  $K_\gamma$  ( $\gamma = x, y, z$ ) couplings is shown in Fig. 4.3. By mapping the fermion operators back to the original spin operators, it is possible to write down the real space spin state of the Kitaev model. This is found to be a gapless  $\mathbb{Z}_2$  spin liquid, also known as Kitaev spin liquid. In this state, spin-spin correlations are present only between first neighbours. More generally, for gapless spin liquids, spin-spin correlations decay algebraically. Note that, opposite to spin solids, spin liquids do not spontaneously break any symmetries. Spin liquids show no long range order even at zero temperature: in this case, quantum fluctuations prevent the formation of an ordered state, similarly to what thermal fluctuations do in normal liquids.

We will not continue further with analysing the gapped phase in detail, as we will focus only on the isotropic case  $K_x = K_y = K_z = K$  in the following. Let us just briefly state that the gapped state has Abelian anyonic excitations, i.e., the Majoranas obey

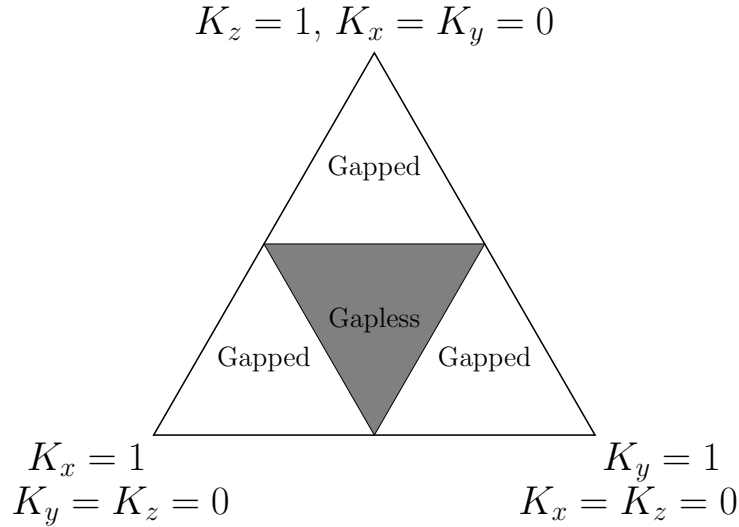


Figure 4.3: Phase diagram of the Kitaev model (see Ref. [92])

anyonic statistics, so that when two are interchanged in a process where each particle makes a counter-clockwise revolution around the other, the two-particle wavefunction gains a phase  $\theta$ :  $|\psi_1\psi_2\rangle = e^{i\theta} |\psi_2\psi_1\rangle$ . These excitations are Abelian [92], meaning that when this process is reversed, each particle makes a clockwise revolution around the other, the wavefunction gains a term  $e^{-i\theta}$ . Let us also note that  $\mathcal{H}_{\text{BdG}}$  does not possess a mass term able to generate a topologically non-trivial gapped superconducting state. Moreover, a gap is induced in the gapless state in the presence of an isotropic magnetic field and this new phase exhibits exotic non-Abelian anyonic excitations. In this case, the phase gained due to moving a particle around a loop is trajectory dependent, so that interchanging two particles twice might not take us back to the starting wavefunction. For small enough fields  $\mathbf{h} = (h_x, h_y, h_z)$ , perturbation theory gives us a mass term:

$$\mathcal{H}_{\text{mass}} \sim -\frac{8h_x h_y h_z}{K^2} \sum_{j,k,l} S_j^x S_k^y S_l^z, \quad (4.40)$$

where  $j$  and  $k$  define the  $\alpha$  bond and  $k$  and  $l$  define the  $\beta$  bond with  $\alpha \neq \beta$  (see Fig. 4.1(a)) and we have considered the isotropic case  $K_x = K_y = K_z = K$ . Note that this interaction includes NNN terms. The Majorana mass gap in this state is then proportional to the cube of the field itself  $\Delta \sim \frac{4h_x h_y h_z}{K^2}$ . This term gaps out the Dirac cones at  $(0, 0)$  and  $(\pi, \pi)$  [92].

## 4.2 Kitaev interaction in real materials

The model described in Sec. 4.1 hosts topological excitations and intriguing properties. But can it be translated into a real physical system? The answer to this question came a couple of years after the model was introduced, thanks to G. Jackeli and G. Khaliullin [95].

In this work, they showed how spin-orbit enhanced Mott insulators can support Kitaev-like interactions. We immediately notice that one of the key ingredients for the

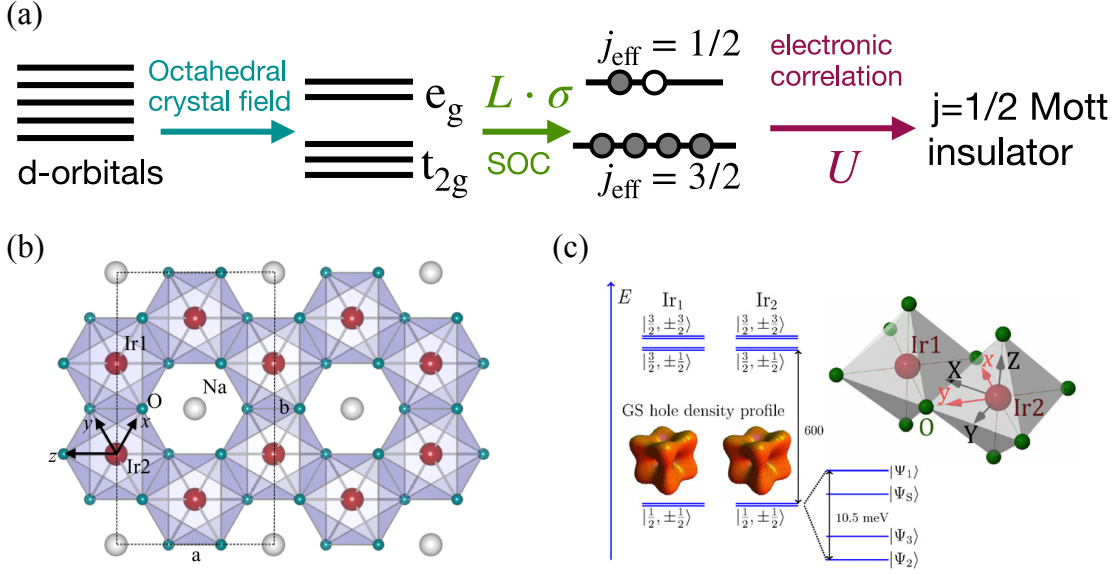


Figure 4.4: (a) Schematic for the formation of a  $j_{\text{eff}} = \frac{1}{2}$  Mott insulator in  $d^5$  materials. (b) Crystal structure of  $\text{Na}_2\text{IrO}_3$ . (c) Energy levels in  $\text{Na}_2\text{IrO}_3$ . Panels (b) and (c) are taken from Ref. [94].

existence of Kitaev coupling is large spin-orbit coupling. In particular, we are considering transition-metal oxides with partially filled  $d$  orbitals. The reason why this class of materials provide us with the correct features to get bond-directional interactions is as follows: first we consider the  $d^5$  orbital. Under the action of the crystal field, e.g., an octahedral field, the  $d^5$  orbitals are split into (empty)  $e_g$  and (partially filled)  $t_{2g}$  levels. We now have five  $s = 1/2$  electrons in a shell with  $\ell = 1$  orbital momentum. The action of the spin-orbit coupling then further separates the  $j = 3/2$  and  $j = 1/2$  bands, with the first being filled and the second partially filled. This band has a somewhat small bandwidth, which allows for the opening of a Mott gap. What we end up with is a  $j_{\text{eff}} = 1/2$  Mott insulator [96]. This mechanism is schematised in Fig. 4.4(a).

At this point, we have one of the ingredients we need, namely a spin-1/2 system. We can now look at how the bond-directional exchange arises. In order to do so, we need to look at the structure of the materials we are considering. Specifically, we are looking at the bond direction between two  $\text{IrO}_6$  octahedra. There are two possibilities: corner sharing or edge sharing octahedra. The corner sharing bond is also referred to as  $180^\circ$  bond. In this case, there is only one Ir-O-Ir path and the dominant coupling is an isotropic Heisenberg interaction. For edge sharing octahedra, there are two distinct Ir-O-Ir paths with a  $90^\circ$  bond geometry. These two paths lead to destructive interference of the Heisenberg coupling when we restrict the coupling to arise only from the  $j = 1/2$  bands. The study of the full multi-orbital model gives a suppressed Heisenberg exchange, in addition to the Kitaev one. In the end, we have different Ising-like interactions on different bond directions depending on which kind of edge is shared between the octahedra, plus a residual Heisenberg interaction on all bonds. The model taking into account both those interactions is known as the Kitaev-Heisenberg (KH) model [95].

From these considerations, one sees how the honeycomb iridates  $\text{Na}_2\text{IrO}_3$  [Fig. 4.4(b)],

$\alpha$ -Li<sub>2</sub>IrO<sub>3</sub> [97, 98, 99, 100] and H<sub>3</sub>LiIr<sub>2</sub>O<sub>6</sub> [101] can be considered as candidate Kitaev materials. Another transition-metal oxide with a honeycomb lattice is  $\alpha$ -RuCl<sub>3</sub>, which has been proven in the last years to be a very promising candidate for the realisation of a quantum spin liquid state [102, 103, 104]. A fairly recent experiment on this material by Kasahara *et al.* [105] reported quantised thermal Hall conductance for field intensities between 7 and 9 T and field directions in the  $ac$  plane at angles  $\theta = 45^\circ$  and  $\theta = 60^\circ$ , where  $\theta$  is the angle with the  $c$  direction. Though these results are very promising and prove, in principle, the fractionalisation of spins into Majoranas and  $\mathbb{Z}_2$  gauge fluxes, other experiments are needed in order to make a final conclusion on the properties of this material at low temperature and in magnetic field. Moving from 2D to 3D, hyperhoneycomb  $\beta$ - and  $\gamma$ -Li<sub>2</sub>IrO<sub>3</sub> [94, 106] also show bond directional exchange and may host Kitaev physics. Though the original Kitaev model is defined on the honeycomb lattice, it has recently been suggested that a class of materials with effective  $j = 1/2$  moments on a quasi-two-dimensional triangular lattice might support Kitaev interactions [96]. These include the family of hexagonal perovskite Ba<sub>3</sub>Ir <sub>$x$</sub> Ti<sub>3- $x$</sub> O<sub>9</sub>. In particular, the doping case  $x = 1$ , Ba<sub>3</sub>IrTi<sub>2</sub>O<sub>9</sub>, has been suggested to be described by a KH model on the triangular lattice [107]. The phase diagram for the KH model on the triangular lattice is very different from that on the honeycomb one. Non-trivial states include a  $\mathbb{Z}_2$  vortex crystal and a nematic phase, both induced by the Kitaev coupling [107, 108].

Nonetheless, all of the above honeycomb materials show an AFM zigzag magnetically ordered ground state at low temperature and normal pressure [109, 110]. This is due to the presence of further interactions beyond the pure KH model. In particular, it is believed that all of the above materials support off-diagonal  $\Gamma$  interactions, so that the full minimal Hamiltonian reads

$$\mathcal{H}_{JK\Gamma} = - \sum_{\gamma\text{-bonds}} \left[ J \mathbf{S}_i \cdot \mathbf{S}_j + K S_i^\gamma S_j^\gamma + \Gamma (S_i^\alpha S_j^\beta + S_i^\beta S_j^\alpha) \right] \quad (4.41)$$

where  $\alpha$  and  $\beta$  are the two directions perpendicular to  $\gamma = x, y, z$ . Moreover, different materials also host further-neighbour Heisenberg and/or  $\Gamma$  coupling. In all these models, the Kitaev interaction is still believed to be the leading interaction. Hence, as shown in experiments, application of magnetic field or pressure might melt the AFM magnetic order into the spin liquid phase. How this melting of order works is still under debate, but, as  $K$  and  $J$  are the two leading interactions, it provides us with a motivation to further explore and better understand the pure KH model.



# 5 The Kitaev-Heisenberg chain

When we consider the Kitaev-Heisenberg model presented in chapter 4 in a 1D setup, the first thing to notice is the missing  $z$ -rungs (see Fig. 5.1). This makes it impossible for this lattice geometry to support the same states as on the 2D honeycomb lattice. It turns out, however, that this model has a particularly rich phase diagram for a 1D system and the ordered states of the 2D honeycomb KH model can be interpreted in terms of coupled chains.

This chapter is organised as follows: in Sec. 5.1, we give some motivations for studying the 1D KH system. In Sec. 5.2 we present the Hamiltonian and the methods used. We discuss the ground state properties and phase diagram in Sec. 5.3 and Sec. 5.4. Sec. 5.5 shows the spectral properties of the low-lying excitations. Finally, we sum up our findings in Sec. 5.6

## 5.1 Motivation

A temperature-dependent electron energy loss spectroscopy (EELS) measurement has been performed in a K-intercalated  $\text{RuCl}_3$ , denoted as  $\text{K}_{0.5}\text{RuCl}_3$  [111]. The intercalated  $\text{K}^+$  ions provide charge carriers, however, a sharp gap was observed at  $\sim 0.9$  eV, instead of the charge gap  $E_g = 1.1 - 1.2$  eV for the undoped  $\alpha\text{-RuCl}_3$  [112, 113, 114]. This indicates an insulating feature of  $\text{K}_{0.5}\text{RuCl}_3$  and differs from the pseudogap behavior seen for charge localisation in disordered metals. This has been interpreted as half of the  $j = \frac{1}{2}$  pseudospins being replaced by nonmagnetic  $d^6$  ions. Therefore, this insulating state can be pictured as a formation of superlattice by charge disproportionation (charge ordering). Different possible charge ordering patterns are shown in Fig. 5.1. In [111], *ab initio* calculations predict a triangle ordering Fig. 5.1(a). A semiclassical analysis, however, predicts the lowest energy state to be the zigzag chain-type pattern exhibited in Fig. 5.1(c), where chains of nonmagnetic ions are separated by chains of magnetic ions with KH interactions [115]. This charge configuration would be a material realisation of the KH chain, making the work presented in this chapter possibly relevant for real materials. To understand whether this is the case, further experimental and theoretical studies on K-doped  $\text{RuCl}_3$  are needed.

The above motivations lead us to studying the 1D KH model not only for fundamental theoretical reasons, but also as a possible minimal spin model to describe the magnetic properties of the K-intercalated  $\text{RuCl}_3$ . So far, there are few studies on the 1D KH model [116, 117, 118, 119, 120, 121, 122, 123, 124]. Using the DMRG method, we calculate total spin, real-space spin-spin correlation functions, static spin structure factor, central charge, and various order parameters in the ground state. Based on the results, we obtain the ground-state phase diagram, including four long-range ordered and two liquid phases, as a function of the ratio between Heisenberg and Kitaev interactions. Moreover, the relevance of the phase diagram to that of the honeycomb-lattice KH model is discussed.

---

Parts of this chapter have been published as Sci. Rep. 8, 1815 (2018)

Remarkably, all the magnetically ordered states of the honeycomb-lattice KH model can be interpreted in terms of coupled 1D KH chains. Furthermore, we calculate the dynamical spin structure factors via the Lanczos exact diagonalization (ED) technique. The basic low-lying excitations are considered by use of the known six-vertex model and the SWT. The present investigation can thus contribute to an elucidation of the fundamental properties of the K-intercalated  $\text{RuCl}_3$  as well as a better insight in the understanding of the physics of the honeycomb-lattice KH model.

## 5.2 Model and Numerical Methods

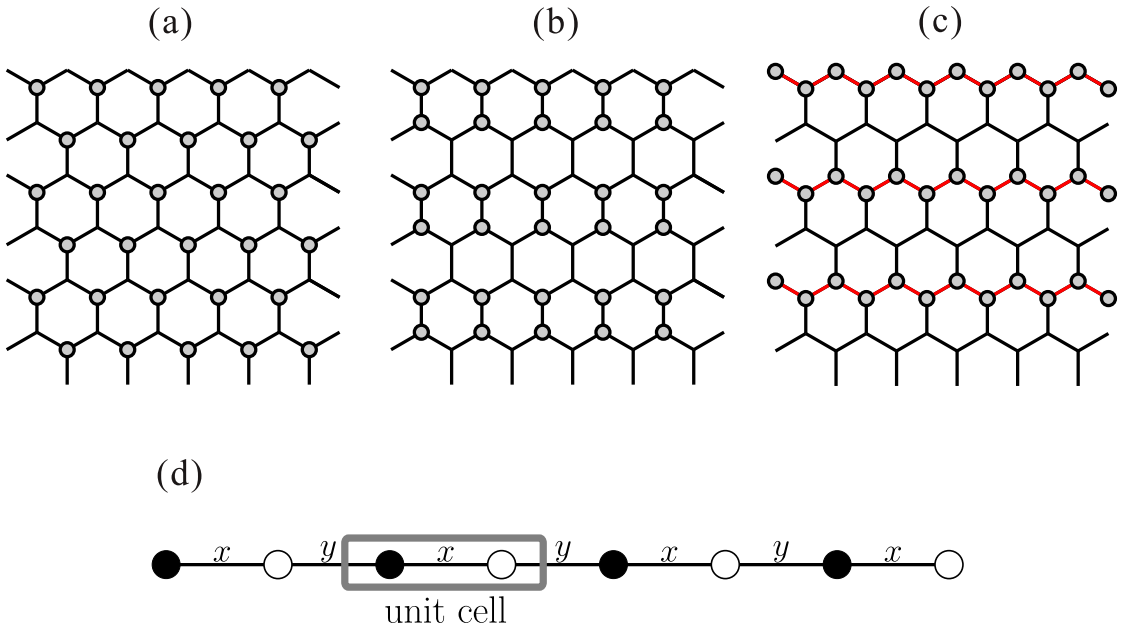


Figure 5.1: Possible charge ordering patterns of  $\text{K}_{0.5}\text{RuCl}_3$ ; (a) triangular, (b) dimer, and (c) zigzag. (d) Lattice structure of the 1D Heisenberg-Kitaev model. The labels ‘ $x$ ’ and ‘ $y$ ’ indicate the  $x$ -bond and  $y$ -bond, respectively (see text).

### 5.2.1 1D Kitaev-Heisenberg Hamiltonian

At present, it is widely believed that the magnetic properties of the undoped  $\alpha\text{-RuCl}_3$  are well described by the KH model on a honeycomb lattice. If we assume the zigzag-type charge ordering in Fig 5.1(c), the zigzag chains are well separated by the nonmagnetic ions. Then, each chain is considered to be a 1D KH model, which is equivalent to a system obtained by removing the  $z$ -bonds from the honeycomb-lattice KH model. The Hamiltonian of the 1D KH model is written as

$$\mathcal{H} = K \sum_{i=1}^{L/2} (S_{2i-1}^x S_{2i}^x + S_{2i}^y S_{2i+1}^y) + J \sum_{i=1}^L \mathbf{S}_i \cdot \mathbf{S}_{i+1} \quad (5.1)$$

for a system with  $L$  sites, where  $\mathbf{S}_i = (S_i^x, S_i^y, S_i^z)$  is a spin- $\frac{1}{2}$  operator at site  $i$ , and the Kitaev and exchange couplings are defined as  $K = \sin \phi$  and  $J = \cos \phi$  via a phase parameter  $\phi$ . Throughout this chapter, we take  $\sqrt{K^2 + J^2} = 1$  as the energy unit. The

system has two kinds of neighbouring links and they appear alternately along the chain. Hence, the structural unit cell contains two lattice sites. Hereafter, we call the links  $(2i-1, 2i)$  and  $(i, 2i+1)$  “ $x$ -link” and “ $y$ -link”, respectively. By rewriting Eq. (5.1) as

$$\begin{aligned}\mathcal{H} &= \frac{2J+K}{4} \sum_{i=1}^L (S_i^+ S_{i+1}^- + S_i^- S_{i+1}^+) + J \sum_{i=1}^L S_i^z S_{i+1}^z + \frac{K}{4} \sum_i^L (-1)^i (S_i^+ S_{i+1}^+ + S_i^- S_{i+1}^-) \\ &\equiv \mathcal{H}_{\text{ex}} + \mathcal{H}_{\text{Ising}} + \mathcal{H}_{\text{dsf}},\end{aligned}$$

we can easily notice that a XXZ Heisenberg chain containing exchange ( $\mathcal{H}_{\text{ex}}$ ) and Ising ( $\mathcal{H}_{\text{Ising}}$ ) terms is disturbed by sign-alternating double-spin-flip ( $\mathcal{H}_{\text{dsf}}$ ) fluctuations [116].

### 5.2.2 Numerical methods

We apply open boundary conditions unless stated otherwise. This enables us to calculate ground-state and low-lying excited-state energies, as well as static quantities, quite accurately for very large finite-size systems. We are thus allowed to carry out an accurate finite-size-scaling analysis to obtain energies and quantities in the thermodynamic limit  $L \rightarrow \infty$ . We hence study chains with several lengths up to  $L = 200$  sites for a given  $\phi$ . Since, in hindsight, the system (5.1) exhibits only commensurate phases in the ground state and the largest magnetic unit cell contains four lattice sites, its size is taken as  $L = 4n$  ( $n$ : integer). For each calculation, we keep up to  $m = 1200$  density-matrix eigenstates in the renormalisation procedure and extrapolate the calculated quantities to the limit  $m \rightarrow \infty$  if needed. Since the SU(2) symmetry is broken in system (5.1) and total  $S^z$  is no longer a good quantum number except at  $\phi = 0, \pi$ , one may have some difficulties in obtaining accurate results in comparison to usual DMRG calculations. Nevertheless, in this way, the maximum truncation error, i.e., the discarded weight, is less than  $1 \times 10^{-10}$  while the maximum error in the ground-state is less than  $1 \times 10^{-8}$ .

For the dynamical properties calculation, we used the Lanczos ED method. To examine the low-energy excitations for each phase, we calculate the dynamical spin structure factor, defined as

$$\begin{aligned}S_\gamma(q, \omega) &= \frac{1}{\pi} \text{Im} \langle \psi_0 | (S_q^\gamma)^\dagger \frac{1}{\hat{H} + \omega - E_0 - i\eta} S_q^\gamma | \psi_0 \rangle \\ &= \sum_\nu |\langle \psi_\nu | S_q^\gamma | \psi_0 \rangle|^2 \delta(\omega - E_\nu + E_0),\end{aligned}\tag{5.2}$$

where  $\gamma$  is  $z$  or  $-$ (+),  $|\psi_\nu\rangle$  and  $E_\nu$  are the  $\nu$ -th eigenstate and the eigenenergy of the system, respectively ( $\nu = 0$  corresponds to the ground state). Under periodic boundary conditions, the spin operators  $S_q^\gamma$  can be precisely defined by

$$S_q^\gamma = \sqrt{\frac{2}{L}} \sum_i S_i^\gamma \exp(iqr_i)\tag{5.3}$$

where  $r_i$  is the position of site  $i$  and the sum runs over either  $i$  even or  $i$  odd sites. They provide the same results. The momentum is taken as  $q = \frac{4\pi}{L}n$  ( $n = 0, \pm 1, \dots, \pm \frac{L}{4}$ ) since the lattice unit cell includes two sites and the number of unit cells is  $\frac{L}{2}$  in a system with  $L$  sites. We calculate both spectral functions  $S_\pm(q, \omega)$  and  $S_z(q, \omega)$  as they are different for all values of  $\phi$  due to the breaking of SU(2) symmetry except at  $\phi = 0$  and  $\pi$ . We

study chains with  $L = 24$ , namely, 12 unit cells, by the Lanczos ED method. As shown below, system (5.1) contains only commensurate phases with unit cell containing one, two, or four sites. Therefore, a quantitative discussion of the low-lying excitations is possible even within the  $L = 24$  chain.

## 5.3 Ground-state properties

### 5.3.1 Quantum phase transitions

Let us first look at the ground-state energy and total spin with respect to  $\phi$  in order to capture the overall appearance of quantum phase transitions. The results, using a periodic 24-site KH chain, are shown in Fig. 5.2. We clearly see discontinuities in the first derivative of the ground-state energy at four values:  $\phi = \frac{\pi}{2}, \pi, \frac{3\pi}{2}$ , and  $\approx 1.65\pi$ , which indicate the first-order phase transitions. The second derivative  $-\partial^2 E_0 / \partial \phi^2$  is, in a precise sense, continuous except for the above four  $\phi$  points, nonetheless, there exists a distinguishable peak around  $\phi \approx 0.65\pi$ , which may corresponds to a second-order (or continuous) phase transition (see inset in Fig. 5.2(b)). Furthermore, as shown below, we find another phase transitions at  $\phi = 0$ . Therefore, we suggest that the simple 1D model (5.1) exhibits a variety of phases including six quantum phase transitions. It will be confirmed by studying various corresponding order parameters or spin-spin correlation functions. We also confirm that the ground-state energy of the 1D KH chain is always lower than that given by the dimer-type charge ordering on the honeycomb shown in Fig. 5.1(b) [see Fig. 5.2(a)].

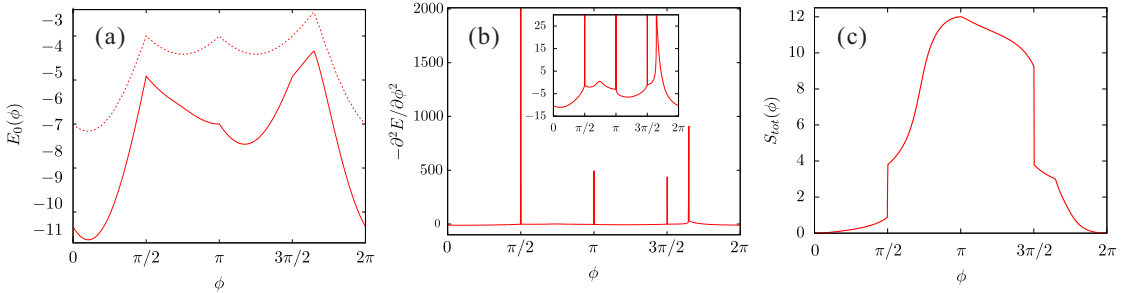


Figure 5.2: (a) Ground-state energy  $E_0$ , (b) the second derivative of  $E_0$  with respect to  $\phi$ , and (c) total spin  $S_{tot}$  as a function of  $\phi$ , obtained with a 24-site periodic Kitaev-Heisenberg chain. Dotted line in (a) indicates ground-state energy for the dimer-type charge ordering.

### 5.3.2 Ferromagnetic- $xy$ phase ( $\pi < \phi < \frac{3\pi}{2}$ )

Since both  $K$  and  $J$  are ferromagnetic (FM), a long-range FM ordered state is naively expected in the range  $\pi < \phi < \frac{3\pi}{2}$ . At the spin isotropic point  $\phi = \pi$ , the spins can align along any arbitrary spatial direction due to SU(2) spin rotation invariance and the total spin takes the maximum value  $\frac{S_{tot}}{L} = \frac{1}{2}$  [see Fig. 5.2(c)]. Away from the isotropic point, the SU(2) symmetry is broken to U(1) and the configurations for higher  $|S^z|$  sectors are

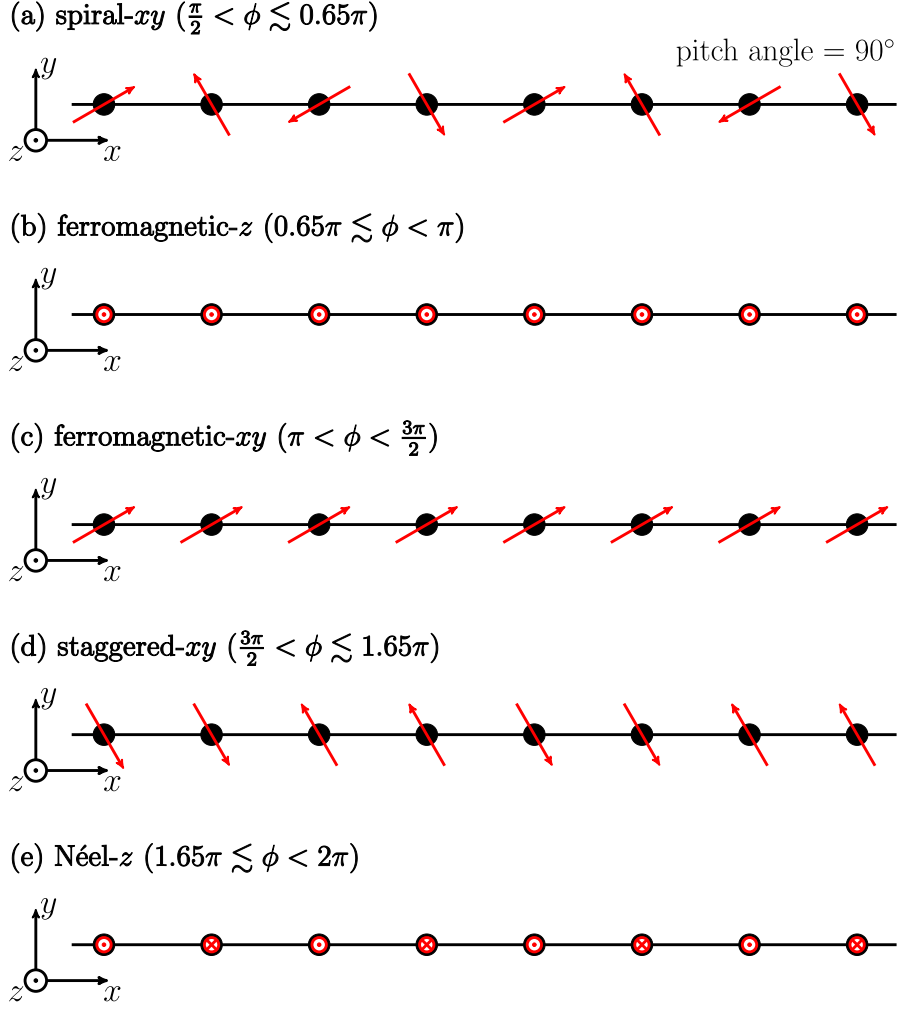


Figure 5.3: Schematic pictures of five states realised in the 1D KH model, except the TLL state at  $0 < \phi < \frac{\pi}{2}$ . In the phases (a)(c)(d), the spins lie mostly on the  $xy$ -plane and these states are rotational invariant around the  $z$ -axis. In phases (b)(e), the spins almost align along the  $z$ -direction and a state having opposite spin directions is degenerate.

projected out [see Fig. 5.3(c)]. When  $\phi$  is still close to  $\pi$  ( $-J \gg -K > 0$ ), the ground state is approximately expressed as

$$|\Psi_0\rangle = \frac{1}{\sqrt{\mathcal{N}}} \sum_m |\psi_m\rangle, \quad (5.4)$$

where  $|\psi_m\rangle$  is a basis in real space, namely each site state is represented by either spin-up ( $\uparrow$ ) or spin-down ( $\downarrow$ ). The basis is here restricted to a  $S_{\text{tot}}^z = \sum_{i=1}^L \langle S_i^z \rangle = 0$  subspace, so that  $m$  is summed over all possible combinations of spin configuration with  $\frac{L}{2}$  up and  $\frac{L}{2}$  down spins in a  $L$  lattice sites.  $\mathcal{N}$  is the total number of the spin configurations, i.e.,  $\frac{L!}{(L/2)!(L/2)!}$ . The wave function (5.4) becomes exact in the isotropic spin limit  $\phi = \pi+$ . Accordingly, the spin-spin correlations have long-range FM ordering for all three spin components:  $\langle S_i^x S_j^x \rangle = \langle S_i^y S_j^y \rangle = \frac{1}{6}$  and  $\langle S_i^z S_j^z \rangle = -\frac{1}{12}$  for any  $i \neq j$ . Taking the spin isotropic Hamiltonian at  $\phi = \pi+$  as an unperturbed one, the unperturbed ground state is given by Eq. (5.4). When  $\phi - \pi \ll 1$ , the perturbed Hamiltonian can be written as

$\mathcal{H}' \approx \frac{\phi-\pi}{4} \sum_i (S_i^+ S_{i+1}^- + S_i^- S_{i+1}^+)$  and the lowest-order energy correction is  $E' = \frac{\phi-\pi}{4}$ . Therefore, with increasing  $\phi$  from  $\pi$ , the AFM fluctuations increase and the long-range FM ordering is weakened. Nonetheless, the correlations  $\langle S_i^x S_j^x \rangle$  and  $\langle S_i^y S_j^y \rangle$  retain the same asymptotic behaviours indicating the long-range FM ordering until  $\phi = \frac{3\pi}{2}$ , characterised by the saturation to a finite negative value in the limit  $|i-j| \rightarrow \infty$ ; whereas,  $\langle S_i^z S_j^z \rangle$  decays in a power law with  $|i-j|$ . This is because the AFM fluctuations are mainly introduced along the  $z$ -direction. It is confirmed by a slow decrease of the total spin as a function of  $\phi$ , as seen in Fig. 5.2(c). We thus call this state FM- $xy$  state. A collapse of the long-range FM ordering is detected by a drop-off of the total spin at  $\phi = \frac{3\pi}{2}$ , suggesting a first-order transition.

### 5.3.3 Ferromagnetic- $z$ phase ( $0.65\pi \lesssim \phi < \pi$ )

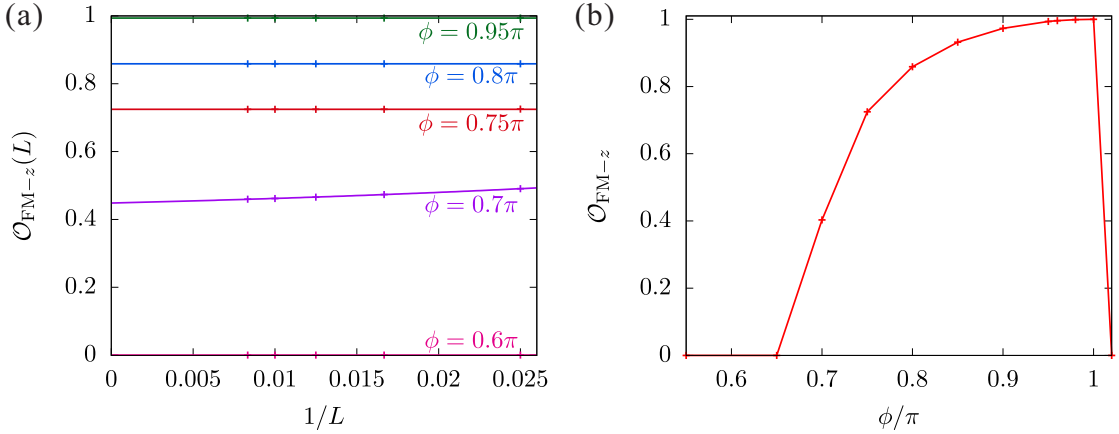


Figure 5.4: (a) Finite-size scaling analyses of the FM- $z$  order parameter with polynomial fitting functions. (b) Extrapolated values of the FM- $z$  order parameter  $\mathcal{O}_{\text{FM-}z}$  to the thermodynamic limit  $L \rightarrow \infty$  as a function of  $\phi$ .

A long-range FM ordered state stabilises also at  $\frac{3\pi}{4} < \phi < \pi$ , where all the exchange tensors are FM since  $J + K$  is negative despite positive  $K$ . However, in contrast to the FM- $xy$  state, spin alignment along the  $z$ -direction is favoured because of the easy-axis-XXZ-like interactions  $|\frac{2J+K}{2}| < |J|$ . Therefore, the most dominant spin configurations are given by the highest  $|S^z|$  sectors, i.e., the ground state is expressed as

$$|\Psi_0\rangle = \frac{1}{\sqrt{2}}(|\uparrow\rangle + |\downarrow\rangle), \quad (5.5)$$

with  $|\uparrow\rangle = |\cdots \uparrow\uparrow\uparrow\uparrow\uparrow \cdots\rangle$  and  $|\downarrow\rangle = |\cdots \downarrow\downarrow\downarrow\downarrow\downarrow \cdots\rangle$ . This wave function is exact in the isotropic limit of  $\phi = \pi$ . We call this type of long-range FM ordering FM- $z$  state. Let us take Eq. (5.5) as the unperturbed ground state. For  $\pi - \phi \ll 1$ , the perturbed Hamiltonian can be written as  $\mathcal{H}' \approx \frac{(\pi-\phi)^2}{2} \sum_i S_i^z S_{i+1}^z$ . This is an Ising-like AFM correlation and it clearly disturbs the FM- $z$  state. However, the lowest-order correction to the ground-state energy is  $E' = \frac{(\pi-\phi)^2}{8}$ . It means that the perturbation acts only gradually with being away from the isotropic point  $\phi = \pi$ . As a result, the total spin is not that much reduced around  $\phi = \pi$  in the FM- $z$  phase. To estimate the lower bound of the FM- $z$  phase, we shall define the FM- $z$  order parameter. A state

with long-range FM ordering is a state with broken spin symmetry along the  $z$ -direction; macroscopically, there are two degenerate ground states  $|\Psi_0\rangle \approx |\uparrow\rangle$  and  $|\Psi_0\rangle \approx |\downarrow\rangle$ . Applying open boundary conditions, one of the two ground states is picked imposing initial conditions on the calculation. The long-range ordered state is thus directly observable as a symmetry-broken state in our DMRG calculations. The order parameter is defined as

$$\mathcal{O}_{\text{FM-}z} = 2 \lim_{L \rightarrow \infty} \langle S_{L/2}^z \rangle \quad (5.6)$$

The finite-size scaling analysis is performed. The extrapolated values in the thermodynamic limit are shown in Fig. 5.4. Notably, the FM- $z$  state survives even at  $\phi < \frac{3\pi}{4}$ , where a part of the interactions is AFM, i.e.,  $J + K > 0$ . Nevertheless, the long-ranged FM order is drastically suppressed by the AFM fluctuations at  $\phi < \frac{3\pi}{4}$  and completely destroyed at  $\phi \approx 0.65\pi$ . This is understandable by noting that the XXZ-like interaction is actually proportional to  $2J + K$  rather than just  $J + K$  and  $2 \cos \phi + \sin \phi$  vanishes at  $\phi \approx 0.65\pi$ . The order parameter has no jump at the transition point, suggesting a second-order phase transition.

#### 5.3.4 Spiral- $xy$ phase ( $\frac{\pi}{2} < \phi \lesssim 0.65\pi$ )

As shown above, the FM- $z$  phase remains down to  $\phi \approx 0.65\pi$ . Then, we look at which kind of phase appears for smaller values of the angle parameter at  $\frac{\pi}{2} < \phi \lesssim 0.65\pi$ . In this range,  $K$  is AFM,  $J$  is FM, and  $K \gg -J$ . On the  $x$ -links, the  $x$ -components of spins tend to be antiparallel due to the strong AFM interaction along the  $x$  direction; whereas their  $y$ -components tend to be parallel due to FM  $J$  term. The  $y$ -links behave in the same way. Eventually, the spins lie on the  $xy$  plane and rotate by  $90^\circ$  from one site to the next. The magnetic unit cell is twice as large as the structural unit cell, i.e., including four lattice sites [see Fig. 5.3(a)]. We call this state spiral- $xy$  state. To confirm this magnetic structure, we calculate the static spin structure factor, defined as

$$S^\gamma(q) = \frac{2}{L} \sum_{k,l} \langle S_k^\gamma S_l^\gamma \rangle e^{-iq(k-l)}, \quad (5.7)$$

where the length of the structural unit cell, i.e., two lattice spacings, is taken to be unity. The DMRG results with  $L = 60$  cluster are shown in Fig. 5.5. Near the AFM Kitaev point  $\phi = \frac{\pi}{2}$ ,  $S^x(q) + S^y(q)$  has a large  $q = \pi$  peak indicating a periodicity of four lattice sites on the  $xy$ -plain. On the other hand,  $S_z(q)$  is almost zero for all  $q$  since the FM  $z$  interaction  $J$  is tiny compared to the dominant AFM  $x$  or  $y$  interactions  $J + K$ . With increasing  $\phi$ , the  $q = \pi$  peak becomes lower and a  $q = 0$  peak in  $S^z(q)$  develops. Basically, the spins are tilted in one direction along the  $z$ -axis with keeping the periodicity on the  $xy$ -plain. Those peak heights are reversed around the transition point  $\phi = 0.65\pi$  from the spiral- $xy$  to the FM- $z$  phases. We note that the height of the  $q = 0$  peak in  $S^z(q)$  coincides with the FM- $z$  order parameter. As shown in Fig. 5.6, the spin-spin correlations decay as a power law for all the spin components in the spiral- $xy$  phase. It means that the  $q = \pi$  peak in  $S^x(q) + S^y(q)$  disappears in the thermodynamic limit: the spiral- $xy$  structure is not long-range ordered.

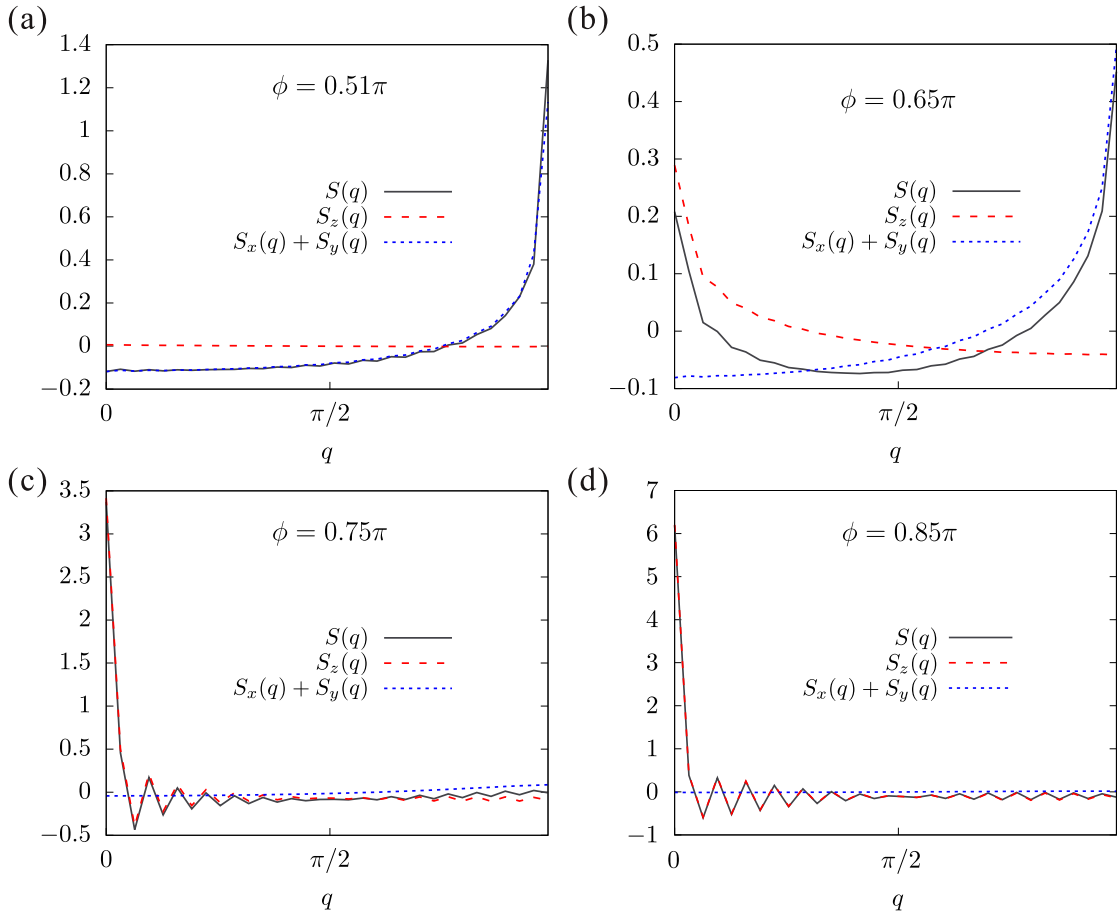


Figure 5.5: Static spin structure factors for (a)  $\phi = 0.51\pi$ , (b)  $\phi = 0.65\pi$ , (c)  $\phi = 0.75\pi$ , and (d)  $\phi = 0.85\pi$ .

### 5.3.5 Néel- $z$ ordered phase ( $1.65\pi \lesssim \phi < 2\pi$ )

Next, we turn to the parameter region  $\frac{3\pi}{2} < \phi < 2\pi$  ( $J > 0$ ,  $K < 0$ ). We start from the SU(2) symmetric limit  $\phi = 2\pi$ , where the system is the original 1D AFM Heisenberg model. The ground-state wave function can be exactly obtained and it is known to have  $S_{\text{tot}} = 0$ . So, the first perturbative correction is given by  $\mathcal{H}' \approx (\phi - 2\pi) \sum_i (S_i^+ S_{i+1}^- + S_i^- S_{i+1}^+)$ , which provides an easy-axis anisotropy to the system. Therefore, the possibility of a continuous Néel- $z$  order transition is conceived by analogy to the easy-axis anisotropic XXZ chain. For small  $2\pi - \phi$ , the magnetisation is expect to grow gradually with

$$M \simeq \frac{\pi}{2(2\pi - \phi)} \exp \left\{ -\frac{\pi^2}{2\sqrt{2(2\pi - \phi)}} \right\}. \quad (5.8)$$

Let us confirm it numerically. In the long-range Néel- $z$  ordered state, the translational symmetry is broken in a finite system due to the Friedel oscillation under open boundary conditions, so that the Néel- $z$  state can be directly observed by extracting one of the degenerate states, like in the FM- $z$  state. Generally, the Friedel oscillations in the centre of the system decay as a function of the system length. If the amplitude at the centre of the system persists for arbitrary system lengths, it corresponds to a long-range ordering.



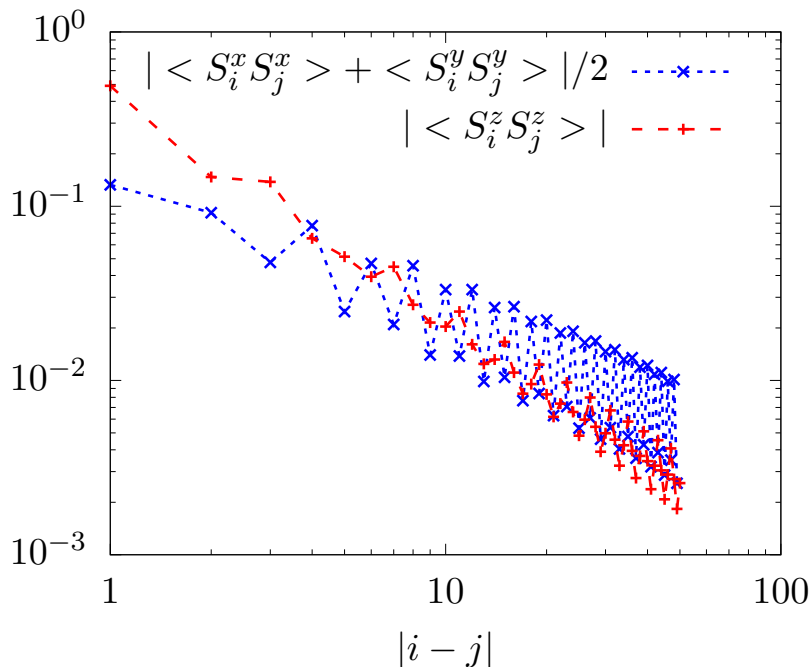


Figure 5.6: Log-log plot of the spin-spin correlation functions as a function of distance at  $\phi = 0.6\pi$ .

Here, we are interested in the formation of alternating spin flip along the  $z$ -direction. Thus, the Néel- $z$  order parameter is defined as

$$\mathcal{O}_{\text{Néel}} = \lim_{L \rightarrow \infty} |\langle S_{L/2}^z \rangle - \langle S_{L/2+1}^z \rangle|. \quad (5.9)$$

This quantity is equivalent to the magnetisation  $M$  in the thermodynamic limit. The finite-size scaling analyses of  $\mathcal{O}_{\text{Néel}}$  was performed using the results for systems with up to  $L = 120$  and the extrapolated values to the thermodynamic limit were obtained. They are shown in Fig. 5.7. We indeed see a slow increase of  $\mathcal{O}_{\text{Néel}}$  near the SU(2) symmetric limit  $\phi = 2\pi$ . Further with decreasing  $\phi$ , the order parameter develops up to  $\mathcal{O}_{\text{Néel}} = 1$  and drops down to 0 at  $\phi \approx 1.65\pi$ .

In fact, this lower  $\phi$ -boundary of the Néel- $z$  ordered phase can be estimated analytically. At  $\phi = \tan^{-1}(-2) \approx 1.6476\pi$ , the exchange term  $\mathcal{H}_{\text{ex}}$  disappears in the Hamiltonian (5.1) and the system is just written as a sum of double-spin-flip and Ising parts

$$\begin{aligned} \mathcal{H} &= \mathcal{H}_{\text{dsf}} + \mathcal{H}_{\text{Ising}} \\ &= \frac{K}{4} \sum_i^L (-1)^i (S_i^+ S_{i+1}^+ + S_i^- S_{i+1}^-) + \frac{J}{4} \sum_i^L S_i^z S_{i+1}^z. \end{aligned} \quad (5.10)$$

Each of the partition Hamiltonians  $\mathcal{H}_{\text{dsf}}$  and  $\mathcal{H}_{\text{Ising}}$  is exactly solvable. For  $\mathcal{H}_{\text{dsf}}$ , the system is regarded as noninteracting fermions with “pair hopping” and the ground-state wave function is

$$|\Psi_0\rangle = \frac{1}{\sqrt{\mathcal{N}}} \sum_{\mathcal{C}} \prod_{i \in (\mathcal{C}), \gamma \in (\mathcal{C})} (-1)^{i-1} S_i^\gamma S_{i+1}^\gamma |\uparrow\rangle, \quad (5.11)$$

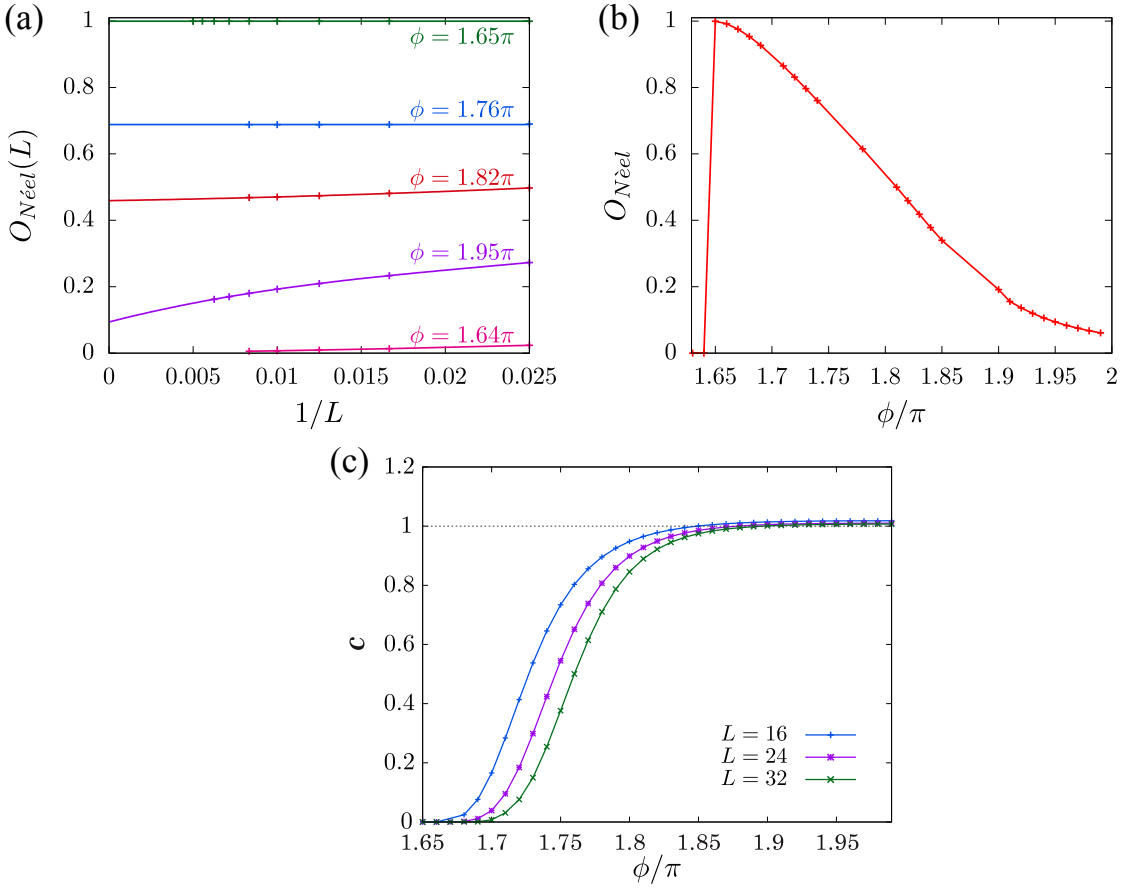


Figure 5.7: (a) Finite-size scaling analyses for the Néel- $z$  order parameter  $\mathcal{O}_{N\acute{e}el}$  with polynomial fitting functions. (b) The extrapolated values of  $\mathcal{O}_{N\acute{e}el}$  to the thermodynamic limit as a function of  $\phi$ . (c) Central charge, calculated with periodic chains, as a function of  $\phi$  for several chain lengths.

where  $\mathcal{C}$  is summed over all possible spin configurations created by the double spin flips starting from  $|\uparrow\rangle$  or  $|\downarrow\rangle$  ( $\mathcal{N} =_L C_{L/2}$ ),  $i$  and  $\gamma(=+ \text{ or } -)$  are taken to create the configuration  $\mathcal{C}$ . While, for  $\mathcal{H}_{\text{Ising}}$ , the system is a simple Ising one and the ground-state wave function is

$$|\Psi_0\rangle = \frac{1}{\sqrt{2}} \sum_{\sigma} \prod_{i=1}^{L/2} c_{2i-1,\sigma}^{\dagger} c_{2i,\bar{\sigma}}^{\dagger} |0\rangle, \quad (5.12)$$

where  $|0\rangle$  is the vacuum state. The ground-state wave functions (5.11) and (5.12) are orthogonal since they do not share the same spin configurations. It means the ground state is two-fold degenerate at the critical point  $\phi = \tan^{-1}(-2)$ . The ground-state energy is  $E_0 = -\frac{L \cos \phi}{4}$ . This degeneracy is lifted away from  $\phi = \tan^{-1}(-2)$ . Eq. (5.12) is the ground state for larger- $\phi$  side, namely, in the Néel- $z$  phase; while, Eq. (5.11) for lower- $\phi$  side (see Sec. 5.3.6). This is consistent with the fact that  $\mathcal{O}_{N\acute{e}el}$  reaches exactly 0.5 at  $\phi = \tan^{-1}(-2)$ , as shown in Fig. 5.7(b). Therefore, the ground-state wave function is completely changed at  $\phi = \tan^{-1}(-2)$  and it clearly suggests a first-order transition. This is also confirmed by the jump of  $\mathcal{O}_{N\acute{e}el}$  as well as by the singularity in  $-\partial^2 E_0 / \partial \phi^2$  at  $\phi \approx 1.65\pi$ .

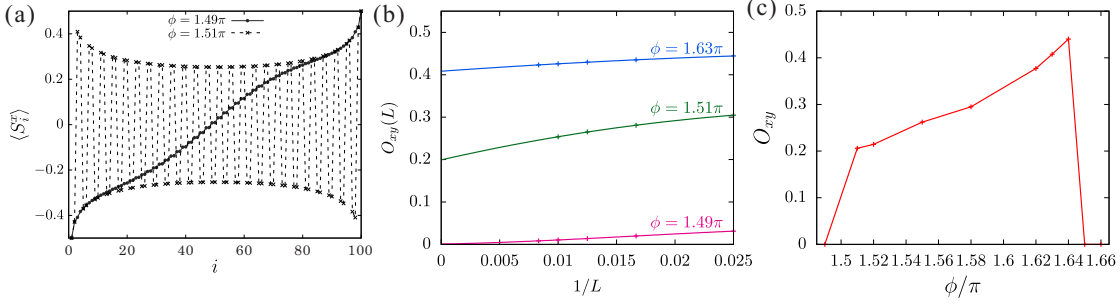


Figure 5.8: (a) The  $x$ -component of local spin, where opposite magnetic fields  $\pm 10$  are applied at either end of the system. (b) Finite-size scaling analyses for the staggered- $xy$  order parameter with polynomial fitting functions. (c) The extrapolated values of  $\mathcal{O}_{xy}$  to the thermodynamic limit as a function of  $\phi$ .

### 5.3.6 Staggered- $xy$ ordered phase ( $\frac{3\pi}{2} < \phi \lesssim 1.65\pi$ )

Let us then consider a region at  $\frac{3\pi}{2} < \phi \lesssim 1.65\pi$ , where the signs of Heisenberg and Kitaev terms counterchange from the spiral- $xy$  state. This may mean the local spin structure is similar to the spiral- $xy$  state. As discussed above, the system has a first-order transition at  $\phi = \tan^{-1}(-2) \approx 1.65\pi$ . In the lower- $\phi$  vicinity ( $\phi \lesssim 1.65$ ) the ground state is exactly given by Eq. (5.11), which derives asymptotic behaviours of the spin-spin correlations:  $\langle S_0^x S_j^x \rangle = \frac{\alpha^2}{4\sqrt{2}} \cos \frac{\pi}{2} [(j + \frac{1}{2})]$ ,  $\langle S_0^y S_j^y \rangle = \frac{\beta^2}{4\sqrt{2}} \cos \frac{\pi}{2} [(j - \frac{1}{2})]$ ,  $\langle S_0^z S_j^z \rangle = 0$ , and  $\langle \mathbf{S}_0 \mathbf{S}_j \rangle = \frac{1}{4} \cos(\frac{\pi}{2} j) + \frac{\alpha^2 - \beta^2}{4} \sin(\frac{\pi}{2} j)$ . Since the system is rotationally invariant around the  $z$ -axis, the coefficients  $\alpha$  and  $\beta$  can take arbitrary real numbers under the condition  $\alpha^2 + \beta^2 = 1$ . As illustrated in Fig. 5.3(d), all the spins lie on the  $xy$ -plane and the magnetic unit cell contains four lattice sites as in the spiral- $xy$  state. However, the crucial difference from the spiral- $xy$  state is that this  $xy$  state exhibits long-range ordering, which is clearly indicated by the correlation functions. We call this state staggered- $xy$  state, since it resembles a Néel-like state with a period of four sites.

We then investigate the  $\phi$ -dependence of this  $xy$  state. Applying a staggered field along the  $x$ -direction on both open system edge sites, the presence or absence of the long-range staggered- $xy$  order can be determined by studying the decay of the  $x$ -component of local spin  $\langle S_i^x \rangle$  as the Friedel oscillation. Thus, the staggered- $xy$  order parameter is defined at the center of the system as

$$\mathcal{O}_{xy} = \frac{1}{2} \lim_{L \rightarrow \infty} |\langle S_{L/2}^x \rangle - \langle S_{L/2+1}^x \rangle|. \quad (5.13)$$

In the upper and lower vicinity of  $\phi \approx 1.65\pi$ ,  $\mathcal{O}_{xy} = 0$  and  $\frac{1}{2}$  are obtained from Eqs. (5.11) and (5.12), respectively. For the other  $\phi$  values the profile of the  $x$ -component of local spin and the finite-size scaling of the order parameter are shown in Fig. 5.8(a)(b). The extrapolated values of  $\mathcal{O}_{xy}$  to the thermodynamic limit are plotted in Fig. 5.8(c). We can see that the order parameter jumps at the both phase boundaries suggesting first-order transitions. The collapse of the staggered- $xy$  ordering at the lower boundary  $\phi = \frac{3\pi}{2}$  is clearly confirmed by the profile of  $\langle S_i^x \rangle$ , as shown in Fig. 5.8(a).

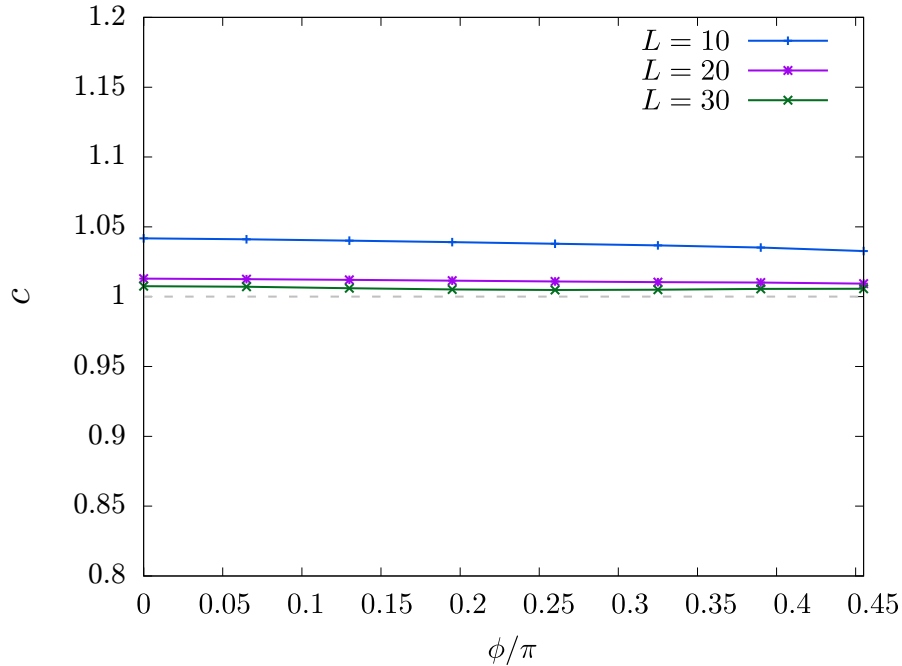


Figure 5.9: Central charge, calculated with periodic  $L = 10, 20,$  and  $30$  chains, as a function of  $\phi$ .

### 5.3.7 Tomonaga-Luttinger-liquid phase ( $0 \leq \phi < \frac{\pi}{2}$ )

The remaining region is  $0 \leq \phi < \frac{\pi}{2}$ . At  $\phi = 0$  the system is equivalent to the spin-isotropic AFM Heisenberg chain, which is a gapless spin liquid. It is known that the low-energy physics is described by a Tomonaga-Luttinger (TL) model with a boson field, which is equivalent to the unity central charge ( $c = 1$ ) conformal field theory (CFT) [125]. Let us now consider what happens when we move away from  $\phi = 0$ . At  $0 < \phi < \frac{\pi}{2}$  the deviating interactions from the spin-isotropic Hamiltonian are written as

$$\mathcal{H}_{\text{aniso}} = \frac{K}{4} \sum_{i=1}^L [S_i^+ S_{i+1}^- + S_i^- S_{i+1}^+ + (-1)^i (S_i^+ S_{i+1}^+ + S_i^- S_{i+1}^-)]. \quad (5.14)$$

Obviously, these interactions cannot produce any explicit magnetic order, since they only enhance the quantum fluctuations. It is a nontrivial question, however, whether the  $c = 1$  CFT is conserved. To examine it, we directly calculate the central charge, which can be obtained from the von Neumann entanglement entropy in the DMRG procedure as follows: Let us consider a quantum 1D periodic system with length  $L$ . We have described the von Neumann entanglement entropy (EE) in Sec. 3.2.5: for a subsystem with length  $l$ , we have to fix  $A = l$  and  $B = L - l$ . We denote the EE for this subsystem as  $S_L(l)$ . Using the CFT, the entropy of the subsystem with length  $l$  for a fixed system length  $L$  has been derived as [126, 127, 128]:

$$S_L(l) = \frac{c}{3} \ln \left[ \frac{L}{\pi} \sin \left( \frac{\pi l}{L} \right) \right] + s_1 \quad (5.15)$$

where  $s_1$  is a non-universal constant. In the DMRG calculations this quantity can be accurately estimated by the second derivative of Eq. (5.15) with respect to  $l$  [129], namely,

$$c = -\frac{3L^2}{\pi^2} \left. \frac{\partial^2 S_L(l)}{\partial l^2} \right|_{l=\frac{L}{2}}. \quad (5.16)$$

The results for periodic chains with  $L=10, 20,$  and  $30$  are plotted in Fig. 5.9. We see a quick convergence to  $c = 1$  with increasing system size in the whole range of  $0 \leq \phi < \frac{\pi}{2}$ . Hence, we confirm the system remains in the TL liquid state as far as both  $J$  and  $K$  are AFM. Similarly, we studied the central charge in the Néel- $z$  phase. The results for periodic chains with  $L = 16, 24,$  and  $32$  are plotted in Fig. 5.7(c). Although  $c = 0$  should be retained in the Néel- $z$  phase, we see a very slow converge to  $c = 0$  with increasing  $L$  near  $\phi = 2\pi$ , reflecting the tiny magnetisation.

### 5.3.8 Kitaev points

As discussed above, the Kitaev points are singular, not adiabatically connected to the neighbouring phases. At these points  $\phi = \pm\frac{\pi}{2}$ , the Heisenberg interaction  $J$  vanishes in our Hamiltonian Eq. (5.1) and it is reduced to

$$\mathcal{H} = \pm K \sum_{x\text{-links}} S_i^x S_{i+1}^x \pm K \sum_{y\text{-links}} S_i^y S_{i+1}^y \quad (5.17)$$

In order to make the notation easier, we here focus on the case of  $\phi = -\pi/2$ . Note that the case of  $\phi = \frac{\pi}{2}$  can be similarly considered. It is convenient to fermionize the Hamiltonian (5.17). By applying the Jordan-Wigner transformation as in Chapter 4

$$S_i^z = 2c_i^\dagger c_i - 1 \quad (5.18)$$

$$S_i^+ = \prod_{k=1}^{i-1} (-S_k^z) c_i^\dagger \quad (5.19)$$

$$S_i^- = \prod_{k=1}^{i-1} (-S_k^z) c_i \quad (5.20)$$

we can rewrite the spin operators in Eq. (5.17) by fermion operators, and we obtain:

$$\mathcal{H} = \sum_{x\text{-links}} (c_{b,i}^\dagger - c_{b,i})(c_{w,i}^\dagger + c_{w,i}) - \sum_{y\text{-links}} (c_{w,i}^\dagger + c_{w,i})(c_{b,i+1}^\dagger - c_{b,i+1}), \quad (5.21)$$

where  $c_{b,i}$  and  $c_{w,i}$  are the fermion annihilation operators at the black and white labelling sites in the  $i$ -th unit cell, illustrated in Fig. 5.1(d), respectively. Generally, it is possible to write fermion operators in terms of Majorana fermions defined as:

$$c_{b,i}^\dagger = \frac{b_{1,i} - ib_{2,i}}{2} \quad (5.22)$$

$$c_{w,i}^\dagger = \frac{w_{1,i} - iw_{2,i}}{2}. \quad (5.23)$$

With these operators Eq. (5.21) is transformed to

$$\mathcal{H} = -i\frac{K}{4} \sum_{x\text{-links}} b_{2,i}w_{1,i} + i\frac{K}{4} \sum_{y\text{-links}} w_{1,i}b_{2,i+1}. \quad (5.24)$$

We immediately notice that the Majoranas  $b_1, w_2$  are not included in the Hamiltonian (5.24). We then define new, non local, fermion operators as

$$d_i^\dagger = \frac{w_{1,i} - ib_{2,i}}{2} \quad (5.25)$$

$$d_i = \frac{w_{1,i} + ib_{2,i}}{2}, \quad (5.26)$$

where the indices  $i$  run over the unit cells instead of over the lattice sites [see Fig. (5.1)(d)]. Using these operators, (5.24) can be expressed as

$$\mathcal{H} = \frac{K}{2} \sum_i d_i^\dagger d_i - \frac{K}{4} \sum_i (d_i^\dagger d_{i+1} + d_i d_{i+1} + \text{h.c.}). \quad (5.27)$$

This describes a  $p$ -wave paired superconductor [130]. The exact solution for the ground state is easily obtained by a Fourier transformation:

$$\mathcal{H} = \frac{1}{2} \sum_q \left[ \varepsilon_q d_q^\dagger d_q + i\frac{\Delta_q}{2} (d_q^\dagger d_{-q}^\dagger + \text{h.c.}) \right] \quad (5.28)$$

where  $\varepsilon_q = -\frac{K}{2}(\cos q + 1)$  and  $\Delta_q = \frac{K}{2} \sin q$ . Using a Bogoliubov transformation, this can be diagonalised and the quasiparticle excitation is given by

$$E_q = \pm \frac{1}{4} \sqrt{\varepsilon_q^2 + \Delta_q^2}. \quad (5.29)$$

Thus, we can confirm the system is still in the gapless region. The ground-state energy is calculated as

$$\frac{E_0}{L} = \frac{1}{L} \sum_q (-E_q) = \frac{1}{2\pi} \int_{-\pi}^{\pi} dq (-E_q) = -\frac{K}{2\pi}. \quad (5.30)$$

To consider the meaning of the Majoranas  $b_1, w_2$  which do not appear explicitly in the Hamiltonian (5.24), we take a possible recombination of them into new fermion operators:

$$\tilde{d}_i^\dagger = \frac{b_{1,i} - iw_{2,i}}{2} \quad (5.31)$$

$$\tilde{d}_i = \frac{b_{1,i} + iw_{2,i}}{2} \quad (5.32)$$

We can now trace these back to the initial spin operators. Using Eqs. (5.22) and (5.23), we get

$$\tilde{d}_i^\dagger = \frac{1}{2} (c_{b,i}^\dagger + c_{b,i} + c_{w,i}^\dagger - c_{w,i}). \quad (5.33)$$

Moreover, the inverse of Jordan-Wigner transformation used to obtain Eq. (5.21) reads

$$c_{w,i}^\dagger = \prod_{k=1}^{i-1} \prod_{k'=b,w} (-S_{k,k'}^z) (-S_{b,i}^z) S_{w,i}^+ \quad (5.34)$$

$$c_{w,i} = \prod_{k=1}^{i-1} \prod_{k'=b,w} (-S_{k,k'}^z) (-S_{b,i}^z) S_{w,i}^- \quad (5.35)$$

$$c_{b,i}^\dagger = \prod_{k=1}^{i-1} \prod_{k'=b,w} (-S_{k,k'}^z) S_{b,i}^+ \quad (5.36)$$

$$c_{b,i} = \prod_{k=1}^{i-1} \prod_{k'=b,w} (-S_{k,k'}^z) S_{b,i}^- \quad (5.37)$$

We can now use this transformation to rewrite in terms of the initial spin operators as:

$$\tilde{d}_i^\dagger = \prod_{k=1}^{i-1} \prod_{k'=b,w} (S_{k,k'}^z) (S_{b,i}^x - iS_{b,i}^z S_{w,i}^y). \quad (5.38)$$

Thus, the Majorana operators can be expressed by spin operators, like

$$b_{1,i} = \tilde{d}_i^\dagger + \tilde{d}_i = 2 \prod_{k=1}^{i-1} (-S_{k,k'}^z) S_{b,i}^x \quad (5.39)$$

$$w_{2,i} = i(\tilde{d}_i^\dagger - \tilde{d}_i) = 2 \prod_{k'=w,b} (-S_{k',k}^z) (-S_{b,i}^z) (-S_{w,i}^y). \quad (5.40)$$

We now confirm that the system has a free spin per unit cell at the Kitaev points. Therefore, the dimensionality of the ground-state manifold, or number of zero Majorana modes, is  $2^{\frac{L}{2}-1}$  for periodic chain and  $2^{\frac{L}{2}}$  for open chain. Some more details are given below.

It is also possible to derive the same results as Eqs. (5.39) and (5.40) by taking a different combination of the Majoranas from Eqs. (5.31) and (5.32):

$$B_i^\dagger = \frac{b_{1,i} - ib_{1,i+1}}{2} \quad (5.41)$$

$$W_i^\dagger = \frac{w_{2,i} - iw_{2,i+1}}{2}. \quad (5.42)$$

From Eqs. (5.22) and (5.23), we have

$$B_i^\dagger = \frac{1}{2}(c_{b,i}^\dagger + c_{b,i} - ic_{b,i+1}^\dagger - ic_{b,i+1}) \quad (5.43)$$

$$W_i^\dagger = \frac{1}{2}(c_{w,i+1}^\dagger - c_{w,i+1} + ic_{w,i}^\dagger - ic_{w,i}). \quad (5.44)$$

Using (5.35)-(5.37), we obtain

$$B_i^\dagger = \prod_{k=1}^{i-1} \prod_{k'=b,w} (-S_{k',k}) [S_{b,i}^x - i(-S_{k',i}^z)S_{b,i+1}^x] \quad (5.45)$$

$$B_i = \prod_{k'=b,w} (-S_{k',k})(S_{b,i}^x - i(-S_{k',i}^z)S_{b,i+1}^x). \quad (5.46)$$

Then, we obtain

$$b_{1,i} = B_i^\dagger + B_i = 2 \prod_{k=1}^{i-1} (-S_{k,k'}^z) S_{b,i}^x. \quad (5.47)$$

In a similar way, we find

$$w_{2,i} = W_i^\dagger + W_i = 2 \prod_{k=1}^{i-1} \prod_{k'=w,b} (-S_{k',k}^z)(-S_{b,i}^z)(-S_{w,i}^y). \quad (5.48)$$

Actually, Eqs. (5.47) and (5.48) are identical to Eqs. (5.39) and (5.40).

## 5.4 Phase diagram

In Fig. 5.10(a) we summarise the ground-state phase diagram as a function of  $\phi$  in a pie chart form. Notably, each phase has another exactly-symmetrically-placed phase in the pie chart, i.e, TLL and FM- $xy$ , Néel- $z$  and FM- $z$ , spiral- $xy$  and staggered- $xy$ . The paired phases have the common features. The TLL and FM- $xy$  states, where the exchange components are either all AFM or all FM, are basically understood within the framework of the isotropic Heisenberg chain; the FM- $xy$  state is long-range ordered and the TLL state is critical. The Néel- $z$  and FM- $z$  states are described by the easy-axis XXZ Heisenberg chain. The dominant features are determined by the Ising term. Depending on the sign of the Ising term, the spins are aligned ferromagnetically or antiferromagnetically along the  $z$  axis. The spiral- $xy$  and staggered- $xy$  states can be basically interpreted as the easy-plane XXZ Heisenberg chain affected by the double-spin-flip term. The system has a four-site periodicity, and exhibits a critical behaviour and a long-range ordering for the former and latter states, respectively, in analogy to the relation between the TLL and FM- $xy$  states.

It is now possible to establish a connection between our ground-state phase diagram and that of the two-dimensional KH model on a honeycomb lattice (Fig. 5.10(b), normalised to the current notation from [131]). To consider the phase-to-phase correspondence, it is helpful to regard the honeycomb lattice as coupled KH chains, as shown in Fig. 5.10(c). Here, the interchain coupling is equivalent to the  $z$ -bond in the honeycomb-lattice KH model, written as

$$\mathcal{H}_{z\text{-bond}} = \frac{J}{2} \sum_{k,l} (S_k^+ S_l^- + S_k^- S_l^+) + (J + K) \sum_{k,l} S_k^z S_l^z, \quad (5.49)$$

where  $k, l$  are summed over all connected sites between the KH chains.



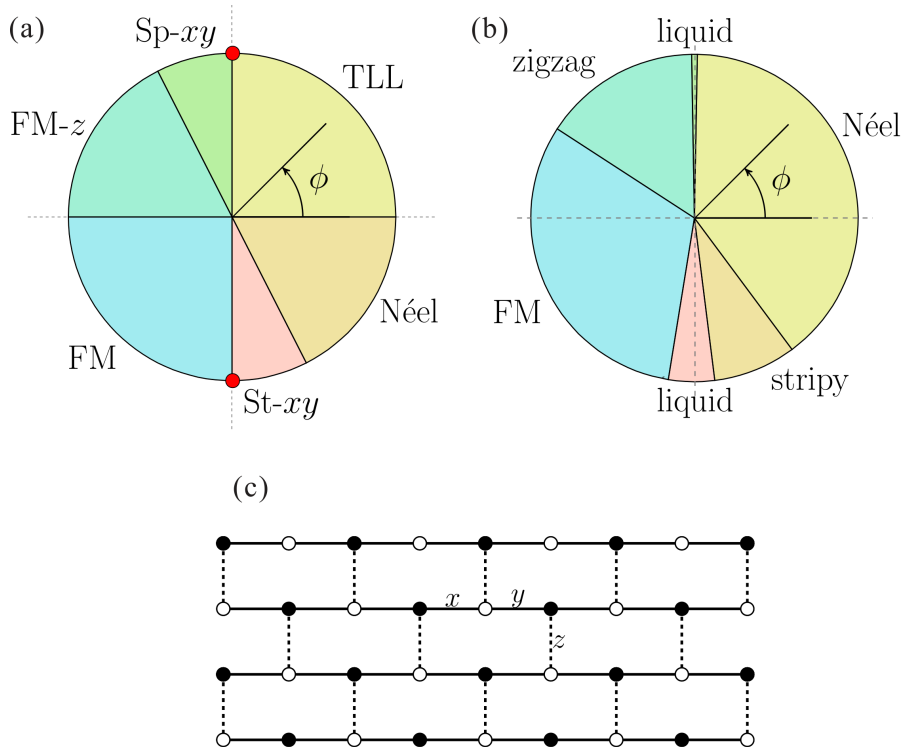


Figure 5.10: (a) Ground-state phase diagram of the 1D KH model. (b) Ground-state phase diagram of the honeycomb-lattice KH model, where the same notations as in Eq. (5.1) are used for  $K$  and  $J$ . (c) Brick-wall lattice created by coupling the 1D KH chains by the  $z$ -bond. This is topologically equivalent to the honeycomb lattice.

Hereafter, we report how the introduction of the  $z$ -bonds coupling affects the (quasi-)ordered states present in the one-dimensional case, mapping them to those of the honeycomb system:

(i) At  $0 \leq \phi < \frac{\pi}{2}$  the interchain coupling is AFM. Our TLL state has no long-range order but strong AFM fluctuations. Therefore, a Néel order is intuitively expected once the chains are antiferromagnetically coupled. Hence, our TLL phase corresponds to the Néel phase in the honeycomb case.

(ii) At  $0.65\pi \lesssim \phi < \pi$  our system is in the FM- $z$  state. While considering this interval, we need to examine two different cases as the sign of the interaction on the  $z$ -bonds changes from AFM to FM. We obtain a zigzag state in the honeycomb case when the FM- $z$  chain state is coupled by AFM interchain couplings; whereas a FM state in the case of FM interchain couplings. The change in sign of the interchain coupling is assumed to happen at  $\phi = \frac{3\pi}{4}$ , where  $J + K = 0$ . This  $\phi$  value is reasonably close to the transition point  $\phi \approx 0.81\pi$  between the zigzag and FM states in the honeycomb case. Thus, our FM- $z$  phase is distributed to either zigzag or FM phases of the honeycomb KH model depending on the AFM or FM nature on the  $z$ -bond.

(iii) At  $1.65\pi \lesssim \phi < 2\pi$  our system is in the Néel- $z$  state. In the same way as above, we need to consider the cases of AFM and FM  $z$ -bonds. We easily find that our Néel- $z$  state is base for the Néel and stripy states of the honeycomb KH model as also discussed in previous work [116]. Namely, our Néel- $z$  phase is distributed to either Néel phase

in the presence of AFM interchains coupling or the stripy phase in the presence of FM interchains coupling of the honeycomb KH model. The value of  $\phi = \frac{7\pi}{4}$  giving  $J + K = 0$  is again near the transition point  $\phi \approx 1.65\pi$  between the Néel and stripy states in the honeycomb case.

Therefore, it is possible to understand all the long-range ordered phases of the honeycomb-lattice KH model in the framework of the coupled KH chains. In brief, an extracted zigzag lattice line from any ordered state of the honeycomb-lattice KH model corresponds to one of the phases in the 1D KH chain; and the remaining degrees of freedom derive from the fact that the zigzag lines are coupled either ferromagnetically or antiferromagnetically by  $\mathcal{H}_{z\text{-bond}}$ .

(iv) Two  $xy$  phases in our phase diagram are left. Since these states are stabilised by the dominant  $xy$ -Kitaev term, they are connected to the Kitaev spin liquid states in the honeycomb case. In hindsight, this means that our staggered- $xy$  ordered state can collapse to the spin liquid state due to strong FM fluctuations along the  $z$ -direction.

## 5.5 Low-lying excitations

To examine the low-energy excitations for each phase, we calculated the dynamical spin structure factors  $S^{z,\pm}(q, \omega)$ , defined in Eq. (5.2). Under periodic boundary conditions the momentum is taken as  $q = \frac{4\pi}{L}n$  ( $n = 0, \pm 1, \dots, \pm \frac{L}{4}$ ) since the unit cell contains two lattice sites and the number of unit cells is  $\frac{L}{2}$  in a system with  $L$  sites. We study chains with  $L = 24$  using the Lanczos ED method and the results are shown only for  $q \geq 0$  as  $S^{z,\pm}(q, \omega) = S^{z,\pm}(-q, \omega)$ .

### 5.5.1 Tomonaga-Luttinger-liquid phase ( $0 \leq \phi < \pi/2$ )

As confirmed above, the low-energy physics at  $0 \leq \phi < \frac{\pi}{2}$  is described by a gapless TL model. The low-lying excitations are expected to be basically equivalent to those of the easy-plane XXZ chain because  $(2J + K)/2 > J > 0$  [see Eq. (5.2)]. If we ignore the double-spin-flip term  $\mathcal{H}_{\text{dsf}}$ , the main dispersion (lower bound of the spectrum) is given by

$$\omega(q) = \frac{\pi(2J + K)}{4} \frac{\sin \mu}{\mu} \sin \frac{q}{2} \quad (5.50)$$

with  $\cos \mu = (1 + \frac{K}{2J})^{-1}$ . This was obtained by using the transfer matrix of the six-vertex model [132, 133]. Nevertheless, the effect of  $\mathcal{H}_{\text{dsf}}$  is unknown. Therefore, to investigate the effect of  $\mathcal{H}_{\text{dsf}}$  we employ a standard SWT for the bipartite system. Using the Holstein-Primakoff representation the spin operators of  $\mathcal{H}_{\text{dsf}}$  for the black labelling sites in Fig. 5.1(d) are replaced as  $S_i^+ = \sqrt{2S - a_i^\dagger a_i} a_i$  and  $S_i^- = a_i^\dagger \sqrt{2S - a_i^\dagger a_i}$ ; similarly, for the white labelling sites  $S_i^+ = b_i^\dagger \sqrt{2S - b_i^\dagger b_i}$  and  $S_i^- = \sqrt{2S - b_i^\dagger b_i} b_i$ , where  $a_i$  and  $b_i$  are canonical boson annihilation operators at site  $i$ . Then, applying the Fourier transform we obtain

$$\mathcal{H}_{\text{dsf}} = i \frac{K}{2} \sum_q \sin \frac{q}{2} (a_{\frac{q}{2}}^\dagger b_{\frac{q}{2}} - a_{\frac{q}{2}} b_{\frac{q}{2}}^\dagger). \quad (5.51)$$

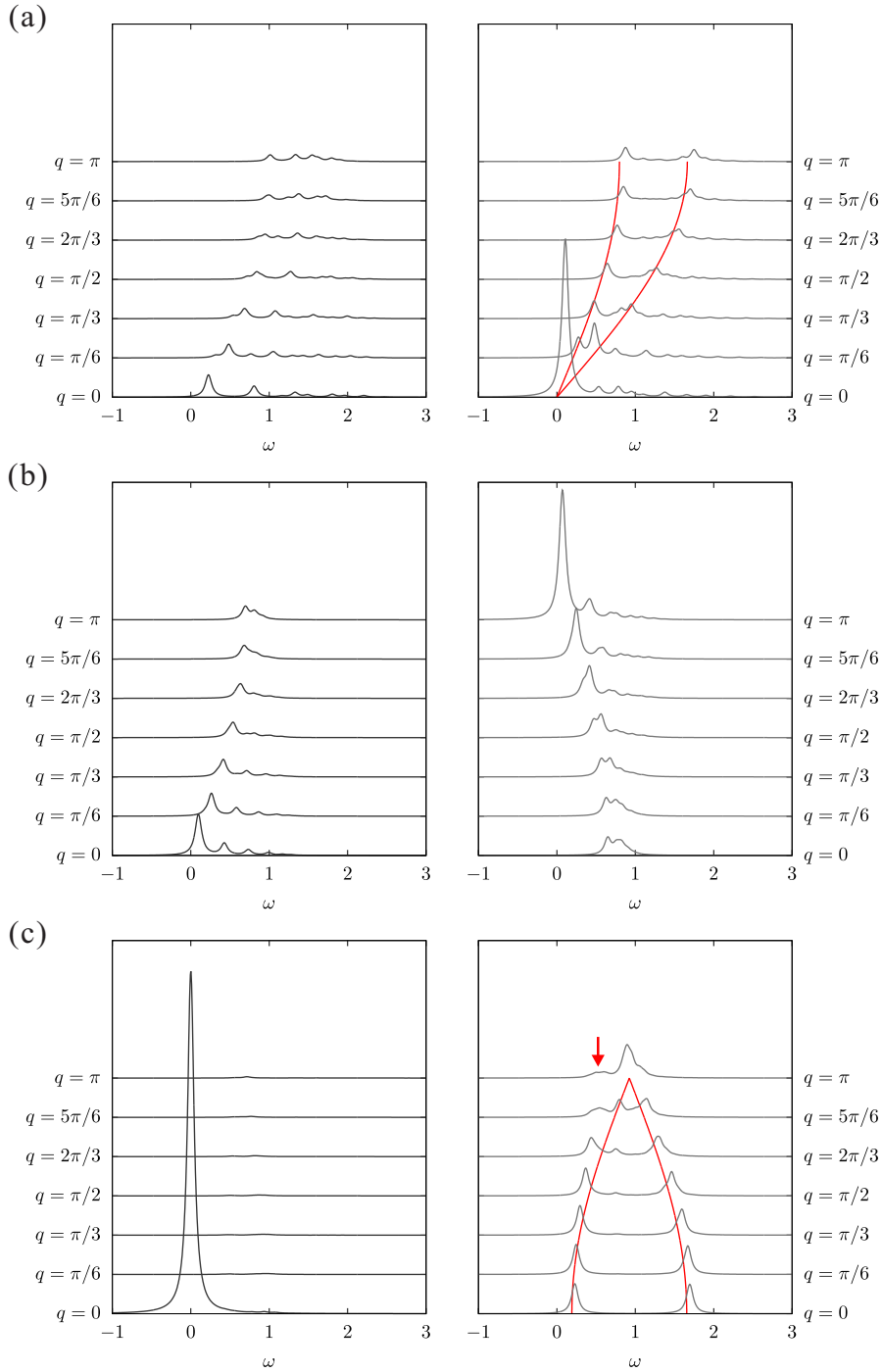


Figure 5.11: Dynamical structure factors calculated with a periodic 24-site chain for (a) TLL [ $\phi = \frac{\pi}{3}$ ], (b) spiral- $xy$  [ $\phi = \frac{5\pi}{8}$ ], and (c) FM- $z$  [ $\phi = \frac{7\pi}{8}$ ] states. The left and right panels show  $S^z(q, \omega)$  and  $S^-(q, \omega)$ , respectively. The red lines are analytical dispersions: Eq. (5.52) for  $\phi = \frac{\pi}{3}$  and Eq. (5.55) for  $\phi = \frac{7\pi}{8}$ . The arrow indicates an appearance of the spiral- $xy$  fluctuation in the FM- $z$  state.

This off-diagonal term gives a splitting in the main dispersion (5.50). Then, we can speculate the total dispersions as

$$\omega(q) = \left( \frac{\pi(2J + K)}{4} \frac{\sin \mu}{\mu} \pm \frac{K}{2} \right) \sin \frac{q}{2}. \quad (5.52)$$

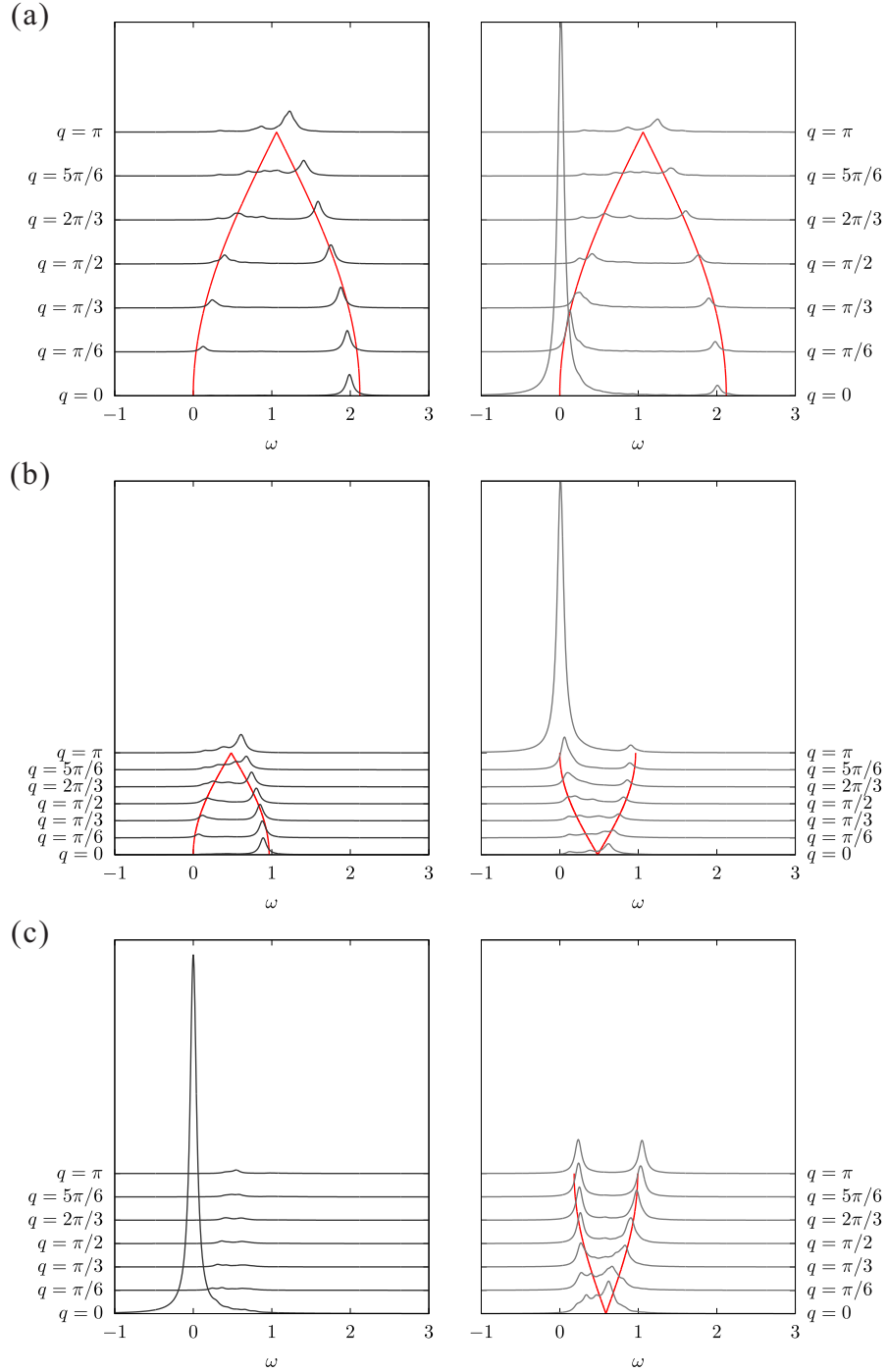


Figure 5.12: Dynamical structure factors calculated with a periodic 24-site chain for (a) FM- $xy$  [ $\phi = \frac{5\pi}{4}$ ], (b) staggered- $xy$  [ $\phi = \frac{19\pi}{12}$ ], and (c) Néel- $z$  [ $\phi = \frac{17\pi}{10}$ ] states. The left and right panels show  $S^z(q, \omega)$  and  $S^-(q, \omega)$ , respectively. The red lines are analytical dispersions: Eq. (5.56) for  $\phi = \frac{5\pi}{4}$ , Eq. (5.57) in  $S^z(q, \omega)$  and Eq. (5.58) in  $S^-(q, \omega)$  for  $\phi = \frac{19\pi}{12}$ , and Eq. (5.59) for  $\phi = \frac{17\pi}{10}$ .

Fig. 5.11(a) shows the dynamical structure factors  $S^z(q, \omega)$  and  $S^-(q, \omega)$  for  $\phi = \frac{\pi}{3}$ . The largest peak appears in  $S^-(q = 0, \omega = 0)$  reflecting the AFM fluctuations. The intensities in  $S^z(q, \omega)$  are weaker than those in  $S^-(q, \omega)$  due to the easy-plane  $xy$  anisotropy. The

split dispersions are well described by Eq. (5.52). The splitting is largest in the vicinity of the Kitaev point  $\phi = \frac{\pi}{2} - (J \rightarrow 0+, K \rightarrow 1)$ :

$$\omega(q) = \left( \frac{K}{2} \pm \frac{K}{2} \right) \sin \frac{q}{2}. \quad (5.53)$$

The main dispersion (lower bound of the spectrum) of the isotropic Heisenberg model at  $\phi = 0$  ( $K = 0$ ) is also reproduced by Eq. (5.52).

### 5.5.2 Spiral- $xy$ phase ( $\frac{\pi}{2} < \phi \lesssim 0.65\pi$ )

Across the Kitaev point from the TL to spiral- $xy$  phases the momentum of the Fermi point is shifted from  $q = \pi$  to  $q = 0$ . Thus, in the vicinity of the Kitaev point  $\phi = \frac{\pi}{2} + (J \rightarrow 0-, K \rightarrow 1)$ , the momentum of the excitation dispersion is shifted from Eq. (5.53) by  $\pi$ :

$$\omega(q) = \left( \frac{K}{2} \pm \frac{K}{2} \right) \left( 1 - \sin \frac{q}{2} \right) \quad (5.54)$$

for  $S^-(q, \omega)$ . In contrast,  $S^z(q, \omega)$  exhibits a  $q$ -independent continuum between  $\omega = 0$  and  $\omega = K$  since the  $z$ -component of exchange interaction is much smaller than the other interactions. With increasing  $\phi$  from  $\frac{\pi}{2}$ , the FM Ising interaction and double-spin-flip fluctuations increase and the exchange interaction decreases becoming zero at the critical boundary to the FM- $z$  phase. Fig. 5.11(b) shows the dynamical structure factors  $S^z(q, \omega)$  and  $S^-(q, \omega)$  for  $\phi = \frac{5}{8}\pi$ . The main dispersion in  $S^-(q, \omega)$  is scaled as  $\omega(q) \propto 1 - \sin \frac{q}{2}$ . Although the largest peak at  $(q, \omega) = (\pi, 0)$  indicates a four-site periodicity in the spiral- $xy$  state, it diminishes with increasing system size because of no long-range ordering. While in  $S^z(q, \omega)$ , a dispersion  $\omega(q) \propto \sin \frac{q}{2}$  appears and a peak toward the FM- $z$  state develops at  $(q, \omega) \approx (0, 0)$ . Both the dispersion widths are roughly scaled by  $|K|$ .

### 5.5.3 Ferromagnetic- $z$ phase ( $0.65\pi \lesssim \phi < \pi$ )

Fig. 5.11(c) shows the dynamical structure factors  $S^z(q, \omega)$  and  $S^-(q, \omega)$  for  $\phi = \frac{7}{8}\pi$ . Near  $\phi = \pi$  ( $K \approx 0$ ) in the FM- $z$  phase, the system is effectively described by a FM XXZ Heisenberg chain with easy-axis anisotropy  $J < \frac{2J+K}{2} < 0$  and the ground state is approximately expressed by Eq. (5.5). An applied operator  $S_q^z$  does not change the ground state  $|\psi_0\rangle$  in Eq. (5.2) and the final state  $|\psi_\nu\rangle$  has only a zero energy excitation from  $|\psi_0\rangle$ . Therefore,  $S^z(q, \omega)$  has a very sharp peak at  $(q, \omega) = (0, 0)$  and almost no spectral weight appears at the other momenta. This peak keeps its weight constant with increasing system length, indicating the long-range FM- $z$  ordering. On the other hand, in Eq. (5.2) the operator  $S_q^-$  dopes one magnon into the FM- $z$  alignment so that the SWT is expected to give a good approximation for the excitation dispersion of  $S^-(q, \omega)$ :

$$\omega(q) = -J \pm \frac{2J+K}{2} \cos \frac{q}{2}. \quad (5.55)$$

We can confirm that a gap  $\Delta = \frac{K}{2}$  opens at  $q = 0$  reflecting the easy-axis anisotropy. With approaching the neighbouring spiral- $xy$  phase, the double-spin-flip fluctuations grow gradually in influence; accordingly, the  $q = 0$  peak in  $S^z(q, \omega)$  shrinks and a peak develops at  $q = \pi, \omega \approx 0$  in  $S^-(q, \omega)$ .

### 5.5.4 Ferromagnetic- $xy$ phase ( $\pi < \phi < \frac{3\pi}{2}$ )

Fig. 5.12(a) shows the dynamical structure factors  $S^z(q, \omega)$  and  $S^-(q, \omega)$  for  $\phi = \frac{5}{4}\pi$ . Near  $\phi = \pi$  ( $K \approx 0$ ) in the FM- $xy$  phase, the system is effectively described by a FM XXZ Heisenberg chain with easy-plane anisotropy  $\frac{2J+K}{2} < J < 0$  and the ground state is approximately expressed by Eq. (5.4). Thus, the excitation spectrum is expected to be gapless. Since the total  $S^z$  of the ground state is zero, unlike the case of FM- $z$  state both  $S^z(q, \omega)$  and  $S^-(q, \omega)$  have the same excitation dispersion as

$$\omega(q) = -\frac{2J+K}{2} \left(1 \pm \cos \frac{q}{2}\right). \quad (5.56)$$

Note that a sharp peak at  $(q, \omega) = (0, 0)$  in  $S^-(q, \omega)$  keeps its weight constant with increasing system length, indicating the FM- $xy$  long-range ordering. On the other hand, in the vicinity of the Kitaev point  $\phi \approx \frac{3\pi}{2}-$ , the excitation dispersion of  $S^-(q, \omega)$  is well described by Eq. (5.53).

### 5.5.5 Staggered- $xy$ ordered phase ( $\frac{3\pi}{2} < \phi \lesssim 1.65\pi$ )

In the vicinity of the Kitaev point  $\phi = \frac{3}{2}\pi+$ , the excitation spectra are the same as in the other Kitaev point  $\phi = \frac{1}{2}\pi+$ , namely, Eq. (5.54) for  $S^-(q, \omega)$  and a  $q$ -independent continuum for  $S^z(q, \omega)$ . Whereas in the vicinity of the Néel- $z$  ordered phase  $\phi = \tan^{-1}(-2)-$ , the ground state is expressed by Eq. (5.11). Thus, the dispersions are described by a single magnon excitation:

$$\omega(q) = -\frac{K}{2} \left(1 \pm \cos \frac{q}{2}\right) \quad (5.57)$$

for  $S^z(q, \omega)$ , and

$$\omega(q) = -\frac{K}{2} \left(1 \pm \sin \frac{q}{2}\right) \quad (5.58)$$

for  $S^-(q, \omega)$ . Fig. 5.12(b) shows the dynamical structure factors  $S^z(q, \omega)$  and  $S^-(q, \omega)$  for  $\phi = \frac{19\pi}{12}$ . The excitation dispersions are well reproduced by Eqs. (5.57) and (5.58). We also find a sharp peak at  $(q, \omega) = (\pi, 0)$  in  $S_-(q, \omega)$ , which indicates the staggered- $xy$  long-range ordering. This peak keeps its weight constant with increasing the system length, in contrast to the similar peak for the spiral- $xy$  state.

### 5.5.6 Néel- $z$ ordered phase ( $1.65\pi \lesssim \phi < 2\pi$ )

In the vicinity of the staggered- $xy$  ordered phase  $\phi = \tan^{-1}(-2)+$ , the ground state is expressed by Eq. (5.12). Accordingly,  $S^z(q, \omega)$  has only a delta peak at  $(q, \omega) = (0, 0)$ . Whereas,  $S^-(q, \omega)$  is exactly explained by a single magnon dispersion. It is obtained by the SWT as

$$\omega(q) = J \pm \frac{K}{2} \sin \frac{q}{2}. \quad (5.59)$$

Although this is equivalent to Eq. (5.57), the spectral weight is uniform for all  $q$  values. Since the transition at  $\phi = \tan^{-1}(-2)$  is first ordered, there is no peak indicating a connection to the staggered- $xy$  ordered phase. On the other hand, near  $\phi = 2\pi$ , the system can be basically regarded as an easy-axis AFM XXZ Heisenberg chain so that the excitation dispersion is described by Eq. (5.52) for both  $S^z(q, \omega)$  and  $S^-(q, \omega)$ . Fig. 5.12(c)

shows the dynamical structure factors  $S^z(q, \omega)$  and  $S^-(q, \omega)$  for the intermediate region  $\phi = \frac{17}{10}\pi$ . The main dispersion of  $S^-(q, \omega)$  is basically described by Eq. (5.59) but some features from Eq. (5.52) seem to be somewhat mixed.

## 5.6 Discussion

In this chapter, we have established the presence of a variety of phases in the 1D KH system. Especially, it is surprising that most of the  $\phi$  ranges are covered by long-range ordered phases despite considering a pure 1D system. In this context, we now consider the K-intercalated  $\alpha$ -RuCl<sub>3</sub>, namely, K<sub>0.5</sub>RuCl<sub>3</sub>. One should be aware of the fact that several different parameter sets have been suggested for undoped  $\alpha$ -RuCl<sub>3</sub>: (i)  $K = -5.6$ ,  $J = 1.2$  ( $\phi \approx 1.57\pi$ ) [134], (ii)  $K = 7.0$ ,  $J = 4.6$  ( $\phi \approx 0.68\pi$ ) [102], (iii)  $K = 8.1$ ,  $J = 2.9$  ( $\phi \approx 0.61\pi$ ) [102], (iv)  $K = -6.8$ ,  $J = 0$  ( $\phi = 1.5\pi$ ) [135] in unit of meV. If we assume that the charge ordering pattern in K<sub>0.5</sub>RuCl<sub>3</sub> is that illustrated in Fig. 5.1(c), the parameter sets (i)-(iv) correspond to the staggered- $xy$ , FM- $z$ , spiral- $xy$ , and FM Kitaev point, respectively. In practice, the charge ordering could cause a significant change of the parameter since they are very sensitive to the Ru-Cl-Ru bond angle [134]. In other words, once the magnetic properties of K<sub>0.5</sub>RuCl<sub>3</sub> are observed, we may easily speculate the possible parameter set of K<sub>0.5</sub>RuCl<sub>3</sub> and even the charge ordering pattern by comparing them to our rich phase diagram. To gain deeper insights, theoretical and experimental studies under magnetic fields are also required.

It is relevant to seek other possible realisations of 1D KH system. Even if the Kitaev interaction in 1D systems is present, it is considered to be very small. However, as shown above, even a tiny Kitaev interaction can stabilise one of ordered state. It might also be intriguing to reconsider quasi-1D materials having two sublattices like Ni<sub>2</sub>(EDTA)(H<sub>2</sub>O)<sub>4</sub>, [Ni(f-rac-L)(CN)<sub>2</sub>], LiCuSbO<sub>4</sub>, and Rb<sub>2</sub>Cu<sub>2</sub>Mo<sub>3</sub>O<sub>12</sub> from the point of view of the 1D Kitaev system.

The  $\phi$ -dependent phase diagram of our model is similar to that for the honeycomb-lattice KH model. Remarkably, all the magnetically ordered states of the honeycomb-lattice KH model can be interpreted in terms of the coupled 1D KH chains. In other words, the key elements to derive the magnetic ordering in the 2D honeycomb-lattice KH model are already contained in the 1D KH chain. The pure 1D model, however, does not support the existence of a KSL state. Therefore, we turn to a quasi-1D system and consider a ladder geometry in the next chapter.





# 6 Kitaev-Heisenberg ladder

In the previous chapter, we have studied the KH model on a 1D chain and found a very rich phase diagram with several long-range ordered states. Nonetheless, that system did not show the presence of a KSL due to the missing  $z$  rung. Hence, we now turn to a more promising geometry for the existence of such an exotic state, though still keeping the system quasi-one-dimensional, and consider a two-legged ladder. In fact, in this chapter, we will show how such a quasi-1D system presents a phase diagram very similar to that of the 2D honeycomb model, including to QSL states.

This chapter is organised as follows: Our Hamiltonian of the KH ladder is explained and the applied numerical methods are described in Sec. 6.2. In Sec. 6.3 we present the four kinds of LRO magnetic state that are present depending on the ratio between Kitaev and Heisenberg interactions. In Sec. 6.4 we discuss the properties of KSL states expanded around the large limit of Kitaev interaction. In Sec. 6.5 the ground states are summarised as a phase diagram as a function of the ratio between Kitaev and Heisenberg interactions. We also compare the ground state phase diagram with those of 1D KH model and 2D honeycomb-lattice KH model, and discuss the similarity and dissimilarity among them. Section 6.6 explains the fundamental features of dynamical spin structure factor in each the phase. Finally we discuss our findings in Sec. 6.7.

## 6.1 Introduction

While in the previous chapter we have studied the KH model on a 1D chain (Fig. 6.1(a)), we now consider a quasi-1D system that acts as an “intermediate” geometry between a pure 1D chain and a 2D lattice, namely, a two-legged ladder. The lattice is shown in Fig. 6.1(b). In fact, though the original KSL was introduced on the honeycomb lattice, it is known that the Kitaev interaction on any three-coordinated lattice gives rise to non trivial properties: In this sense, while a one-dimensional (1D) KH chain represented in Fig. 6.1(a) cannot possess a KSL state (see Chapter 5), the KH model on a ladder (we simply refer to it as the KH ladder hereafter) in Fig. 6.1(b) already meets the geometrical requirement due to the presence of the  $z$  bonds. The KH ladder can be also extracted from a brick-wall lattice (Fig. 6.1(c)), which is geometrically equivalent to the honeycomb lattice: Cutting along the grey line and folding the cut  $z$  bonds towards the centre we recover the KH ladder in Fig. 6.1(b). Hence, we expect to gain insight about the basic properties of the honeycomb-lattice KH model from the KH ladder.

Since the interplay of Kitaev and Heisenberg interactions in 2D or 3D geometries may pose serious challenges to the available numerical methods, it is a good strategy to consider the ladder system next. We can make use of the DMRG technique to study quasi-1D systems with great accuracy [21]. Moreover, possible spin liquid behaviour in the KH ladder has been already suggested at finite temperature [136].

We obtain the ground state phase diagram of the KH ladder to be composed of

---

Parts of this chapter have been published as Phys. Rev. B **99**, 224418 2019

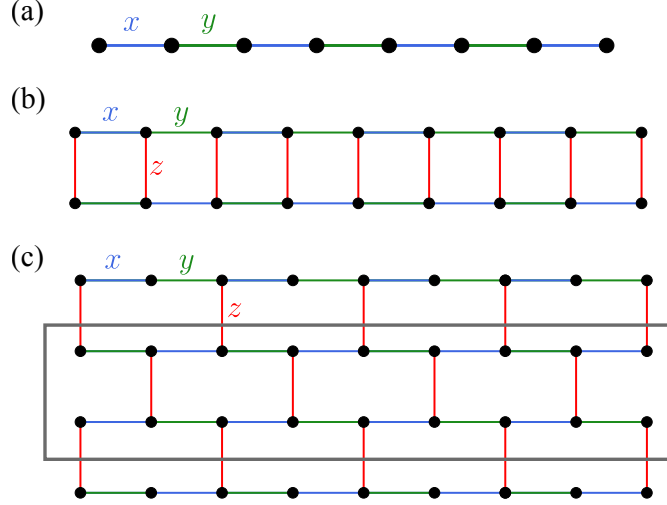


Figure 6.1: (a) Lattice structure of the KH chain. (b) Lattice structure of the KH ladder studied in this chapter. (c) Structure of the KH model on a brickwall lattice, which is geometrically equivalent to the honeycomb lattice. The grey rectangle shows a cutout that makes the mapping to the ladder represented in (b) possible. The indices  $x$ ,  $y$  and  $z$  indicate the three different bonds:  $x$  bond,  $y$  bond, and  $z$  bond, respectively.

four magnetically ordered phases, namely rung singlet, stripy, FM- $xy$ , zigzag; and two liquid phases, namely AFM SL and FM SL, depending on the ratio between Kitaev and Heisenberg interactions. To determine the phase boundaries, we compute several order parameters, excitation gap, and entanglement spectra. Strikingly, the phase diagram of the KH ladder is very similar to that of the honeycomb-lattice KH model. We then proceed at analyzing the low-lying excitations of the KH ladder by calculating the dynamical spin structure factor with using the Lanczos (ED). It is interesting that most of the spectral features can be explained by considering those of the 1D KH model Sec. 5.5.

## 6.2 Model and Method

### 6.2.1 Model

We study the KH ladder as represented in Fig. 6.1(b). The Hamiltonian is described by

$$\begin{aligned}
 \mathcal{H} = & K \sum_{i=1}^{L/2} (S_{2i-1,1}^x S_{2i,1}^x + S_{2i,1}^y S_{2i+1,1}^y) + J \sum_{i=1}^L \mathbf{S}_{i,1} \cdot \mathbf{S}_{i+1,1} \\
 & + K \sum_{i=1}^{L/2} (S_{2i,2}^x S_{2i+1,2}^x + S_{2i-1,2}^y S_{2i,2}^y) + J \sum_{i=1}^L \mathbf{S}_{i,2} \cdot \mathbf{S}_{i+1,2} \\
 & + K \sum_{i=1}^L S_{i,1}^z S_{i,2}^z + J \sum_{i=1}^L \mathbf{S}_{i,1} \cdot \mathbf{S}_{i,2},
 \end{aligned} \tag{6.1}$$

where  $S_{i,j}^\alpha$  is the  $\alpha$  component of spin- $\frac{1}{2}$  operator  $\mathbf{S}_{i,j}$  at rung  $i$  and leg  $j$  ( $= 1, 2$ ),  $L$  is the system length, and  $K$  and  $J$  are the Kitaev and Heisenberg interactions, respectively. The first two lines denote the intraleg interactions and the last line denotes the interleg

interactions: Each leg has a period of two lattice spacing and there are three kinds of bond-dependent interactions. As shown in Fig. 6.1(c) one finds that the KH ladder (6.1) is a system cut out of the KH model on a brick-wall lattice. Since the brick-wall-lattice KH model is obtained by deforming the honeycomb-lattice KH model, the KH ladder is geometrically equivalent to the honeycomb-lattice KH model. Note that the KH ladder has a strong cluster anisotropy, i.e., the periodicity along the  $z$  bond is short. Nonetheless, the LRO states observed in the honeycomb-lattice KH model also have a short periodicity in the bond direction and all of them can be reproduced in the KH ladder as shown below. In this work, to compare magnetic properties of the KH ladder to those of the honeycomb-lattice KH model, we focus on the case of equal Kitaev and Heisenberg terms on the three bonds. For convenience, we introduce an angle parameter  $\phi$ , setting  $J = \cos \phi$  and  $K = \sin \phi$ .

The Hamiltonian (6.1) can be rewritten as

$$\begin{aligned} \mathcal{H}_{\text{leg}} = & \frac{2J + K}{4} \sum_{j=1}^2 \sum_{i=1}^L (S_{i,j}^+ S_{i+1,j}^- + S_{i,j}^- S_{i+1,j}^+) \\ & + \frac{K}{4} \sum_{j=1}^2 \sum_{i=1}^L (-1)^{(i+j)} (S_{i,j}^+ S_{i+1,j}^+ + S_{i,j}^- S_{i+1,j}^-) \\ & + J \sum_{j=1}^2 \sum_{i=1}^L S_{i,j}^z S_{i+1,j}^z, \end{aligned} \quad (6.2)$$

for the intraleg couplings, and

$$\mathcal{H}_{\text{rung}} = \frac{J}{2} \sum_{i=1}^L (S_{i,1}^+ S_{i,2}^- + S_{i,1}^- S_{i,2}^+) + (J + K) \sum_{i=1}^L S_{i,1}^z S_{i,2}^z \quad (6.3)$$

for the interleg, i.e., rung, couplings. We can easily notice that all the nearest-neighbor bonds have a  $XXZ$ -type interaction, and the sign-alternating double-spin-flip fluctuations acts only along the leg direction.

### 6.2.2 Method

We study finite-size systems with length up to  $L \times 2 = 160 \times 2$  with keeping up to  $m = 4000$  density-matrix eigenstates in the renormalisation procedure. In this way, the truncation error, i.e. the discarded weight, is  $\sim 10^{-11}$ . The calculated quantities are extrapolated to the limit  $m \rightarrow \infty$  if needed. This allows us to perform very accurate finite-size scaling analysis. We use open and periodic boundary conditions depending on the quantity we consider. To identify the ground state for the given angle parameter  $\phi$ , we compute several order parameters, spin gap, plaquette operator, dynamical spin structure factor, and entanglement spectra. When we calculate the order parameter under open boundary conditions, the LRO state is observed as a state with a broken translational or spin symmetry. There are in fact several degenerate ground states; one configuration of the degenerate states is selected as the ground state by the initial condition of the DMRG calculation.

For the dynamical calculations, we use the Lanczos ED method. To examine the low-energy excitations for each phase, we calculate the dynamical spin structure factor, defined as

$$\begin{aligned} S_\gamma(q, \omega) &= \frac{1}{\pi} \text{Im} \langle \psi_0 | (S_q^\gamma)^\dagger \frac{1}{\hat{H} + \omega - E_0 - i\eta} S_q^\gamma | \psi_0 \rangle \\ &= \sum_\nu |\langle \psi_\nu | S_q^\gamma | \psi_0 \rangle|^2 \delta(\omega - E_\nu + E_0), \end{aligned} \quad (6.4)$$

where  $\gamma$  is  $z$  or  $-$ (+),  $|\psi_\nu\rangle$  and  $E_\nu$  are the  $\nu$ -th eigenstate and the eigenenergy of the system, respectively ( $\nu = 0$  corresponds to the ground state). Under periodic boundary conditions, the spin operators  $S_q^\gamma$  can be precisely defined by

$$S_q^\gamma = \sqrt{\frac{2}{L}} \sum_i S_{i,j}^\gamma \exp(iqr_{i,j}), \quad (6.5)$$

where  $r_{i,j}$  is the position of site  $(i, j)$ . The sum runs over either  $i$  even or  $i$  odd sites with fixing  $j = 1$  or  $2$ . They provide the same results. The momentum is taken as  $q = \frac{4\pi}{L}n$  ( $n = 0, \pm 1, \dots, \pm \frac{L}{4}$ ) since the lattice unit cell includes four sites and the number of unit cells is  $\frac{L}{2}$  in a system with  $L \times 2$  sites. We calculate both spectral functions  $S_\pm(q, \omega)$  and  $S_z(q, \omega)$  as they are different due to broken SU(2) symmetry except at  $\phi = 0$  and  $\pi$ . We study ladders with  $L \times 2 = 12 \times 2$ , namely, six unit cells, by the Lanczos ED method. As shown below, our model (6.1) contains only commensurate phases with the unit cell containing one, two, or four sites. Therefore, a quantitative discussion for the low-lying excitations is possible even within the  $12 \times 2$  ladder.

### 6.3 Ordered phases

In this section, we present the DMRG results for LRO phases in the ground state. We find four kinds of ordering, namely: stripy, rung singlet, zigzag, and FM- $xy$  phases. The rung-singlet state is not magnetically ordered but the system is in a unique state with dimer ordering, namely, the dimer-dimer correlation is long ranged. The names of the ordered phases follow Ref. [98]. In the LRO states, except for the rung-singlet state, the translational or spin rotation symmetry is broken in a finite system due to Friedel oscillations under open boundary conditions, so that the ordered state can be directly observed with a local quantity by extracting one of the degenerate states. Generally, the Friedel oscillations in the centre of the system decay as a function of the system length. If the amplitude at the centre of the system persists for arbitrary system lengths, it corresponds to a long-range ordering.

#### 6.3.1 Stripy phase ( $1.57\pi < \phi < 1.7\pi$ )

Let us start with the stripy state. In the region of  $\frac{3}{2}\pi \lesssim \phi < \frac{7}{4}\pi$ , since  $J > 0$  and  $J + K < 0$ , the leg and rung interactions are AFM and FM, respectively. Thus, we naively expect the coupled chains to order in what we call the stripy state, as depicted in Fig. 6.2(a). Getting back to the original brick-wall lattice, the alignments of up spins and down spins appear alternately with running along the leg. This state can be analytically

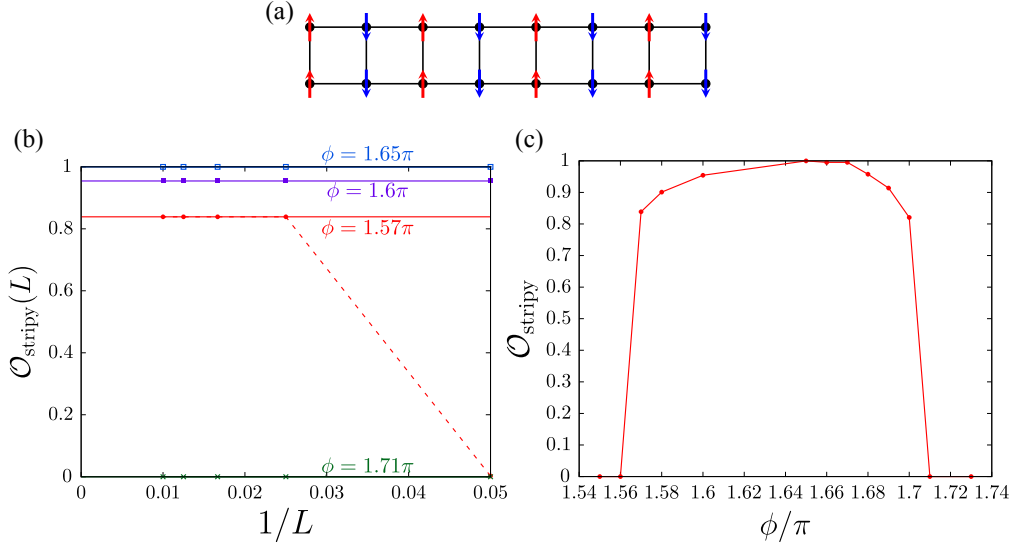


Figure 6.2: (a) Schematic spin configuration of the stripy state. (b) Finite-size scaling of the stripy order parameter for several values of  $\phi$ . The dotted line helps the eye follow the data points, solid lines represent the linear fitting. (c) Extrapolated stripy order parameter as a function of  $\phi/\pi$ .

proven at  $\phi = \tan^{-1}(-2) \approx 1.65\pi$ , where our model (6.1) is exactly solvable: The rung Hamiltonian (6.3) leads simply to isotropic FM couplings due to  $J + K = -J$ , whereas, the leg Hamiltonian (6.2) is reduced to a sum of double-spin-flip ( $S^+S^+ + S^-S^-$ ) and Ising ( $S^zS^z$ ) parts because the exchange ( $S^+S^- + S^-S^+$ ) term disappears due to  $2J + K = 0$ . The total energy of our system (6.1) is minimised by taking the wave function as

$$|\Psi_0\rangle = \frac{1}{\sqrt{2}} \left[ \prod_{i=1}^{L/2} S_{2i,1}^- S_{2i,2}^- |\uparrow\uparrow\rangle + \prod_{i=1}^{L/2} S_{2i,1}^+ S_{2i,2}^+ |\downarrow\downarrow\rangle \right], \quad (6.6)$$

where  $|\uparrow\uparrow\rangle$  and  $|\downarrow\downarrow\rangle$  denote configurations including only up and down spins, respectively. Note that all the spins are aligned along the  $z$  direction. When the Hamiltonian (6.1) is applied to this wave function (6.6), only the Ising terms provide nonzero components. Thus, no quantum fluctuations exist and the system is in a perfect stripy state described by Eq. (6.6). The ground-state energy is  $E_0/L = \frac{3}{4}J$ .

It is still a nontrivial question how the wave function (6.6) is modified with moving away from  $\phi \approx 1.65\pi$ . To study it numerically, we introduce an order parameter defined by

$$\mathcal{O}_{\text{stripy}}(L) = \frac{1}{2} \left( |\langle S_{(L/2,1)}^z \rangle - \langle S_{(L/2+1,1)}^z \rangle + \langle S_{(L/2,2)}^z \rangle - \langle S_{(L/2+1,2)}^z \rangle| \right) \quad (6.7)$$

$$\mathcal{O}_{\text{stripy}} = \lim_{L \rightarrow \infty} \mathcal{O}_{\text{stripy}}(L) \quad (6.8)$$

In Fig. 6.2(b), we show finite-size scaling analysis of  $\mathcal{O}_{\text{stripy}}$ . We see how finite-size scaling is of fundamental importance in this system: the dotted line shows the jump in the order parameter between the smallest ( $20 \times 2$ ) and the second smallest ( $40 \times 2$ ) systems. The finite size scaling is then performed with discarding the first point, where the system

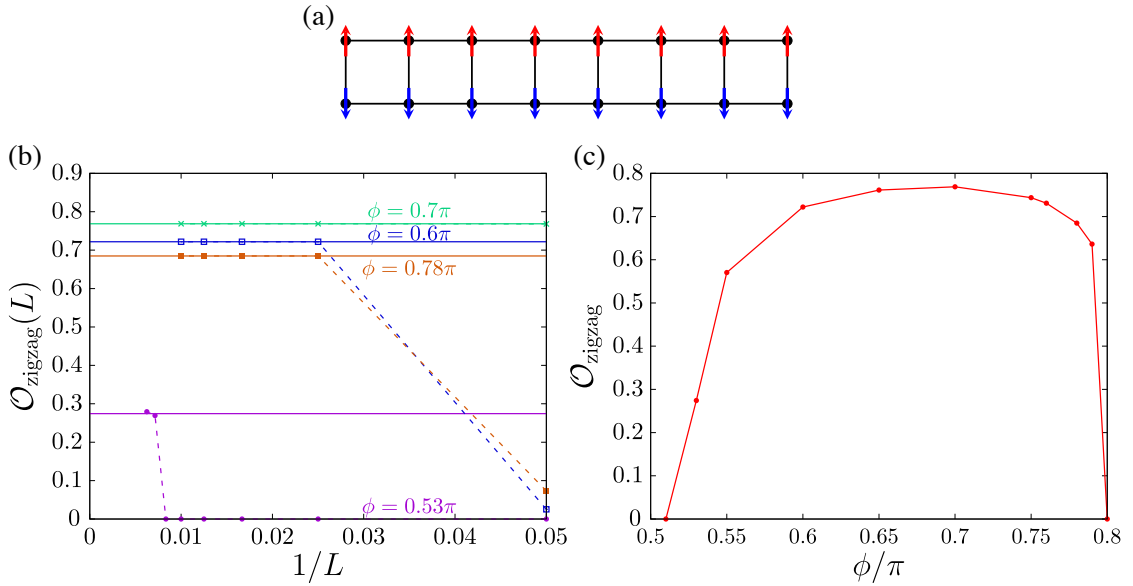


Figure 6.3: (a) Schematic spin configuration of the zigzag state. (b) Finite size scaling of the zigzag order parameter for several values of  $\phi$ . Dotted lines help the eye follow the data points, solid lines represent the linear fitting. Note that for  $\phi = 0.53\pi$  the order parameter is finite only for  $L \geq 140$ . (c) Extrapolated zigzag order parameters as a function of  $\phi/\pi$ .

size is too small to stabilise the ordering. This explicitly indicates the existence of a “critical length” for stabilising a long range order. Examples of this kind of behaviour are seen also for order parameters of the other ordered states. The  $L \rightarrow \infty$  extrapolated value of the stripy order parameter is plotted in Fig. 6.2(c). The validity of the exact wave function (6.6) is confirmed by  $\mathcal{O}_{\text{stripy}} = 1$  at  $\phi \approx 1.65\pi$ . Even away from  $\phi \approx 1.65\pi$ ,  $\mathcal{O}_{\text{stripy}}$  keeps relatively large value ( $\sim 1$ ) and drops down to zero at both edges,  $\phi \approx 1.57\pi$  and  $\phi = 1.7\pi$ . It means that the transitions at both phase boundaries are of the first order.

In the previous Chapter (Sec. 5.3.5) we found that the 1D KH model exhibits a Néel- $z$  state, i.e., Néel ordering with spins parallel or antiparallel to the  $z$  axis, for  $1.65\pi \lesssim \phi < 2\pi$ . In this sense the stripy state of the KH ladder may be also interpreted as two Néel- $z$  chains coupled by FM interaction.

### 6.3.2 Zigzag phase ( $0.53\pi \leq \phi < 0.8\pi$ )

In the region of  $\frac{1}{2}\pi \lesssim \phi < \frac{3}{4}\pi$ , since  $J < 0$  and  $J + K > 0$ , the leg and rung interactions are FM and AFM, respectively. Hence, an ordered state as in Fig. 6.3(a) is expected. We call it a *zigzag* state by following the name of the corresponding state in the honeycomb-lattice KH model [98] (our *straight* leg corresponds to a zigzag line in the honeycomb lattice). Through a similar analysis of the exact wave function (6.6) at  $\phi \approx 1.65\pi$ , we could assume the wave function at  $\phi \approx 0.65\pi$  to be

$$|\Psi_0\rangle \approx \frac{1}{\sqrt{2}} \left[ \prod_{i=1}^L S_{i,1}^- |\uparrow\rangle + \prod_{i=1}^L S_{i,1}^+ |\downarrow\rangle \right]. \quad (6.9)$$

However, unlike in the case of  $\phi \approx 1.65\pi$ , this *classical* configuration is just a good approximation for the wave function at  $\phi \approx 0.65\pi$  but not an exact one because quantum fluctuations are involved from the intra-leg double-spin-flip and rung exchange processes.

We define the following order parameter to see the instability of zigzag ordering:

$$\mathcal{O}_{\text{zigzag}}(L) = \frac{1}{2} \left( |\langle S_{(L/2,1)}^z \rangle + \langle S_{(L/2+1,1)}^z \rangle - \langle S_{(L/2,2)}^z \rangle - \langle S_{(L/2+1,2)}^z \rangle| \right) \quad (6.10)$$

$$\mathcal{O}_{\text{zigzag}} = \lim_{L \rightarrow \infty} \mathcal{O}_{\text{zigzag}}(L) \quad (6.11)$$

Figures 6.3(b) and 6.3(c) show the finite-size scaling analysis of  $\mathcal{O}_{\text{zigzag}}(L)$  for several values of  $\phi$ . At the lower boundary with the AFM KSL phase ( $\phi = 0.53\pi$ ), the long-range order settles only at large system sizes  $L \geq 140$ : This can be interpreted as some kind of “fragility” of the zigzag ordering close to the AFM KSL. Moreover, it underlines the importance of studying large enough ladders using the DMRG method for this system, although the finite-size effect could be relieved by a pinning of the order with the corresponding magnetic field at the system edges. In Fig. 6.3(c) we plot the extrapolated values of  $\mathcal{O}_{\text{zigzag}}$  in the thermodynamic limit. We can see that  $\mathcal{O}_{\text{zigzag}}$  keeps  $\sim 0.7$ – $0.8$  in most of the zigzag phase and Eq. (6.9) gives a good approximation for this zigzag state. Around the lower phase boundary ( $\phi \sim 0.53\pi$ ),  $\mathcal{O}_{\text{zigzag}}$  approaches rather continuously to zero with approaching the phase boundary, suggesting a continuous transition of second order; whereas at the upper phase boundary ( $\phi \sim 0.8\pi$ ),  $\mathcal{O}_{\text{zigzag}}$  drops down to 0, suggesting a first-order transition.

For  $\phi < 0.75\pi$ , the leading interaction on the rungs is AFM since  $J + K$  is positive in Eq. (6.3). Therefore, the zigzag state may be simply interpreted as antiferromagnetically coupled FM chains (“FM- $z$  state” Sec. 5.3.3) obtained in the 1D KH model at  $0.65\pi < \phi < \pi$ . However, the lower bound of the zigzag phase is significantly more extended (down to  $\phi = 0.53\pi$ ) than the lower bound of the FM- $z$  state ( $\phi = 0.65\pi$ ) in the 1D KH model. At  $0.5\pi < \phi < 0.65\pi$  the 1D KH model is in a liquid state called “spiral- $xy$  state” (Sec. 5.3.4). Nevertheless, ferromagnetic fluctuations on the legs would be strong because of the negative  $J$  in Eq. (6.2) and the zigzag ordering can be stabilised by the dominant AFM Ising term on the rungs due to  $J + K > |J|$  in Eq. (6.3). In other words, the FM alignment on each leg is just taken care of by the interchain AFM couplings. This may be related to the fragility of the zigzag order near the AFM KSL phase.

### 6.3.3 Rung-singlet phase ( $-0.3\pi \leq \phi \leq 0.48\pi$ )

At  $\phi = 0$  ( $J = 1, K = 0$ ), our system (6.1) is a pure isotropic AFM Heisenberg ladder, known to be in a rung-singlet state with singlet-triplet excitation gap  $\Delta_1 = 0.5037J$  (Ref. [137]). The schematic picture of a rung-singlet state is given in Fig. 6.4(a). We compute the excitation gap to see how the perturbation introduced by the Kitaev term affects this state. Since the total  $S^z$  is not a good quantum number except at  $\phi = 0$ , the rung-singlet excitation gap is simply defined as the energy difference between the ground state and first excited state. The gap between the ground state and  $n$ th excited state is defined as

$$\Delta_n(L) = E_n(L) - E_0(L) \quad \Delta_n = \lim_{L \rightarrow \infty} \Delta_n(L), \quad (6.12)$$

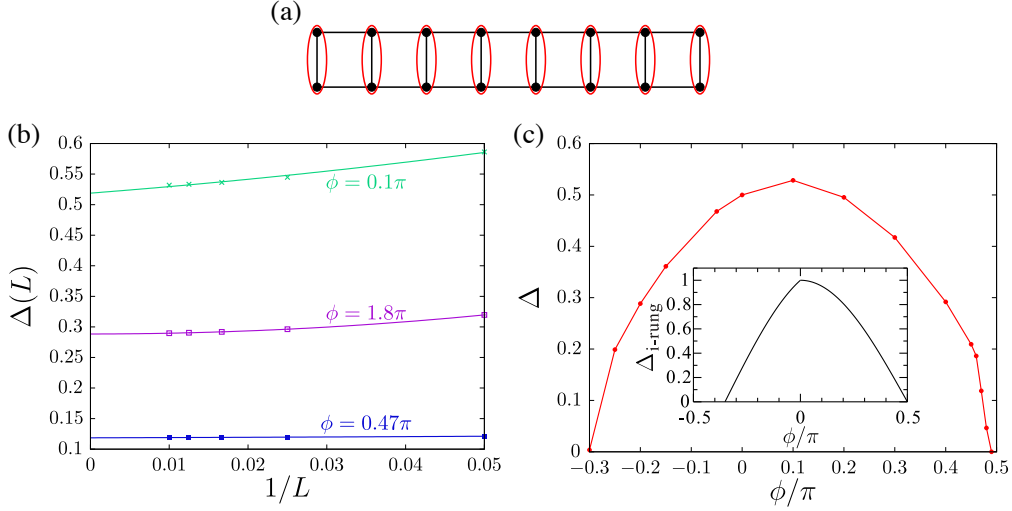


Figure 6.4: (a) Schematic spin configuration of the rung singlet state, where a red ellipse represents a spin singlet. (b) Finite size scaling of the gap for  $\phi = -0.2\pi, 0.1\pi$ , and  $0.47\pi$ . The fit is performed using a polynomial function in  $1/L$ . (c) Extrapolated spin gap as a function of  $\phi/\pi$ . Inset: Spin gap of isolated rung as a function of  $\phi$ .

where  $E_0$  is the ground state energy and  $E_n$  is the  $n$ th excited state energy. Figures 6.4(b) and 6.4(c) show the finite-size scaling analysis of  $\Delta_1(L)$  for several values of  $\phi$  and the  $L \rightarrow \infty$  extrapolated value of  $\Delta_1$  as a function of  $\phi$ , respectively. It is remarkable that the gap is clearly asymmetric about  $\phi = 0$ , reaching its maximum at  $\phi \sim 0.1\pi$ : this could be understood by noticing that both  $K$  and  $J$  are AFM in the region of  $0 < \phi < \frac{1}{2}$ , while,  $K$  and  $J$  have different signs in the region of  $-\frac{1}{2}\pi < \phi < 0$ . The gap closes gradually with approaching the boundary to the stripy phase at  $\phi = -0.3\pi$  and to the AFM KSL phase at  $\phi = 0.48\pi$ . Thus, they are both continuous transitions.

Let us provide a more comprehensive explanation about the asymmetry of the gap in respect to  $\phi$ . In an AFM Heisenberg ladder, it is known that the magnitude of the gap roughly scales with the AFM rung interaction. This also means that the spin-spin correlations are strongly screened. Therefore, a single dimer may be expected to be an effective model to reproduce the gap behaviour. We then extract an isolated rung:  $\frac{J}{2}(S_1^+ S_2^- + S_1^- S_2^+) + (J + K)S_1^z S_2^z$  from our system (6.1). This two-site system can be easily diagonalised and the gap is obtained as  $\Delta_{i\text{-rung}} = \frac{2J+K}{2}$  for  $\phi < 0$  and  $\Delta_{i\text{-rung}} = J$  for  $\phi > 0$ . In the inset of Fig. 6.4(c) the gap obtained for the isolated rung is plotted. The qualitative trend of the gap with  $\phi$  is well described by the single dimer. Furthermore, the gap closing points at  $\phi = \tan^{-1}(-2) \approx -0.35\pi$  and  $\phi = \frac{1}{2}\pi$  are very close to those for the original KH ladder. It proves the strong screening of spin-spin correlations in the whole rung-singlet phase.

We note that the rung-singlet state is a special feature of the KH ladder with even number of legs. If the number of legs is odd, the system is gapless; and in the limit of infinite number of legs, i.e., 2D honeycomb lattice, the system exhibits a Néel order.



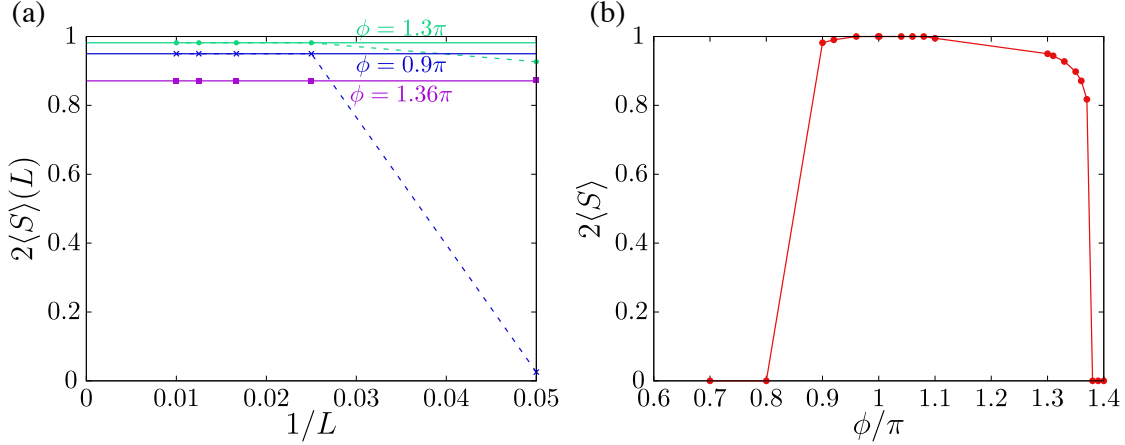


Figure 6.5: (a) Finite-size scaling of the local spin  $\langle S \rangle$  for several values of  $\phi$ . Dotted lines help the eye follow the data points, solid lines represent the fitting. (b) Extrapolated values of  $\langle S \rangle$  as a function of  $\phi/\pi$ .

### 6.3.4 Ferromagnetic phases

At  $\phi = \pi$  ( $J = -1$ ,  $K = 0$ ), the system is in an  $SU(2)$  isotropic FM state. This state can be expressed as a sum of fully polarised spin configurations for all of the total  $S^z$  sectors, namely,  $S_{\text{tot}}^z = \sum_i S_i^z = 0, \pm 1, \pm 2, \dots, \pm L$ . On leaving  $\phi = \pi$ , the sectors are lifted: For  $|\pi - \phi| \ll 1$ , the first order perturbation in the Hamiltonian (6.1) is given by

$$\begin{aligned}
 \mathcal{H}' = & \frac{\pi - \phi}{4} \sum_{j=1}^2 \sum_{i=1}^L (S_{i,j}^+ S_{i+1,j}^- + S_{i,j}^- S_{i+1,j}^+) \\
 & + \frac{\pi - \phi}{4} \sum_{j=1}^2 \sum_{i=1}^L (-1)^{(i+j)} (S_{i,j}^+ S_{i+1,j}^+ + S_{i,j}^- S_{i+1,j}^-) \\
 & + (\pi - \phi) \sum_{i=1}^L S_{i,1}^z S_{i,2}^z,
 \end{aligned} \tag{6.13}$$

where the nonperturbative part is the simple FM Heisenberg ladder with  $J = -1$  ( $\forall$  NN bonds). To gain the energy benefits by  $\mathcal{H}'$ , the total  $S^z$  sectors in the wave function are restricted to  $S_{\text{tot}}^z = 0, \pm 2, \pm 4, \dots, \pm L$ . Thus, near the vicinity of  $\phi = \pi$  the ground state is approximately denoted by

$$|\psi\rangle \approx \frac{1}{\sqrt{\mathcal{N}}} \sum_m |\phi_m\rangle \tag{6.14}$$

where  $m$  runs over all the possible spin configurations  $|\phi_m\rangle$  ( $m = 1 \dots \mathcal{N}$ ) with  $S_{\text{tot}}^z = 0, \pm 2, \pm 4, \dots, \pm L$ ,  $\mathcal{N}$  is the number of the spin configurations, i.e.,  $\mathcal{N} = \sum_{n=0}^L 2L C_{2n} = \sum_{n=0}^L \frac{(2L)!}{(2n)!(2L-2n)!}$ . As a result, the polarised direction is  $[110]$  in the spin space, namely,  $\langle S_i^x S_j^x \rangle = \langle S_i^y S_j^y \rangle = \frac{1}{8}$  and  $\langle S_i^z S_j^z \rangle = 0$  ( $\forall i, j$ ). We call it the FM- $xy$  state. This breaking of the  $SU(2)$  symmetry is a consequence of the double-spin-flip term, which immediately suppressed the spin polarisation along the  $z$  axis.

To determine the range of the FM- $xy$  phase, we calculate the total spin per rung

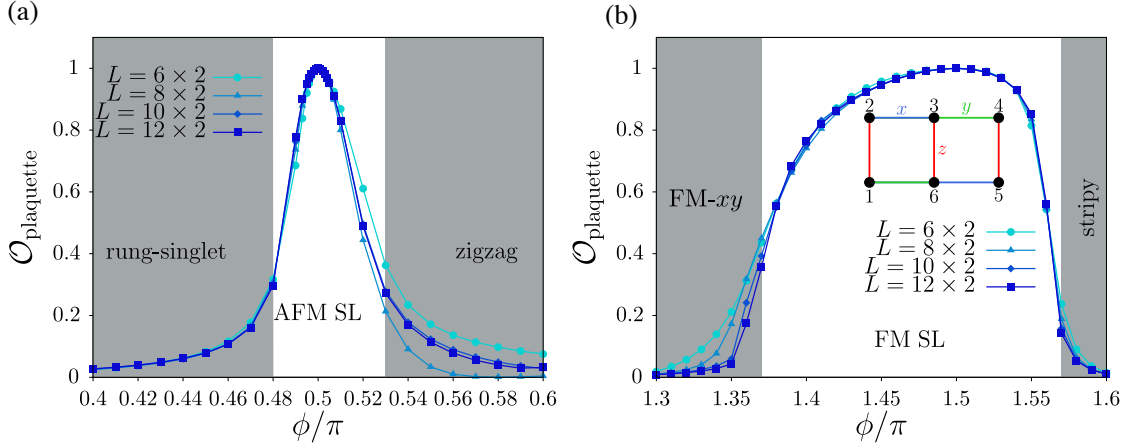


Figure 6.6: Expectation value of the plaquette operator around (a) the AFM SL point  $\phi = \pi/2$  and (b) the FM SL point  $\phi = 3\pi/2$  for different system lengths. Shaded areas show the neighbouring LRO phases. The insets in (a) and (b) show the considered six-site plaquette corresponding to a hexagon in the honeycomb-lattice KH model.

$S^{\text{tot}}/(2L)$ , defined by

$$S^{\text{tot}}(S^{\text{tot}} + 1) = \sum_{j,j'=1}^2 \sum_{i,i'=1}^L \mathbf{S}_{i,j} \cdot \mathbf{S}_{i',j'} \quad (6.15)$$

and the local spin

$$\langle S \rangle = \sqrt{\langle S_{i,j}^x \rangle^2 + \langle S_{i,j}^y \rangle^2 + \langle S_{i,j}^z \rangle^2} \quad (6.16)$$

at the centre of the system  $i = \frac{L}{2}$ . Note that we can directly detect the local moment in the FM state since the spin rotation symmetry is broken by using open boundary conditions. We have confirmed  $\langle S \rangle = S^{\text{tot}}/(2L)$  in the thermodynamic limit. Figure 6.5 shows  $2\langle S \rangle$  as a function of  $\phi$ . At the isotropic SU(2) point ( $\phi = \pi$ ),  $2\langle S \rangle = S^{\text{tot}}/L = 1$ . We find that  $2\langle S \rangle$  decays very slowly from 1 as the distance from  $\phi = \pi$ , and keeps  $\sim 1$  in the whole FM- $xy$  region  $0.8\pi < \phi < 1.37\pi$ . The robustness of the FM- $xy$  state is naively expected because both  $J$  and  $J + K$  are FM at  $\frac{3}{4}\pi < \phi < \frac{3}{2}\pi$ . Then, at both boundaries, to the zigzag state at  $\phi = 0.8\pi$  and to the spin liquid state  $\phi = 1.37\pi$ , it sharply drops down to 0, which indicates first-order transitions.

## 6.4 Spin-liquid states

We have determined the phase boundaries of LRO phases covering most of the  $\phi$  range. In the remaining two narrow  $\phi$  regions around the Kitaev points  $\phi = \pm\frac{\pi}{2}$ , we found no long-range ordering, i.e., they are *spin-liquid* states. To consider the similarity to the so-called KSL in the honeycomb KH model, we compute the expectation value of plaquette operator and the excitation gap.

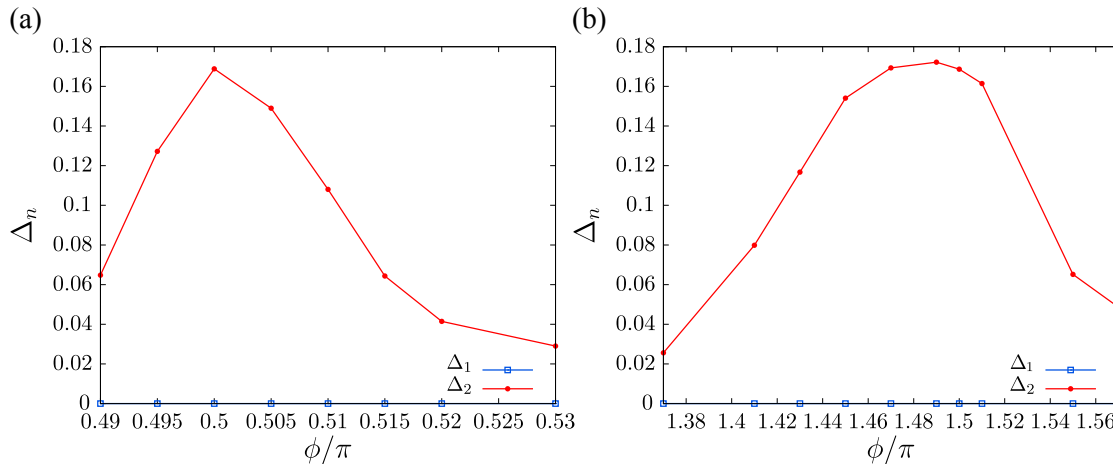


Figure 6.7:  $L \rightarrow \infty$  extrapolated gap of first and second excited states from the ground state as a function of  $\phi$ : (a) AFM QSL, (b) FM QSL.

### 6.4.1 Plaquette operator

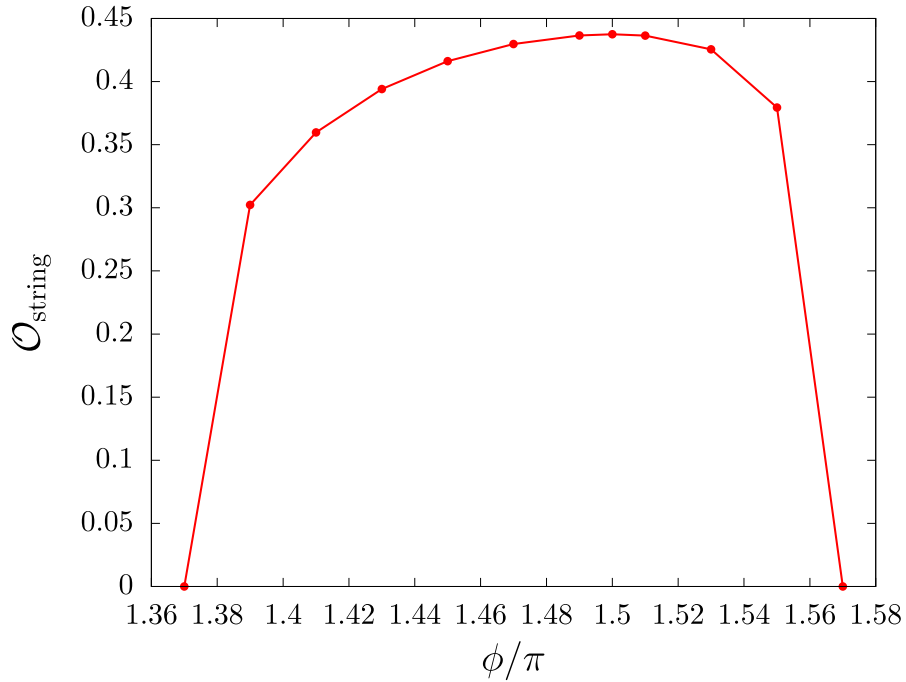
It is known that the Kitaev model, e.g., on a hexagonal cluster and ladder, is in a  $\pi$ -flux state. This state is characterised by the expectation value of plaquette operator to be unity. We define the expectation value of the plaquette operator for our system (6.1) as

$$\mathcal{O}_{\text{plaquette}} = \langle S_1^x S_2^y S_3^z S_4^x S_5^y S_6^z \rangle \quad (6.17)$$

where the numbering of sites is indicated in the inset of Fig. 6.6(b). Note that this six-site plaquette corresponds to a hexagon in the honeycomb-lattice KH model. In Fig. 6.6 we show  $\mathcal{O}_{\text{plaquette}}$  calculated with ED for several ladder lengths under periodic boundary conditions. The finite-size effect seems to be negligible within the spin-liquid phases. At both of the Kitaev points  $\phi = \pm\pi/2$ ,  $\mathcal{O}_{\text{plaquette}}$  is 1 as expected. With moving away from  $\phi = \pm\pi/2$ ,  $\mathcal{O}_{\text{plaquette}}$  decreases but keeps  $\sim 1$  in finite regions. In the vicinities of the neighboring LRO phases, it decreases rapidly to  $\sim 0$ . This means that the ranges of spin-liquid phases characterized by nonzero  $\mathcal{O}_{\text{plaquette}}$  are consistent to the phase boundaries with the LRO state estimated by order parameters and spin moment. Interestingly, the region of FM SL is a few times wider than that of AFM SL. This is similar to the trend in the honeycomb KH model (see below). We have also confirmed that the spin-spin correlations are finite only between neighbouring sites at the Kitaev points, as in the honeycomb-lattice KH model.

### 6.4.2 Excitation gap

We compute the excitation gaps  $\Delta_1$  and  $\Delta_2$  around the AFM and FM Kitaev point  $\phi = \pm\frac{1}{2}\pi$  using Eq. (6.12). In Fig. 6.7 the excitation gaps are plotted as a function of  $\phi/\pi$ . In both cases, the first excitation gap  $\Delta_1$  seems to vanish; whereas the second excitation gap  $\Delta_2$  is clearly finite over the whole interested region. It means that the disordered phase around the Kitaev points is characterised as a gapped KSL, although the ground state is doubly degenerate. This is consistent with the previous studies in Refs. [138, 139, 140]. Therefore, we can conclude that the spin liquid state of the KH

Figure 6.8: String order parameters  $\mathcal{O}_{\text{string}}$  as a function of  $\phi$ .

ladder is different in terms of excitations from an isotropic gapless KSL state of the honeycomb-lattice KH model. It is also worth mentioning that for the FM QSL, the maximal value of  $\Delta_2$  is given a bit away from the FM Kitaev point,  $\phi \sim 1.49\pi$ . We also point out that the gap  $\Delta_1$  reported in Fig. 6.7(a) is finite in the rung singlet state and closes continuously at  $\phi \approx 0.49\pi$ .

### 6.4.3 String order parameter

Hidden (non local) order is a key feature to know the topological properties of a spin system and it has been so far recognised in various ladder systems. In particular, as discussed in previous studies [93, 139, 140], the string (or brane) order is expected in the Kitaev systems. To confirm it numerically, we calculate the string order parameter which is defined by

$$\mathcal{O}_{\text{string}} = \lim_{|i-j| \rightarrow \infty} \langle S_{i,1}^y S_{i,2}^x \left( \prod_{k=i+1}^{j-1} S_{k,1}^z S_{k,2}^z \right) S_{j,1}^y S_{j,2}^x \rangle. \quad (6.18)$$

To obtain the values in the thermodynamic limit, we choose  $i = \frac{L}{4}$  and  $j = \frac{3L}{4}$  with system length  $L = 8n$  ( $n$ : integer). We calculate the string order parameters (6.18) for systems with length up to  $L = 76$  and perform finite-size scaling analysis. The  $L \rightarrow \infty$  extrapolated results around the FM Kitaev point are plotted as a function of  $\phi/\pi$  in Fig. 6.8. The presence of a long-ranged string order is clearly seen in the whole range of the FM SL phase. The maximum is found at the FM Kitaev point.

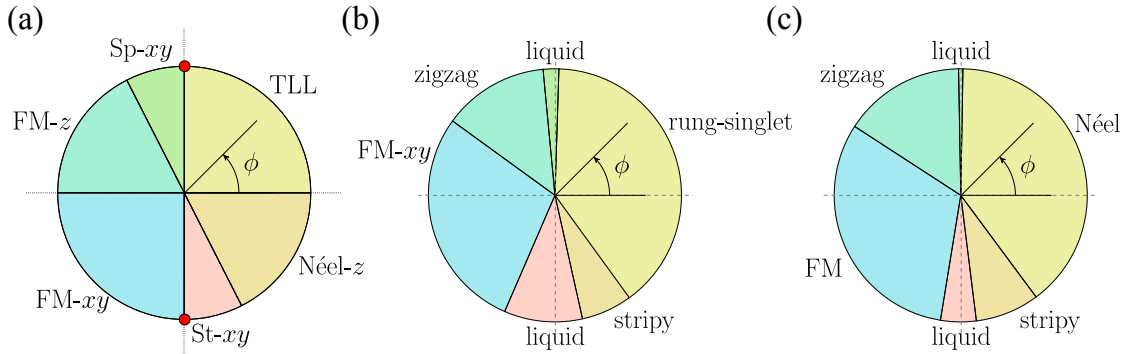


Figure 6.9: (a)  $\phi$ -dependent Phase diagram of the 1D KH model as determined in Chapter 5. (b) Phase diagram of the KH ladder, obtained in this chapter. (c) Phase diagram of the honeycomb-lattice KH model adapted from Ref. [131].

## 6.5 Phase diagram

Based on the above numerical results, we present the  $\phi$ -dependent ground state phase diagram of the KH ladder in Fig. 6.9(b). For an easier comparison, we also show the ground state phase diagrams of the KH model on a single chain reported in the previous chapter (Sec. 5.4) and on a honeycomb lattice [131] in Figs. 6.9(a) and 6.9(c), respectively. As discussed in Chapter 5, all the LRO states of the honeycomb-lattice KH model can be interpreted in terms of the coupled KH chains. Surprisingly, we now found that the phase diagram of just two coupled KH chains, i.e., the KH ladder, is getting more similar to that of the 2D honeycomb-lattice KH model. The only recognisable differences are the following:

- (i) The Néel phase is replaced by the rung-singlet phase. The rung-singlet gap decreases with increasing the number of KH chains and goes to zero in the honeycomb KH limit. This is essentially the same as the relation between  $n$ -leg Heisenberg ladder and 2D Heisenberg model.
- (ii) The KSL phases in the KH ladder is wider than those in the honeycomb-lattice KH model because the quantum fluctuations are stronger due to the low dimensionality.

Finally, to get further insights into the topological properties of our system (6.1), we investigate the entanglement spectrum [77]. Using Schmidt decomposition, the ground state can be expressed as

$$|\psi\rangle = \sum_i e^{-\xi_i/2} |\phi_i^A\rangle \otimes |\phi_i^B\rangle, \quad (6.19)$$

where the states  $|\phi_i^S\rangle$  correspond to an orthonormal basis for the subsystem  $S$  (either A or B). We study a periodic ladder with  $L \times 2 = 32 \times 2$  sites and divide it into isometric subdomains A and B with  $\frac{L}{2} \times 2$  sites. In our calculations, the ES  $\{\xi_i\}$  is simply obtained as  $\xi_i = -\ln \lambda_i$ , where  $\{\lambda_i\}$  are the eigenvalues of the reduced density matrices after the bipartite splitting. The low-lying entanglement spectrum levels are plotted as a function of  $\phi$  in Fig. 6.10. We find that the lowest level has no degeneracy in the magnetic LRO phases, which are topologically trivial. In the SL phases, the lowest level has two fold degeneracy confirming the existence of Majorana zero modes and the higher levels have high degrees of degeneracy. These are consistent with the ground state phase diagram.

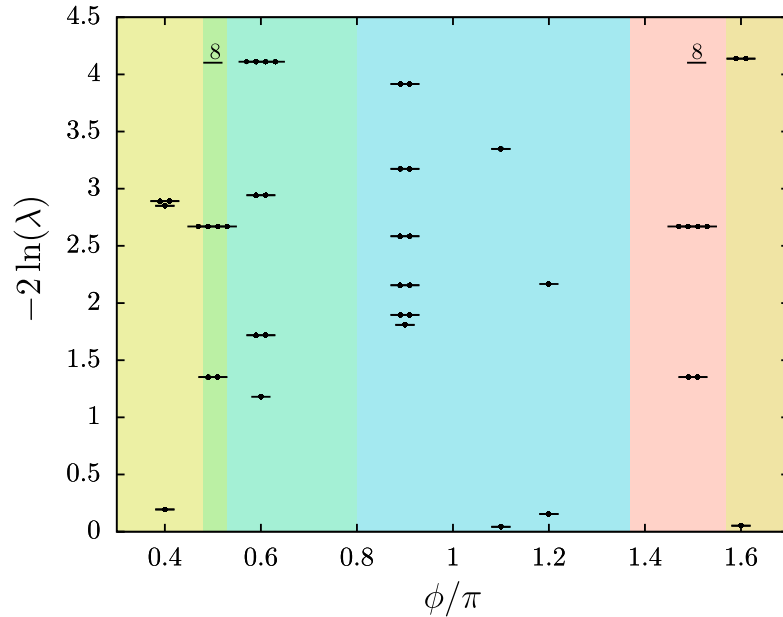


Figure 6.10: Entanglement spectra for representative  $\phi$ -points of the different phases in the ground-state phase diagram. The used system size is  $L \times 2 = 32 \times 2$  for the LRO states and  $L \times 2 = 24 \times 2$  for the two Kitaev points.

## 6.6 Low-lying excitations

In this section, we study the low-lying excitations of the KH ladder by calculating the dynamical spin structure factor. We compute both  $S^z(q, \omega)$  and  $S^-(q, \omega)$  for each of the LRO phase. For the FM KSL state we compute them at three different  $\phi$  values to study the effect of the Heisenberg interaction on the dispersion. The calculations were done using ED and a ladder of size  $L = 12 \times 2$  with periodic boundary conditions.

### 6.6.1 Rung-singlet phase

Figure 6.11(a) shows the dynamical structure factors for the rung-singlet state at  $\phi = 0.2\pi$  ( $J \sim 0.81, K \sim 0.59$ ). The largest peak appears in  $S^-(q = 0, \omega \sim 0.6)$  reflecting the dominant AFM fluctuations along the leg. The value of  $\omega \sim 0.6$  corresponds to the excitation gap  $\Delta$  estimated above. The intensities in  $S^-(q, \omega)$  are larger than those in  $S^z(q, \omega)$  due to the easy-plane  $xy$  anisotropy. As indicated by the dotted line, the spin-triplet dispersion  $\omega(q)$  of  $S^z(q, \omega)$  can be well explained by that of the two-leg Heisenberg ladder with the ratio between rung and leg interactions  $\frac{\text{rung}}{\text{leg}} \approx \frac{J+K}{J} \sim 1.7$  (Ref. [141]). The spin-triplet dispersion of  $S^-(q, \omega)$  is similar in shape but it splits with the width  $\sim \pm \frac{K}{2}$  at  $q = \pi$ . This splitting of the spin-triplet dispersion is a general feature in the system including the sign-alternating double-spin-flip term as seen in Sec. 5.5. The width of spin-triplet dispersion in  $S^z(q, \omega)$  and  $S^-(q, \omega)$  roughly scales to  $J$  and  $J + \frac{K}{2}$ , respectively.

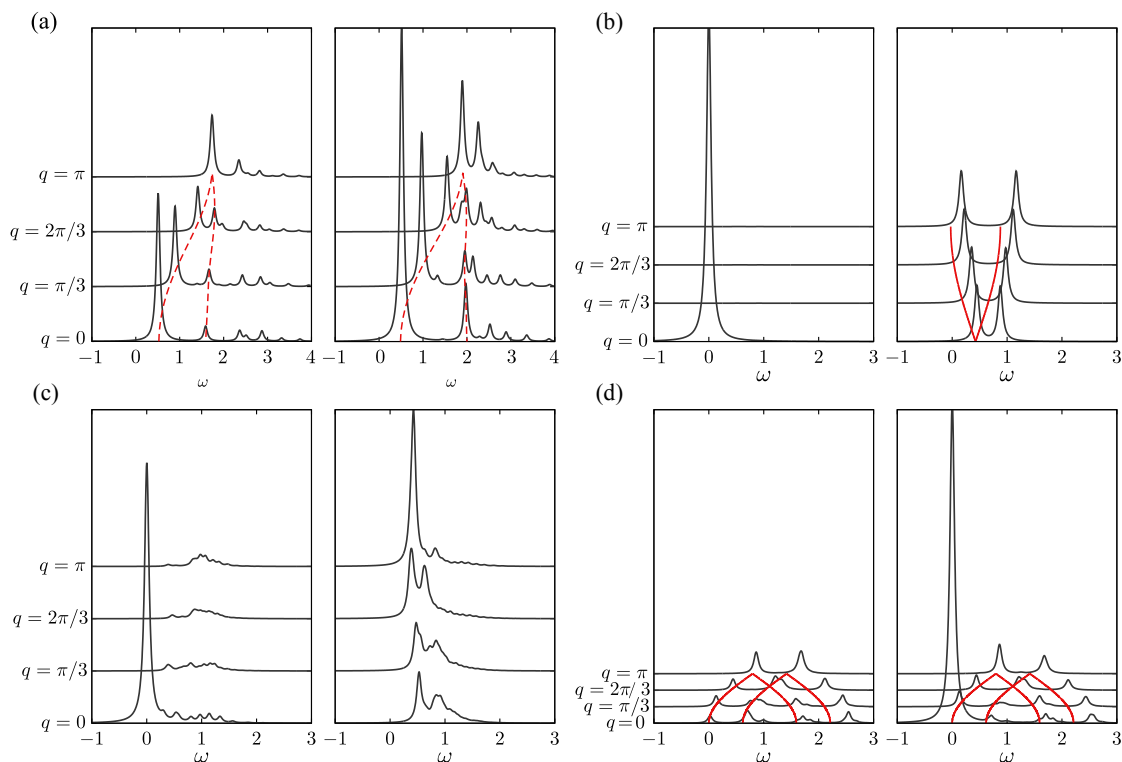


Figure 6.11: Dynamical structure factors calculated with a  $12 \times 2$  ladder with periodic boundary conditions in the (a) rung-singlet ( $\phi = 0.2\pi$ ), (b) stripy ( $\phi = 1.64\pi$ ), (c) zigzag ( $\phi = 0.6\pi$ ), and (d) FM- $xy$  ( $\phi = 0.9\pi$ ) phases. The left and right panels show  $S^z(q, \omega)$  and  $S^-(q, \omega)$ , respectively. The red dotted lines are guides to the eye and red solid lines are spin-triplet dispersion obtained by the spin-wave theory.

### 6.6.2 Stripy phase

Figure 6.11(b) shows the dynamical structure factors for the stripy state at  $\phi = 1.64\pi$  ( $J \sim 0.43, K \sim -0.9$ ) where the single leg can be basically regarded as an easy-axis AFM  $XXZ$  Heisenberg chain. In  $S^z(q, \omega)$  the largest peak appears at  $(q, \omega) = (0, 0)$  due to the Néel ordering along the leg. Very few weights in the other momenta prove the validity of Eq. (6.6) with almost perfect alignment of spins parallel or antiparallel to the  $z$  axis and very weak quantum fluctuations, whereas the spin-triplet dispersion of  $S^-(q, \omega)$  is basically explained by a single magnon dispersion. Thus, the spectral weight is almost uniform for all  $q$  values, and the dispersion is obtained by spin-wave theory as

$$\omega(q) = J \pm \frac{K}{2} \sin \frac{q}{2}. \quad (6.20)$$

The good agreement can be seen in Fig. 6.11(b). Since the stripy order parameter drops on both phase boundaries, Eq. (6.20) would give at least qualitatively a good approximation for the spin-triplet dispersion in the whole stripy phase.

### 6.6.3 Zigzag phase

Figure 6.11(c) shows the dynamical structure factors for the zigzag state at  $\phi = 0.6\pi$  ( $J \sim -0.31, K \sim 0.95$ ) where each leg is ferromagnetically ordered. The system can be

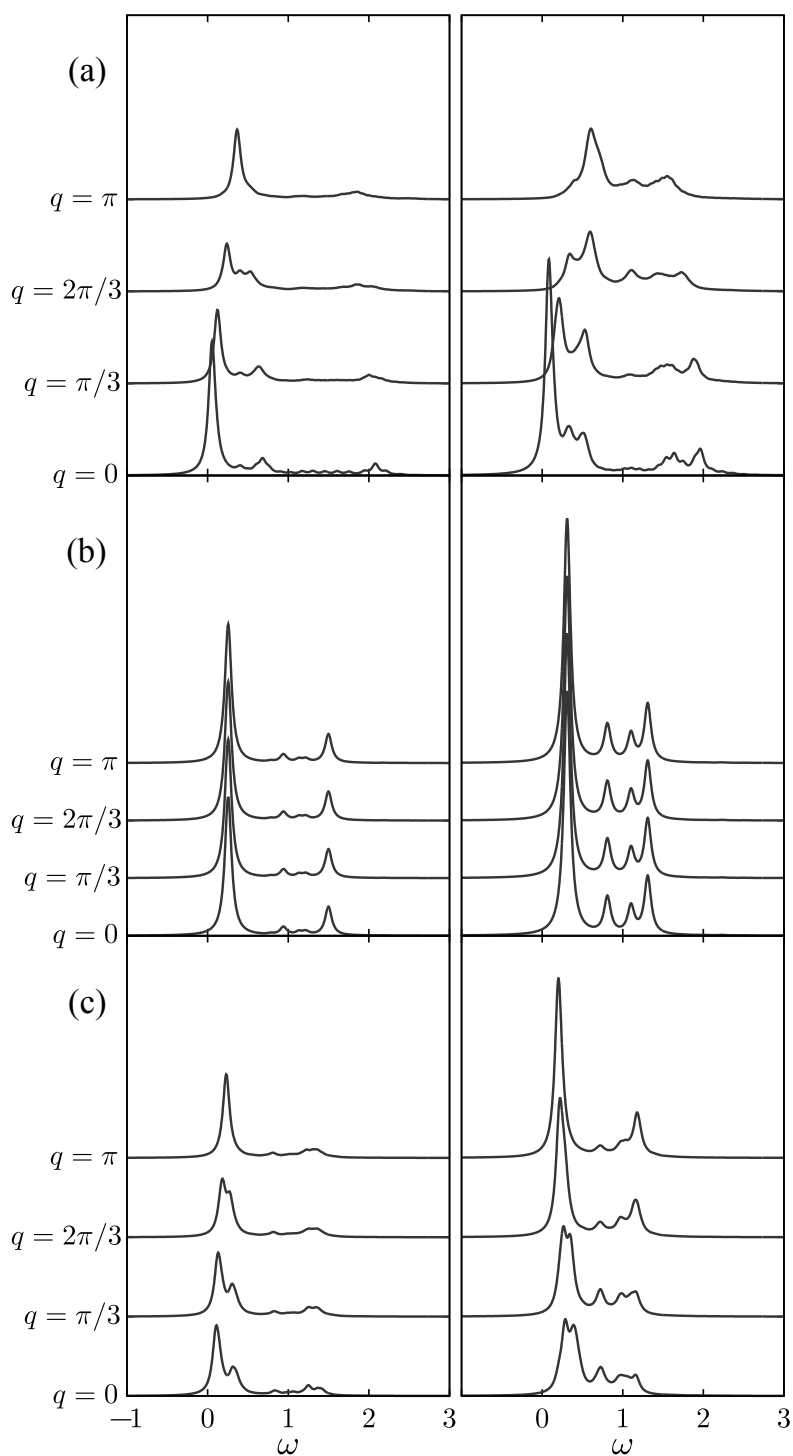


Figure 6.12: Dynamical structure factors in the FM KSL phase, calculated with a  $12 \times 2$  ladder under periodic boundary conditions for (a)  $\phi = 1.4\pi$ , (b)  $\phi = 1.5\pi$ , and (c)  $\phi = 1.54\pi$ . The left and right panels show  $S^z(q, \omega)$  and  $S^-(q, \omega)$ , respectively. The results for the AFM Kitaev point  $\phi = 0.5\pi$  are exactly the same as in (b).



understood as two FM chains coupled by the Ising-like AFM coupling. The largest peak in  $S^z(q = 0, \omega \sim 0)$  reflects the FM ordering along the leg. The weights in the other momenta are small since the spins are mostly aligned along the  $z$  axis; however, they seem to be larger than those for the stripy state. This implies that the zigzag ordering is more fragile than the stripy ordering. In  $S^-(q, \omega)$  a largest and lowest-lying peak appears at  $q = \pi$ , indicating a four-site periodicity along the leg. The shape of the dispersion is similar to that of the staggered- $xy$  ordered state in the 1D KH model. Nevertheless, the gapped peak position  $\omega \sim 0.42$  clearly suggests no ordering on the  $xy$  plane. The intensities in  $S^-(q, \omega)$  are larger than those in  $S^z(q, \omega)$  due to the easy-plane  $xy$  anisotropy.

#### 6.6.4 FM states

Figure 6.11(d) shows the dynamical structure factors for the FM- $xy$  state at  $\phi = 0.9\pi$  ( $J \sim -0.95, K \sim 0.30$ ). The largest peak in  $S^-(q = 0, \omega \sim 0)$  confirms that the spins lie mostly on the  $xy$ -plane. The other features are very similar between  $S^z(q, \omega)$  and  $S^-(q, \omega)$ . Both of them have the same excitation dispersion as

$$\omega_1(q) = -\frac{2J + K}{2} \left(1 \pm \cos \frac{q}{2}\right), \quad (6.21)$$

and

$$\omega_2(q) = -\frac{2J + K}{2} \left(1 \pm \cos \frac{q}{2}\right) + 2|K|. \quad (6.22)$$

The splitting between  $\omega_1(q)$  and  $\omega_2(q)$  becomes zero in the isotropic SU(2) symmetric point at  $q = \pi$  and it is roughly proportional to  $|K|$ .

#### 6.6.5 Kitaev spin liquid

In Fig. 6.12 we show the dynamical structure factors around the FM Kitaev point ( $\phi = \frac{3}{2}\pi$ ). At the FM Kitaev point, both  $S^z(q, \omega)$  and  $S^-(q, \omega)$  show no dependence on  $q$ . This dispersionless feature is a natural consequence of no spin-spin correlations except the nearest-neighbour ones. The distance between the lower and upper bound of the continuum in  $S^-(q, \omega)$  is of the order of  $|K|$ , relating to the spinon propagation along the leg. Note that the spectra at the AFM Kitaev point are exactly the same as those at the FM Kitaev point. Let us then see the effect of the Heisenberg term on the spectra. Figures 6.12(a) and 6.12(c) show the dynamical structure factors at  $\phi = 1.4\pi$  and  $\phi = 1.54\pi$ , respectively. Although they are almost equally close to the boundary to the neighbouring phase, the spectra are apparently quite different: At  $\phi = 1.54$  it mostly keeps the spectral features at the Kitaev point except that the main peak splits into two peaks with a small interval  $\sim J$ ; while at  $\phi = 1.4\pi$  the dispersionless feature is completely collapsed and its lower bound looks rather similar to the spin-triplet dispersion of the FM- $xy$  state. It may be related to the fact that the expectation value of the plaquette operator deviates faster from the pure KSL value ( $\mathcal{O}_{\text{plaquette}} = 1$ ) at  $\phi < \frac{3}{2}\pi$  ( $J < 0$ ) than at  $\phi < \frac{3}{2}\pi$  ( $J > 0$ ) with leaving from the FM Kitaev point. This also suggests that the SL state at  $J < 0$  is more easily destroyed by external perturbations, e.g., magnetic field.

## 6.7 Discussion

We studied the ground state and low-lying excitations of the KH model on a ladder using the DMRG and Lanczos ED methods. Based on the results of several order parameters, excitation gap, and entanglement spectra, we determined the ground state phase diagram as a function of the ratio between Kitaev and Heisenberg interactions. The phase diagram is very rich and includes four magnetically ordered phases, namely, rung singlet, stripy, zigzag, FM, and two spin-liquid phases. The phase diagram is strikingly similar to that of the KH model on a honeycomb lattice. Distinct differences are only the presence of a rung-singlet phase instead of the Néel state and a few times wider ranges of the two spin-liquid phases. These differences can be understood through the dimensionality: (i) Though the two-leg KH ladder has a finite excitation gap in the rung-singlet phase around  $\phi = 0$  due to strong cluster anisotropy, the gap decreases with increasing the number of legs and becomes zero in the limit of the 2D honeycomb-lattice KH model. (ii) Since the quantum fluctuations are typically stronger in a lower dimensional system, it is more difficult to stabilise LRO state in the ladder than in a 2D system. Moreover, the fact that these two QSL states exhibit a finite gap beyond the 2-fold degenerate ground state can also be understood in terms of the lowered geometry of the lattice when compared to the 2D case. In fact, as in the rung singlet case, the gap would decrease with increasing the number of coupled chain and it would vanish in the limit of infinite coupled chains. Interestingly, the rung-singlet phase shows the same geometry as the valence bond crystal induced by pressure in  $\alpha$ - $\text{RuCl}_3$  [142]. We also calculated the dynamical spin structure factor using the Lanczos ED method. Noticeably, most of the spectral features in the KH ladder can be explained by considering those of the 1D KH model determined in Sec. 5.5.

# 7 Conclusion

Quantum magnetism is a vast and worth of exploring field. In particular, magnetic frustration opens the door to new possible exotic phases of matter, like spin liquids, spin ices, and nematic phases. Much of what lies behind that door is yet to be completely understood. In this work, we focused on a special class of frustrated spin systems, namely one- (1D) and quasi-one-dimensional models. Though real, effectively 1D materials are not so common, there exist different classes of materials where an effective 1D Hamiltonian is enough to capture the experimental feature, such as magnetisation curve and inelastic neutron scattering spectra, thus motivating our theoretical investigation.

We have presented possible realisations of such systems exhibiting geometric frustration in Chapter 2. A class of materials that supports the realisation of spin- $\frac{1}{2}$  chains is cuprates. The most celebrated one is  $\text{CuGeO}_3$ , which was the first inorganic material to exhibit a spin-Peierls transition. This material exhibits an antiferromagnetic (AFM) nearest neighbour (NN) interaction. Other cuprate chains, however, have been found to have a ferromagnetic (FM) NN interaction, i.e., they are described by the FM  $J_1$ - $J_2$  model. We have analysed this model in Chapter 3. Some of its features were already known, namely that the system is in a FM state for  $J_2/|J_1| < 1/4$  and that it exhibits incommensurate spiral spin correlations for larger values of  $J_2/|J_1|$ . Nonetheless, a question remained open about the behaviour of the spin gap. In fact, mean field theory predicted the gap to open around  $J_2/|J_1| \sim 3.3$  with a value of  $\Delta \sim 10^{-40}|J_1|$ , but failed for smaller  $J_2/|J_1|$  values. We have presented our numerical prediction for the existence of a spin gap for  $J_2/|J_1| > 1/4$ . Moreover, we have thoroughly analysed the ground state supporting the gap and found it to be an Affleck-Kennedy-Tasaki-Lieb (AKLT)-like valence bond solid (VBS) with valence bonds forming between third neighbours. We call this state  $\mathcal{D}_3$ -VBS state. We were able to characterise this state by computing dimer order parameters for first, second and third neighbours and a string order parameter. We proved this state to be topologically non-trivial by studying its entanglement spectrum. Therefore, we concluded that the phase transition from the FM gapless to the  $\mathcal{D}_3$ -VBS can be understood in two steps: first, a ferromagnetic dimerisation between first neighbours spontaneously breaks translational symmetry, next these FM dimers give rise to an effective  $S = 1$  AFM chain that supports an AKLT-like VBS with a Haldane gap.

We also considered a dimerised model, namely a  $J_1$ - $J'_1$ - $J_2$  chain, where translational symmetry is already broken in the Hamiltonian. The introduction of the dimerisation parameter  $\beta = J'_1/J_1$  has two effects on the phase diagram: (i) with decreasing  $\beta$ , the FM region shrinks and (ii) considering the same value of  $\alpha$ , the gap is enhanced with decreasing  $\beta$ . In particular, the gap is due to the presence of a VBS in the ground state. This, however, presents a crossover from next nearest neighbours to a third-neighbour VBS.

While this model captures most of the physics for the frustrated cuprate chains with FM NN interactions, real materials often present a finite interchain coupling  $J'$  and one may also need to include further interactions, like Dzyaloshinskii-Moriya interaction, in

order to capture their low-energy physics. Moreover, the FM  $J_1$ - $J_2$  chain is known to exhibit multipolar ordering in high magnetic field. A different approach to access this kind of multipolar physics would be to study two AFM coupled chains. In this case, an Ising interchain coupling would act like an effective field, lowering the value of the saturation field. The effects of a Heisenberg coupling and other XXZ anisotropic interaction are, currently, unclear. We believe investigating the possibility of multimagnon bound states in this setting will improve our understanding of spin chain materials and open up the possibility of multipolar physics at lower fields. Furthermore, when dealing with real materials, several of them also exhibit a small, but finite, third neighbour interaction. It is currently undetermined what the effect of this third neighbour coupling is on the spin gap. A future numerical investigation using the DMRG method could answer this question and also shed light on the nematicity in these materials.

The second part of this work focused on exchange frustration, particularly the Kitaev-Heisenberg (KH) model. We have shown how the KH model features non-trivial physics also in lower dimension. We have first analysed a simple chain with alternating  $x$  and  $y$  interactions and Heisenberg interaction on all bonds. Though it is not possible to have a Kitaev spin liquid in this geometry due to the lack of  $z$  bonds, the phase diagram is still found to be extremely rich. In particular, it has six different phases: two without long-range magnetic order, namely Tomonaga-Luttinger liquid (TLL) and spiral- $xy$  state, and four of which are long-range-ordered, namely FM- $z$ , FM- $xy$ , staggered- $xy$  and Néel- $z$ . Moreover, this system has two singular Kitaev points at  $\phi = \pm \frac{\pi}{2}$ . At these two points, the system is a  $p$ -wave superconductor, namely a Kitaev chain. Remarkably, it is possible to map the long range ordered states of the KH chain to those of the 2D honeycomb model by coupling the chains in a brick-wall fashion through  $z$ -bonds. In this way, the FM- $z$  state gives rise to the zigzag and FM state on the honeycomb, depending on the sign of the interactions on the rungs; the FM- $xy$  naively goes into the FM state, while the Néel- $z$  state transforms into the stripy and Néel phase depending on the sign of the rung interaction. The TLL, being unstable to any perturbation, gives rise to the Néel state on the 2D honeycomb lattice, as the interaction between the chains is AFM.

This naive mapping from a 1D model to its 2D counterpart is rare and unexpected and we proved it further by studying the KH model on a two-legged ladder. In this case, the presence of  $z$  bonds and the threefold coordination of the lattice make it possible for the system to support the presence of a Kitaev spin liquid. We found the ground state phase diagram to be strikingly similar to that of the 2D honeycomb model. In particular, the differences between the two diagrams can be understood in terms of the different dimensionality: (i) on the ladder, a rung-singlet state stabilises in the region where the 2D honeycomb model exhibits Néel ordering. The rung singlet state has a finite gap, in contrast with the 2D phase. When extending the ladder to contain more coupled chains, the gap is expected to decrease and it will vanish in the limit of an infinite number of coupled chains. (ii) The liquid regions are more extended in the quasi-1D case. This is interpreted in terms of the stronger effects of quantum fluctuations on lower dimensional systems. These two liquid states are gapped. This gap, however, would behave as that of the rung singlet state when changing the dimensionality, so that the spin liquid states on the two-legged ladder would become gapless Kitaev spin liquid in the 2D limit. In

---

addition, the low-lying excitations of the ladder are well explained by the pure 1D chain. We also note that the spectral properties of the long range ordered states in the 2D honeycomb are expected to be similar to those of the ladder, due to symmetry breaking in the  $k_y$  direction.

Experimental studies have suggested the possibility of field induced spin liquid behaviour in  $\alpha$ - $\text{RuCl}_3$  [104, 105]. This transition is currently interpreted as a melting of AFM order to a liquid state. However, the microscopic mechanism behind this transition is still under debate. A possible way to investigate this mechanism is by making use of the KH ladder. In fact, this model realises the liquid-zigzag transition with the advantage of being quasi-1D, allowing for great numerical accuracy. By analysing the effect of the magnetic field on the ladder, one hopes to gain insight on how the AFM order transforms into a Kitaev spin liquid.



# Bibliography

---

- [1] E. Ising, *Beitrag zur Theorie des Ferromagnetismus*, Z. Phys. **31**, 253 (1925). 1
- [2] R. Peierls, *On Ising's model of ferromagnetism*, Math. Proc. Cambridge Philos. Soc. **32**, 477 (1936). 1
- [3] L. Onsager, *Crystal statistics. I. A two-dimensional model with an order-disorder transition*, Phys. Rev. **65**, 117 (1944). 1
- [4] M. Billó, M. Caselle, D. Gaiotto, F. Gliozzi, M. Meineri, and R. Pellegrini, *Line defects in the 3D Ising model*, Journal of High Energy Physics **2013**, 55 (2013). 1
- [5] C. Cosme, J. M. V. P. Lopes, and J. Penedones, *Conformal symmetry of the critical 3D Ising model inside a sphere*, Journal of High Energy Physics **2015**, 22 (2015). 1
- [6] B. Delamotte, M. Tissier, and N. Wschebor, *Scale invariance implies conformal invariance for the three-dimensional Ising model*, Phys. Rev. E **93**, 012144 (2016). 1
- [7] C. G. Shull and J. S. Smart, *Detection of antiferromagnetism by neutron diffraction*, Phys. Rev. **76**, 1256 (1949). 1
- [8] N. D. Mermin and H. Wagner, *Absence of ferromagnetism or antiferromagnetism in one- or two-dimensional isotropic Heisenberg models*, Phys. Rev. Lett. **17**, 1133 (1966). 2
- [9] P. Anderson, *Resonating valence bonds: A new kind of insulator?*, Mater. Res. Bull. **8**, 153 (1973). 3
- [10] D. A. Huse and V. Elser, *Simple variational wave functions for two-dimensional Heisenberg spin- $\frac{1}{2}$  antiferromagnets*, Phys. Rev. Lett. **60**, 2531 (1988). 4
- [11] B. Bernu, P. Lecheminant, C. Lhuillier, and L. Pierre, *Exact spectra, spin susceptibilities, and order parameter of the quantum heisenberg antiferromagnet on the triangular lattice*, Phys. Rev. B **50**, 10048 (1994). 4
- [12] M. Boninsegni, *Ground state of a triangular quantum antiferromagnet: Fixed-node Green-function Monte Carlo study*, Phys. Rev. B **52**, 15304 (1995). 4
- [13] L. Capriotti, A. E. Trumper, and S. Sorella, *Long-range Néel order in the triangular Heisenberg model*, Phys. Rev. Lett. **82**, 3899 (1999). 4
- [14] C. Weber, A. Läuchli, F. Mila, and T. Giamarchi, *Magnetism and superconductivity of strongly correlated electrons on the triangular lattice*, Phys. Rev. B **73**, 014519 (2006). 4
- [15] D. Heidarian, S. Sorella, and F. Becca, *Spin- $\frac{1}{2}$  Heisenberg model on the anisotropic triangular lattice: From magnetism to a one-dimensional spin liquid*, Phys. Rev. B **80**, 012404 (2009). 4

- [16] L. Balents, *Spin liquids in frustrated magnets*, Nature **464**, 199 (2010). 4
- [17] Y. Zhou, K. Kanoda, and T.-K. Ng, *Quantum spin liquid states*, Rev. Mod. Phys. **89**, 025003 (2017). 4
- [18] J. Villain, R. Bidaux, J.-P. Carton, and R. Conte, *Order as an effect of disorder*, J. Phys. France **41**, 1263 (1980). 4
- [19] S.-I. Tomonaga, *Remarks on Bloch's method of sound waves applied to many-fermion problems*, Prog. Theor. Phys. **5**, 544 (1950). 4
- [20] J. M. Luttinger, *An exactly soluble model of a many-fermion system*, J. Math. Phys. **4**, 1154 (1963). 4
- [21] S. R. White, *Density-matrix algorithms for quantum renormalization groups*, Phys. Rev. B **48**, 10345 (1993). 5, 6, 73
- [22] U. Schollwöck, *The density-matrix renormalization group*, Rev. Mod. Phys. **77**, 259 (2005). 5
- [23] S. R. White, *Strongly correlated electron systems and the density matrix renormalization group*, Phys. Rep. **301**, 187 (1998). 6
- [24] S. R. White, *Density-matrix algorithms for quantum renormalization groups*, Phys. Rev. B **48**, 10345 (1993). 6
- [25] J. Gaiete, *Angular quantization and the density matrix renormalization group*, Mod. Phys. Lett. A **16**, 1109 (2001). 6
- [26] A. Galindo and M. A. Martín-Delgado, *Information and computation: Classical and quantum aspects*, Rev. Mod. Phys. **74**, 347 (2002). 6
- [27] T. J. Osborne and M. A. Nielsen, *Entanglement, quantum phase transitions, and density matrix renormalization*, Quantum Inf. Process **1**, 45 (2002). 6
- [28] J. I. Latorre, E. Rico, and G. Vidal, *Ground state entanglement in quantum spin chains*, Quantum Inf. Comput. **4**, 48 (2004). 6
- [29] H.-J. Mikeska and A. K. Kolezhuk, *One-dimensional magnetism*, Lect. Notes Phys **645**, (2008). 9, 10
- [30] L. Faddeev and L. Takhtajan, *What is the spin of a spin wave?*, Phys. Lett. A **85**, 375 (1981). 9
- [31] J. W. Bray, H. R. Hart, L. V. Interrante, I. S. Jacobs, J. S. Kasper, G. D. Watkins, S. H. Wee, and J. C. Bonner, *Observation of a spin-Peierls transition in a Heisenberg antiferromagnetic linear-chain system*, Phys. Rev. Lett. **35**, 744 (1975). 10
- [32] M. Hase, I. Terasaki, and K. Uchinokura, *Observation of the spin-Peierls transition in linear  $\text{Cu}^{2+}$  ( $\text{spin}-\frac{1}{2}$ ) chains in an inorganic compound  $\text{CuGeO}_3$* , Phys. Rev. Lett. **70**, 3651 (1993). 10



- 
- [33] M. Nishi, O. Fujita, and J. Akimitsu, *Neutron-scattering study on the spin-Peierls transition in a quasi-one-dimensional magnet CuGeO<sub>3</sub>*, Phys. Rev. B **50**, 6508 (1994). 11
- [34] J. A. Northby, H. A. Groenendijk, L. J. de Jongh, J. C. Bonner, I. S. Jacobs, and L. V. Interrante, *Field-dependent differential susceptibility studies on tetrathiafulvalene-AuS<sub>4</sub>C<sub>4</sub>(CF<sub>3</sub>)<sub>4</sub>: Universal aspects of the spin-Peierls phase diagram*, Phys. Rev. B **25**, 3215 (1982). 11
- [35] R. Werner, C. Gros, and M. Braden, *Microscopic spin-phonon coupling constants in CuGeO<sub>3</sub>*, Phys. Rev. B **59**, 14356 (1999). 11
- [36] F. D. M. Haldane, *Spontaneous dimerization in the  $S=\frac{1}{2}$  Heisenberg antiferromagnetic chain with competing interactions*, Phys. Rev. B **25**, 4925 (1982). 11, 15
- [37] K. Okamoto and K. Nomura, *Fluid-dimer critical point in  $S = \frac{1}{2}$  antiferromagnetic Heisenberg chain with next nearest neighbor interactions*, Phys. Lett. A **169**, 433 (1992). 11, 15
- [38] S. R. White and I. Affleck, *Dimerization and incommensurate spiral spin correlations in the zigzag spin chain: Analogies to the Kondo lattice*, Phys. Rev. B **54**, 9862 (1996). 11, 15
- [39] S.-L. Drechsler, O. Volkova, A. N. Vasiliev, N. Tristan, J. Richter, M. Schmitt, H. Rosner, J. Málek, R. Klingeler, A. A. Zvyagin, and B. Büchner, *Frustrated cuprate route from antiferromagnetic to ferromagnetic spin- $\frac{1}{2}$  Heisenberg chains: Li<sub>2</sub>ZrCuO<sub>4</sub> as a missing link near the quantum critical point*, Phys. Rev. Lett. **98**, 077202 (2007). 11, 12, 15
- [40] L. Heinze, G. Bastien, B. Ryll, J.-U. Hoffmann, M. Reehuis, B. Ouladdiaf, F. Bert, E. Kermarrec, P. Mendels, S. Nishimoto, S.-L. Drechsler, U. K. Rößler, H. Rosner, B. Büchner, A. J. Studer, K. C. Rule, S. Süllow, and A. U. B. Wolter, *Magnetic phase diagram of the frustrated spin chain compound linarite PbCuSO<sub>4</sub>(OH)<sub>2</sub> as seen by neutron diffraction and <sup>1</sup>H-NMR*, Phys. Rev. B **99**, 094436 (2019). 12, 13
- [41] T. Hikihara, L. Kecke, T. Momoi, and A. Furusaki, *Vector chiral and multipolar orders in the spin- $\frac{1}{2}$  frustrated ferromagnetic chain in magnetic field*, Phys. Rev. B **78**, 144404 (2008). 11
- [42] F. Schrettle, S. Krohns, P. Lunkenheimer, J. Hemberger, N. Büttgen, H.-A. Krug von Nidda, A. V. Prokofiev, and A. Loidl, *Switching the ferroelectric polarization in the  $S = \frac{1}{2}$  chain cuprate LiCuVO<sub>4</sub> by external magnetic fields*, Phys. Rev. B **77**, 144101 (2008). 11, 13
- [43] H.-J. Grafe, S. Nishimoto, M. Iakovleva, E. Vavilova, L. Spillecke, A. Alfonsov, M.-I. Sturza, S. Wurmehl, H. Nojiri, H. Rosner, J. Richter, U. K. Rößler, S.-L. Drechsler, V. Kataev, and B. Büchner, *Signatures of a magnetic field-induced unconventional nematic liquid in the frustrated and anisotropic spin-chain cuprate LiCuSbO<sub>4</sub>*, Sci. Rep. **7**, 6720 (2017). 11, 13, 15, 16, 37

- [44] T. Masuda, A. Zheludev, A. Bush, M. Markina, and A. Vasiliev, *Competition between helimagnetism and commensurate quantum spin correlations in LiCu<sub>2</sub>O<sub>2</sub>*, Phys. Rev. Lett. **92**, 177201 (2004). 11
- [45] A. N. Vasil'ev, L. A. Ponomarenko, H. Manaka, I. Yamada, M. Isobe, and Y. Ueda, *Magnetic and resonant properties of quasi-one-dimensional antiferromagnet LiCuVO<sub>4</sub>*, Phys. Rev. B **64**, 024419 (2001). 11
- [46] M. Enderle, C. Mukherjee, B. Fåk, R. K. Kremer, J.-M. Broto, H. Rosner, S.-L. Drechsler, J. Richter, J. Malek, A. Prokofiev, W. Assmus, S. Pujol, J.-L. Raggazzoni, H. Rakoto, M. Rheinstädter, and H. M. Rønnow, *Quantum helimagnetism of the frustrated spin- $\frac{1}{2}$  chain LiCuVO<sub>4</sub>*, Europhysics Lett. (EPL) **70**, 237 (2005). 11
- [47] K. C. Rule, B. Willenberg, M. Schäpers, A. U. B. Wolter, B. Büchner, S.-L. Drechsler, G. Ehlers, D. A. Tennant, R. A. Mole, J. S. Gardner, S. Süllow, and S. Nishimoto, *Dynamics of linarite: Observations of magnetic excitations*, Phys. Rev. B **95**, 024430 (2017). 12
- [48] B. Willenberg, M. Schäpers, A. U. B. Wolter, S.-L. Drechsler, M. Reehuis, J.-U. Hoffmann, B. Büchner, A. J. Studer, K. C. Rule, B. Ouladdiaf, S. Süllow, and S. Nishimoto, *Complex field-induced states in linarite PbCuSO<sub>4</sub>(OH)<sub>2</sub> with a variety of high-order exotic spin-density wave states*, Phys. Rev. Lett. **116**, 047202 (2016). 12, 13
- [49] K. Y. Povarov, Y. Feng, and A. Zheludev, *Multiferroic phases of the frustrated quantum spin-chain compound linarite*, Phys. Rev. B **94**, 214409 (2016). 12
- [50] Y. Feng, K. Y. Povarov, and A. Zheludev, *Magnetic phase diagram of the strongly frustrated quantum spin chain system PbCuSO<sub>4</sub>(OH)<sub>2</sub> in tilted magnetic fields*, Phys. Rev. B **98**, 054419 (2018). 12
- [51] B. Willenberg, M. Schäpers, K. C. Rule, S. Süllow, M. Reehuis, H. Ryll, B. Klemke, K. Kiefer, W. Schottenhamel, B. Büchner, B. Ouladdiaf, M. Uhlarz, R. Beyer, J. Wosnitza, and A. U. B. Wolter, *Magnetic frustration in a quantum spin chain: The case of linarite PbCuSO<sub>4</sub>(OH)<sub>2</sub>*, Phys. Rev. Lett. **108**, 117202 (2012). 12
- [52] F. Pollmann, E. Berg, A. Turner, and M. Oshikawa, *Symmetry protection of topological phases in one-dimensional quantum spin systems*, Phys. Rev. B **85**, 075125 (2012). 15, 20, 29
- [53] F. Haldane, *Continuum dynamics of the 1-D Heisenberg antiferromagnet: Identification with the O(3) nonlinear sigma model*, Physics Lett. A **93**, 464 (1983). 15, 17, 32
- [54] T. Kennedy and H. Tasaki, *Hidden symmetry breaking and the Haldane phase in S = 1 quantum spin chains*, Comm. Math. Phys. **147**, 431 (1992). 15, 19
- [55] M. Oshikawa, *Hidden  $\mathbb{Z}_2 \times \mathbb{Z}_2$  symmetry in quantum spin chains with arbitrary integer spin*, J Phys. Condens. Matter **4**, 7469 (1992). 15, 19

- 
- [56] *Introduction to Frustrated Magnetism*, Vol. 164 of *Springer Series in Solid-State Sciences*, edited by C. Lacroix, P. Mendels, and F. Mila (Springer-Verlag, Berlin Heidelberg, 2011). 15
- [57] J. Villain, R. Bidaux, J.-P. Carton, and R. Conte, *Order as an effect of disorder*, J. Phys. France **41**, 1263 (1980). 15
- [58] C. Majumdar and D. Ghosh, *On next nearest neighbor interaction in linear chains. I*, J. Math. Phys. **10**, 1388 (1969). 15, 17
- [59] H. P. Bader and R. Schilling, *Conditions for a ferromagnetic ground state of Heisenberg Hamiltonians*, Phys. Rev. B **19**, 3556 (1979). 15, 31
- [60] M. Härtel, J. Richter, D. Ihle, and S.-L. Drechsler, *Thermodynamics of a one-dimensional frustrated spin- $\frac{1}{2}$  Heisenberg ferromagnet*, Phys. Rev. B **78**, 174412 (2008). 15, 31
- [61] R. Bursill, G. Gehringt, D. Farnellt, J. Parkinson, T. Xian, and C. Zeng, *Numerical and approximate analytical results for the frustrated spin- $\frac{1}{2}$  quantum spin chain*, J. Phys.: Condens. Matter **7**, 8605 (1995). 15, 31
- [62] J. Sirker, V. Y. Krivnov, D. V. Dmitriev, A. Herzog, O. Janson, S. Nishimoto, S.-L. Drechsler, and J. Richter,  *$J_1 - J_2$  Heisenberg model at and close to its  $z=4$  quantum critical point*, Phys. Rev. B **84**, 144403 (2011). 15
- [63] S. Furukawa, M. Sato, S. Onoda, and A. Furusaki, *Ground-state phase diagram of a spin- $\frac{1}{2}$  frustrated ferromagnetic XXZ chain: Haldane dimer phase and gapped/gapless chiral phases*, Phys. Rev. B **86**, 094417 (2012). 15, 23
- [64] A. A. Nersesyan, A. O. Gogolin, and F. H. L. Eßler, *Incommensurate spin correlations in spin- $\frac{1}{2}$  frustrated two-leg Heisenberg ladders*, Phys. Rev. Lett. **81**, 910 (1998). 15, 20, 23
- [65] C. Itoi and S. Qin, *Strongly reduced gap in the zigzag spin chain with a ferromagnetic interchain coupling*, Phys. Rev. B **63**, 224423 (2001). 15, 20, 23, 31, 35
- [66] C. de Graaf, I. de P. R. Moreira, F. Illas, Ò. Iglesias, and A. Labarta, *Magnetic structure of  $\text{Li}_2\text{CuO}_2$ : From ab initio calculations to macroscopic simulations*, Phys. Rev. B **66**, 014448 (2002). 15
- [67] A. Orlova, E. L. Green, J. M. Law, D. I. Gorbunov, G. Chanda, S. Krämer, M. Horvatić, R. K. Kremer, J. Wosnitza, and G. L. J. A. Rikken, *Nuclear magnetic resonance signature of the spin-nematic phase in  $\text{LiCuVO}_4$  at high magnetic fields*, Phys. Rev. Lett. **118**, 247201 (2017). 15
- [68] H. Ueda, S. Onoda, Y. Yamaguchi, T. Kimura, D. Yoshizawa, T. Morioka, M. Hagiwara, M. Hagiwara, M. Soda, T. Masuda, T. Sakakibara, K. Tomiyasu, S. Ohira-Kawamura, K. Nakajima, R. Kajimoto, M. Nakamura, Y. Inamura, M. Hase, and Y. Yasui, *Emergent spin-1 Haldane gap and ferroelectricity in a frustrated spin- $\frac{1}{2}$  ladder*, arXiv:1803.07081 (2018), arXiv: 1803.07081. 15

- [69] A. U. B. Wolter, F. Lipps, M. Schäpers, S.-L. Drechsler, S. Nishimoto, R. Vogel, V. Kataev, B. Büchner, H. Rosner, M. Schmitt, M. Uhlarz, Y. Skourski, J. Wosnitza, S. Süllow, and K. C. Rule, *Magnetic properties and exchange integrals of the frustrated chain cuprate linearite PbCuSO<sub>4</sub>(OH)<sub>2</sub>*, Phys. Rev. B **85**, 014407 (2012). 15
- [70] L. Kecke, T. Momoi, and A. Furusaki, *Multimagnon bound states in the frustrated ferromagnetic one-dimensional chain*, Phys. Rev. B **76**, 060407(R) (2007). 15
- [71] J. Sudan, A. Lüscher, and A. M. Läuchli, *Emergent multipolar spin correlations in a fluctuating spiral: The frustrated ferromagnetic spin- $\frac{1}{2}$  Heisenberg chain in a magnetic field*, Phys. Rev. B **80**, 140402(R) (2009). 15
- [72] M. Hase, H. Kuroe, K. Ozawa, O. Suzuki, H. Kitazawa, G. Kido, and T. Sekine, *Magnetic properties of Rb<sub>2</sub>Cu<sub>2</sub>Mo<sub>3</sub>O<sub>12</sub> including a one-dimensional spin- $\frac{1}{2}$  Heisenberg system with ferromagnetic first-nearest-neighbor and antiferromagnetic second-nearest-neighbor exchange interactions*, Phys. Rev. B **70**, 104426 (2004). 16
- [73] Y. Yasui, R. Okazaki, I. Terasaki, M. Hase, M. Hagihala, T. Masuda, and T. Sakakibara, *Low temperature magnetic properties of frustrated quantum spin chain system Rb<sub>2</sub>Cu<sub>2</sub>Mo<sub>3</sub>O<sub>12</sub>*, JPS Conf. Proc. **3**, 014014 (2014). 16
- [74] I. Affleck, T. Kennedy, E. H. Lieb, and H. Tasaki, *Rigorous results on valence-bond ground states in antiferromagnets*, Phys. Rev. Lett. **59**, 799 (1987). 16, 17, 23, 25, 32
- [75] M. den Nijs and K. Rommelse, *Preroughening transitions in crystal surfaces and valence-bond phases in quantum spin chains*, Phys. Rev. B **40**, 4709 (1989). 19
- [76] S. R. White and D. A. Huse, *Numerical renormalization-group study of low-lying eigenstates of the antiferromagnetic S=1 Heisenberg chain*, Phys. Rev. B **48**, 3844 (1993). 25
- [77] H. Li and F. D. M. Haldane, *Entanglement spectrum as a generalization of entanglement entropy: Identification of topological order in non-abelian fractional quantum Hall effect states*, Phys. Rev. Lett. **101**, 010504 (2008). 26, 85
- [78] G. Vidal, I. Latorre, E. Rico, and A. Kitaev, *Entanglement in quantum critical phenomena*, Phys. Rev. Lett. **90**, 227902 (2003). 26
- [79] C. E. Agrapidis, S.-L. Drechsler, J. van den Brink, and S. Nishimoto, *Crossover from an incommensurate singlet spiral state with a vanishingly small spin gap to a valence-bond solid state in dimerized frustrated ferromagnetic spin chains*, Phys. Rev. B **95**, 220404(R) (2017). 26
- [80] F. Pollmann, A. Turner, E. Berg, and M. Oshikawa, *Entanglement spectrum of a topological phase in one dimension*, Phys. Rev. B **81**, 064439 (2010). 26
- [81] G. Uhrig, F. Schönfeld, M. Laukamp, and E. Dagotto, *Unified quantum mechanical picture for confined spinons in dimerized and frustrated spin chains*, Eur. Phys. J. B **7**, 67 (1999). 29

- 
- [82] T. Kennedy, *Exact diagonalisations of open spin-1 chains*, J. Phys. Condens. Matter **2**, 5737 (1990). 31
- [83] A. A. Nersesyan, A. O. Gogolin, and F. H. L. Eßler, *Incommensurate spin correlations in spin- $\frac{1}{2}$  frustrated two-leg Heisenberg ladders*, Phys. Rev. Lett. **81**, 910 (1998). 31
- [84] K. Hida, *Haldane gap in the spin- $\frac{1}{2}$  double chain Heisenberg antiferromagnet - numerical diagonalization and projector Monte Carlo study*, J. Phys. Soc. Jpn. **60**, 1347 (1991). 32, 33
- [85] H. Watanabe, K. Nomura, and S. Takada,  *$S=\frac{1}{2}$  quantum Heisenberg ladder and  $S=1$  Haldane phase*, J. Phys. Soc. Jpn. **62**, 2845 (1993). 32, 33, 34
- [86] J. Timonen, J. Solyom, and J. B. Parkinson, *Critical behaviour of coupled spin chains*, Journal of Physics: Condensed Matter **3**, 3343 (1991). 34
- [87] S. Ejima and H. Fehske, *Comparative density-matrix renormalization group study of symmetry-protected topological phases in spin-1 chain and Bose-Hubbard models*, Phys. Rev. B **91**, 045121 (2015). 34
- [88] S. R. White, *Equivalence of the antiferromagnetic Heisenberg ladder to a single  $S=1$  chain*, Phys. Rev. B **53**, 52 (1996). 35
- [89] K. Nomura and T. Murashima, *Incommensurability and edge state in quantum spin chain*, J. Phys. Soc. Jpn. **74**, 42 (2005). 35
- [90] S. Nishimoto, S.-L. Drechsler, R. Kuzian, J. Richter, J. Málek, M. Schmitt, J. van den Brink, and H. Rosner, *The strength of frustration and quantum fluctuations in  $\text{LiVCuO}_4$* , EPL **98**, 37007 (2012). 37
- [91] K. Rule, B. Willenberg, M. Schäpers, A. Wolter, B. Büchner, S.-L. Drechsler, G. Ehlers, D. Tennant, R. Mole, J. Gardner, S. Süllow, and S. Nishimoto, *Dynamics of linarite: Observations of magnetic excitations*, Phys. Rev. B **95**, 024430 (2017). 37
- [92] A. Kitaev, *Anyons in an exactly solved model and beyond*, Annals of Physics **321**, 2 (2006). 39, 40, 43, 45, 46
- [93] H.-D. Chen and Z. Nussinov, *Exact results of the Kitaev model on a hexagonal lattice: spin states, string and brane correlators, and anyonic excitations*, Journal of Physics A: Mathematical and Theoretical **41**, 075001 (2008). 41, 43, 84
- [94] V. M. Katukuri, R. Yadav, L. Hozoi, S. Nishimoto, and J. van den Brink, *The vicinity of hyper-honeycomb  $\beta\text{-Li}_2\text{IrO}_3$  to a three-dimensional Kitaev spin liquid state*, Sci. Rep. **6**, 29585 (2016). 47, 48
- [95] G. Jackeli and G. Khaliullin, *Mott insulators in the strong spin-orbit coupling limit: From Heisenberg to a quantum compass and Kitaev models*, Phys. Rev. Lett. **102**, 017205 (2009). 46, 47

- [96] S. Trebst, *Kitaev Materials*, arXiv e-prints arXiv:1701.07056 (2017). 47, 48
- [97] Y. Singh, S. Manni, J. Reuther, T. Berlijn, R. Thomale, W. Ku, S. Trebst, and P. Gegenwart, *Relevance of the Heisenberg-Kitaev model for the honeycomb lattice Iridates  $A_2IrO_3$* , Phys. Rev. Lett. **108**, 127203 (2012). 48
- [98] S. K. Choi, R. Coldea, A. N. Kolmogorov, T. Lancaster, I. I. Mazin, S. J. Blundell, P. G. Radaelli, Y. Singh, P. Gegenwart, K. R. Choi, S.-W. Cheong, P. J. Baker, C. Stock, and J. Taylor, *Spin waves and revised crystal structure of honeycomb iridate  $Na_2IrO_3$* , Phys. Rev. Lett. **108**, 127204 (2012). 48, 76, 78
- [99] T. Takayama, A. Kato, R. Dinnebier, J. Nuss, H. Kono, L. S. I. Veiga, G. Fabbris, D. Haskel, and H. Takagi, *Hyperhoneycomb iridate  $\beta$ - $Li_2IrO_3$  as a platform for Kitaev magnetism*, Phys. Rev. Lett. **114**, 077202 (2015). 48
- [100] S. H. Chun, J.-W. Kim, J. Kim, H. Zheng, C. C. Stoumpos, C. D. Malliakas, J. F. Mitchell, K. Mehlawat, Y. Singh, Y. Choi, T. Gog, A. Al-Zein, M. M. Sala, M. Krisch, J. Chaloupka, G. Jackeli, G. Khaliullin, and B. J. Kim, *Direct evidence for dominant bond-directional interactions in a honeycomb lattice iridate  $Na_2IrO_3$* , Nat. Phys. **11**, 462 (2015). 48
- [101] K. Kitagawa, T. Takayama, Y. Matsumoto, A. Kato, R. Takano, Y. Kishimoto, S. Bette, R. Dinnebier, G. Jackeli, and H. Takagi, *A spin-orbital-entangled quantum liquid on a honeycomb lattice*, Nature **554**, 341 EP (2018). 48
- [102] A. Banerjee, C. A. Bridges, J.-Q. Yan, A. A. Aczel, L. Li, M. B. Stone, G. E. Granroth, M. D. Lumsden, Y. Yiu, J. Knolle, S. Bhattacharjee, D. L. Kovrizhin, R. Moessner, D. A. Tennant, D. G. Mandrus, and S. E. Nagler, *Proximate Kitaev quantum spin liquid behaviour in a honeycomb magnet*, Nat. Mater. **15**, 733 (2016). 48, 71
- [103] S.-H. Do, S.-Y. Park, J. Yoshitake, J. Nasu, Y. Motome, Y. S. Kwon, D. T. Adroja, D. J. Voneshen, K. Kim, T.-H. Jang, J.-H. Park, K.-Y. Choi, and S. Ji, *Majorana fermions in the Kitaev quantum spin system  $\alpha$ - $RuCl_3$* , Nature Physics **13**, 1079 (2017). 48
- [104] R. Hentrich, A. U. Wolter, X. Zotos, W. Brenig, D. Nowak, A. Isaeva, T. Doert, A. Banerjee, P. Lampen-Kelley, D. G. Mandrus, S. E. Nagler, J. Sears, Y.-J. Kim, B. Büchner, and C. Hess, *Unusual phonon heat transport in  $\alpha$ - $RuCl_3$  : Strong spin-phonon scattering and field-induced spin gap*, Phys. Rev. Lett. **120**, 117204 (2018). 48, 93
- [105] Y. Kasahara, T. Ohnishi, Y. Mizukami, O. Tanaka, S. Ma, K. Sugii, N. Kurita, H. Tanaka, J. Nasu, Y. Motome, T. Shibauchi, and Y. Matsuda, *Majorana quantization and half-integer thermal quantum Hall effect in a Kitaev spin liquid*, Nature **559**, 227 (2018). 48, 93
- [106] B. Huang, W. Choi, Y. B. Kim, and Y.-M. Lu, *Classification and properties of quantum spin liquids on the hyperhoneycomb lattice*, Phys. Rev. B **97**, 195141 (2018). 48

- 
- [107] M. Becker, M. Hermanns, B. Bauer, M. Garst, and S. Trebst, *Spin-orbit physics of  $j = \frac{1}{2}$  mott insulators on the triangular lattice*, Phys. Rev. B **91**, 155135 (2015). 48
- [108] I. Rousochatzakis, U. K. Rössler, J. van den Brink, and M. Daghofer, *Kitaev anisotropy induces mesoscopic  $\mathbb{Z}_2$  vortex crystals in frustrated hexagonal antiferromagnets*, Phys. Rev. B **93**, 104417 (2016). 48
- [109] Y. Singh and P. Gegenwart, *Antiferromagnetic Mott insulating state in single crystals of the honeycomb lattice material  $\text{Na}_2\text{IrO}_3$* , Phys. Rev. B **82**, 064412 (2010). 48
- [110] R. D. Johnson, S. C. Williams, A. A. Haghighirad, J. Singleton, V. Zapf, P. Manuel, I. I. Mazin, Y. Li, H. O. Jeschke, R. Valenti, and R. Coldea, *Monoclinic crystal structure of  $\alpha$ - $\text{RuCl}_3$  and the zigzag antiferromagnetic ground state*, Phys. Rev. B **92**, 235119 (2015). 48
- [111] A. Koitzsch, C. Habenicht, E. Müller, M. Knupfer, B. Büchner, S. Kretschmer, M. Richter, J. van den Brink, F. Börrnert, D. Nowak, A. Isaeva, and T. Doert, *Nearest-neighbor Kitaev exchange blocked by charge order in electron-doped  $\alpha$ - $\text{RuCl}_3$* , Phys. Rev. Materials **1**, 052001 (2017). 49
- [112] A. Koitzsch, C. Habenicht, E. Müller, M. Knupfer, B. Büchner, H. C. Kandpal, J. van den Brink, D. Nowak, A. Isaeva, and T. Doert,  *$J_{\text{eff}}$  description of the honeycomb Mott insulator  $\alpha$ - $\text{RuCl}_3$* , Phys. Rev. Lett. **117**, 126403 (2016). 49
- [113] L. J. Sandilands, Y. Tian, A. A. Reijnders, H.-S. Kim, K. W. Plumb, Y.-J. Kim, H.-Y. Kee, and K. S. Burch, *Spin-orbit excitations and electronic structure of the putative Kitaev magnet  $\alpha$ - $\text{RuCl}_3$* , Phys. Rev. B **93**, 075144 (2016). 49
- [114] L. J. Sandilands, C. H. Sohn, H. J. Park, S. Y. Kim, K. W. Kim, J. A. Sears, Y.-J. Kim, and T. W. Noh, *Optical probe of Heisenberg-Kitaev magnetism in  $\alpha$ - $\text{RuCl}_3$* , Phys. Rev. B **94**, 195156 (2016). 49
- [115] C. E. Agrapidis, J. van den Brink, and S. Nishimoto, *Numerical study of the Kitaev-Heisenberg chain as a spin model of the K-intercalated  $\text{RuCl}_3$* , Journal of Physics: Conference Series **969**, 012112 (2018). 49
- [116] E. Sela, H.-C. Jiang, M. H. Gerlach, and S. Trebst, *Order-by-disorder and spin-orbital liquids in a distorted Heisenberg-Kitaev model*, Phys. Rev. B **90**, 035113 (2014). 49, 51, 65
- [117] W. Brzezicki, J. Dziarmaga, and A. M. Oleś, *Quantum phase transition in the one-dimensional compass model*, Phys. Rev. B **75**, 134415 (2007). 49
- [118] S. Mondal, D. Sen, and K. Sengupta, *Quench dynamics and defect production in the Kitaev and extended Kitaev models*, Phys. Rev. B **78**, 045101 (2008). 49
- [119] U. Divakaran and A. Dutta, *Reverse quenching in a one-dimensional Kitaev model*, Phys. Rev. B **79**, 224408 (2009). 49

- [120] E. Eriksson and H. Johannesson, *Multicriticality and entanglement in the one-dimensional quantum compass model*, Phys. Rev. B **79**, 224424 (2009). 49
- [121] S. Mahdavifar, *Numerical study of the one-dimensional quantum compass model*, Eur. Phys. J. B **77**, 77 (2010). 49
- [122] V. Subrahmanyam, *Block entropy for Kitaev-type spin chains in a transverse field*, Phys. Rev. A **88**, 032315 (2013). 49
- [123] H. Katsura, D. Schuricht, and M. Takahashi, *Exact ground states and topological order in interacting Kitaev/Majorana chains*, Phys. Rev. B **92**, 115137 (2015). 49
- [124] R. Steinigeweg and W. Brenig, *Energy dynamics in the Heisenberg-Kitaev spin chain*, Phys. Rev. B **93**, 214425 (2016). 49
- [125] A. Gogolin, A. Nersesyan, and A. Tselik, *Bosonization and Strongly Correlated Systems* (Cambridge University Press, Cambridge, 1998). 60
- [126] I. Affleck and A. W. W. Ludwig, *Universal noninteger “ground-state degeneracy” in critical quantum systems*, Phys. Rev. Lett. **67**, 161 (1991). 60
- [127] C. Holzhey, F. Larsen, and F. Wilczek, *Geometric and renormalized entropy in conformal field theory*, Nucl. Phys. B **424**, 443 (1994). 60
- [128] P. Calabrese and J. Cardy, *Entanglement entropy and quantum field theory*, Journal of Statistical Mechanics: Theory and Experiment **2004**, P06002 (2004). 60
- [129] S. Nishimoto, *Tomonaga-luttinger-liquid criticality: Numerical entanglement entropy approach*, Phys. Rev. B **84**, 195108 (2011). 61
- [130] A. Y. Kitaev, *Unpaired Majorana fermions in quantum wires*, Physics-Uspekhi **44**, 131 (2001). 62
- [131] J. Chaloupka, G. Jackeli, and G. Khaliullin, *Zigzag magnetic order in the iridium oxide  $\text{Na}_2\text{IrO}_3$* , Phys. Rev. Lett. **110**, 097204 (2013). 64, 85
- [132] J. D. Johnson, S. Krinsky, and B. M. McCoy, *Vertical-arrow correlation length in the eight-vertex model and the low-lying excitations of the XYZ Hamiltonian*, Phys. Rev. A **8**, 2526 (1973). 66
- [133] T. Schneider, E. Stoll, and U. Glaus, *Excitation spectrum of planar spin- $\frac{1}{2}$  Heisenberg XXZ chains*, Phys. Rev. B **26**, 1321 (1982). 66
- [134] R. Yadav, N. A. Bogdanov, V. M. Katukuri, S. Nishimoto, J. van den Brink, and L. Hozoi, *Kitaev exchange and field-induced quantum spin-liquid states in honeycomb  $\alpha\text{-RuCl}_3$* , Sci. Rep. **6**, 37925 (2016), article. 71
- [135] K. Ran, J. Wang, W. Wang, Z.-Y. Dong, X. Ren, S. Bao, S. Li, Z. Ma, Y. Gan, Y. Zhang, J. T. Park, G. Deng, S. Danilkin, S.-L. Yu, J.-X. Li, and J. Wen, *Spin-wave excitations evidencing the Kitaev interaction in single crystalline  $\alpha\text{-RuCl}_3$* , Phys. Rev. Lett. **118**, 107203 (2017). 71



- 
- [136] A. Metavitsiadis, C. Psaroudaki, and W. Brenig, *Spin liquid fingerprints in the thermal transport of a Kitaev-Heisenberg ladder*, Phys. Rev. B **99**, 205129 (2019). 73
- [137] S. R. White, R. M. Noack, and D. J. Scalapino, *Resonating valence bond theory of coupled Heisenberg chains*, Phys. Rev. Lett. **73**, 886 (1994). 79
- [138] N. Wu, *Topological phases of the two-leg Kitaev ladder*, Physics Lett. A **376**, 3530 (2012). 83
- [139] X.-Y. Feng, G.-M. Zhang, and T. Xiang, *Topological characterization of quantum phase transitions in a spin- $\frac{1}{2}$  model*, Phys. Rev. Lett. **98**, 087204 (2007). 83, 84
- [140] A. Catuneanu, E. S. Sørensen, and H.-Y. Kee, *Nonlocal string order parameter in the  $S = \frac{1}{2}$  Kitaev-Heisenberg ladder*, Phys. Rev. B **99**, 195112 (2019). 83, 84
- [141] T. Barnes, E. Dagotto, J. Riera, and E. S. Swanson, *Excitation spectrum of Heisenberg spin ladders*, Phys. Rev. B **47**, 3196 (1993). 86
- [142] G. Bastien, G. Garbarino, R. Yadav, F. J. Martinez-Casado, R. B. Rodríguez, Q. Stahl, M. Kusch, S. P. Limandri, R. Ray, P. Lampen-Kelley, D. G. Mandrus, S. E. Nagler, M. Roslova, A. Isaeva, T. Doert, L. Hozoi, A. U. B. Wolter, B. Büchner, J. Geck, and J. van den Brink, *Pressure-induced dimerization and valence bond crystal formation in the Kitaev-Heisenberg magnet  $\alpha$ -RuCl<sub>3</sub>*, Phys. Rev. B **97**, 241108(R) (2018). 90



# Acknowledgments

---

This dissertation is the product of more than three years of work. During this time, I have met new people and made new friends while still getting the support of the old ones. Here I would like to thank all the persons without whom I could not have managed to complete my PhD.

A first, special thank goes to my supervisors Prof. Jeroen van den Brink and Dr. Satoshi Nishimoto. In particular, I want to thank Prof. van den Brink for always supporting me in visiting conferences and school and Dr. Nishimoto for always being so kind and available to answer my questions and discuss my research.

Secondly, I wish to thank my office mates, Dr. Ekaterina Pärschke, your presence is always a delight, Dr. Alexander Lau, for after work physics discussion, Andrei Pavlov, without whom our afternoon teapot would have been empty, and Ziba Zangenehpourzadeh, your strength against adversity is an inspiration.

I wish to thank my colleagues: Dr. Ion Cosma Fulga, Dr. Rajyavardhan Ray, Dr. Ching-Hao Chang, Dr. Jorge Facio, Selma Franca, Sanjib Kumar Das, Josef Kaufmann. A special appreciation goes to Dr. Flavio Nogueira for discussions ranging from physics to politics, from movies to books and for sharing cat videos.

A special thank goes to Ulrike Nitzsche, all of the results presented in this work were possible thanks to her technical assistance, and to Grit Rötzer, I could not have managed all my business trips and paperwork without her help.

I wish to thank my “out-of-institute” friends: Margarita, Yuliia, Olga, Elena, Jose, Francesco, Richard, Adam, Elvis, Chris: from swap-parties to bouldering evenings, from themed dinners to tea breaks, you have kept me sane during this journey.

I want to thank my family for their never ending support. In particular, I want to thank my grandmother, Alexandra, and my mother, Elettra, for always telling me women can do anything.

Lastly, a personal “thank you” is dedicated to my fiancé, Alexander Lau: thank you for always being there.



# Eidesstattliche Erklärung

---

Hiermit versichere ich, dass ich die vorliegende Arbeit ohne unzulässige Hilfe Dritter und ohne Benutzung anderer als der angegebenen Hilfsmittel angefertigt habe; die aus fremden Quellen direkt oder indirekt übernommenen Gedanken sind als solche kenntlich gemacht. Die Arbeit wurde bisher weder im Inland noch im Ausland in gleicher oder ähnlicher Form einer anderen Prüfungsbehörde vorgelegt.

Die vorliegende Dissertation wurde vom 01.04.2016 bis 26.08.2019 am Leibniz-Institut für Festkörper- und Werkstoffforschung Dresden (IFW Dresden), Institut für theoretische Festkörperphysik (ITF), unter der Betreuung von Prof. Dr. Jeroen van den Brink und Dr. Satoshi Nishimoto angefertigt.

Es haben keine erfolglosen Promotionsverfahren in der Vergangenheit stattgefunden. Die aktuelle Promotionsordnung der Fakultät Physik der Technischen Universität Dresden wird anerkannt.

Clìo Eftthimia Agrapidis  
Dresden, 27 August 2019